UNIVERSITAT ROVIRA I VIRGILI

Department of Electronic, Electrical and Automatic Control Engineering

Fabrication of bulk and interdigitated organic solar cells and analysis of degradation mechanisms

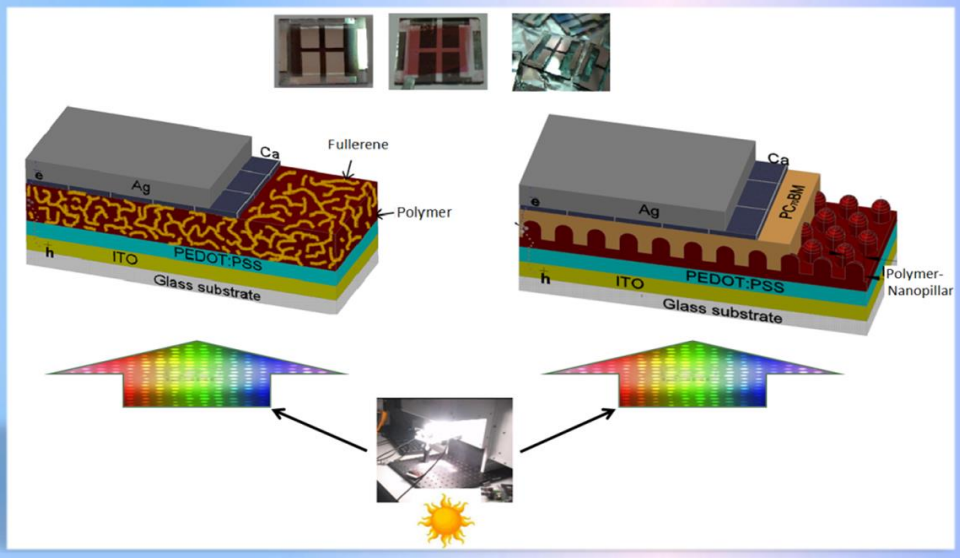

DOCTORAL THESIS

Victor Samuel Balderrama Vázquez

Victor Samuel Balderrama Vázquez

FABRICATION OF BULK AND INTERDIGITATED ORGANIC SOLAR CELLS AND ANALYSIS OF DEGRADATION MECHANISMS

DOCTORAL THESIS

Supervised by
Dr. Lluís Francesc Marsal Garví

Departament d'Enginyeria Electrònica, Elèctrica i Automàtica
Nanoelectronic and Photonic System Group (NePhos)

UNIVERSITAT ROVIRA I VIRGILI

Tarragona
2014

UNIVERSITAT ROVIRA I VIRGILI
ESCOLA TÈCNICA SUPERIOR D'ENGINYERIA
DEPARTAMENT D'ENGINYERIA ELECTRONICA, ELÈCTRICA I AUTOMÀTICA

Avinguda dels Països Catalans, 26
Campus sescelades
43007 Tarragona
Tel. (977) 55 96 10
Fax (977) 55 96 05
e-mail: secelec@etse.urv.es
http://www.etse.urv.es/DEEEA/

I STATE that the present study, entitled "Fabrication of bulk and interdigitated organic solar cells and analysis of degradation mechanisms", presented by Victor Samuel Balderrama Vázquez for the award of the degree of Doctor, has been carried out under my supervision at the Department of Electrical, Electronic and Automatic Control Engineering of this University, and that it fulfils all the requirements to be eligible for the International Doctorate Award.

Tarragona, 09th October 2014

Doctoral Thesis Supervisor

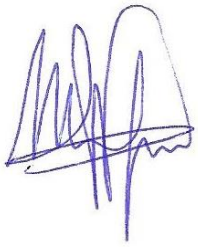

Dr. Lluís Marsal Garví

Acknowledgements

I express my gratitude to Dr. Lluís F. Marsal by his knowledge, time, dedication, guidance, support, encouragement and invaluable advices throughout of this work to achieve the Ph.D. degree.

I would like to thank Dr. Josep Ferré-Borrull for the comments and corrections of this work and the scientific articles.

Many thanks to Dr. Josep Pallarès by his recommendations, corrections and suggestions in the works made.

I would like to thank all colleagues of NePhos group for their help and support over these four years: Pilar, Pedro, María, Gerard, José and Peilin.

I would like to thank Dr. Magali Estrada from Mexico of CINVESTAV by her knowledge, experience and the support that she gave for this work and as well as her friendship.

I would also like to thank Dr. Emilio Palomares and his work team in ICIQ for helping, correcting and improving the scientific articles and as well as the collaboration and contribution for this thesis. Also I am very grateful with Dr. Aurelien Viterisi and Dr. Josep Albero by the experience, the knowledge and the availability of time that they gave me.

I offer my gratitude to the staff of the Scientific and Technical Service (SRCiT) for their support and patience during the characterization sessions (Dr. Mariana Stankova, Dr. Lukas Vojkuvka, Dr. Rita Marimon and Mercé Moncusí).

I would like to thank Dr. Elizabeth von Hauff from Vrije Univesity of Amsterdam (Netherlands) for accepting me in her group of Organic Solar Cells. I appreciate also all the help, support, knowledge and discussion about of the work and the effective way of collaborating with the Dr. von Hauff. I would

also like to thank Simon Schmeißer, Andreas Peukert, Dr. Alina Chanaewa and Renate Kaiser by the support during the research done in Freiburg University.

I would like to thank Romain by his frankness, friendship, knowledge and discussion of many topics.

I would like to thank Abel Santos by teach me all the alumina fabrication process at the beginning of my Ph.D., also by his friendship and knowledge.

My family from Mexico, I express my gratitude for everything, because they are always with me: Laura, Cristal, Jaqueline, Nancy, Paloma, all my Nieces and Nephews and my Parents. I would like to thank all my friends that I have known during my formation of Ph.D.: Souhila, Fátima, Helen, Julian, Juan Carlos, Francois, among other.

As well, I would like to thank Oliver baby and his parents: Javier and Gloria for their support, friendship, confidence that they offered me, during my Ph.D. formation. I would like to thank Karen and José for their friendship and help.

This work has been supported by Spanish Ministry of Science and Innovation (MICINN) under grant number TEC2006-06531, TEC2009-09551 and TEC2008-01342, HOPE CSD2007-00007 (Consolider-Ingenio 2010) and by Generalitat of Catalunya under project number 2009 SGR 549 and project AGAUR 2014 SGR 1344.

List of contributions

Journal publications arising from this thesis

[1] **V.S. Balderrama**, M. Estrada, P.L. Han, P. Granero, J. Pallarès, J. Ferré-Borrull and L.F. Marsal, "Degradation of Electrical properties of PTB1:PCBM solar cells under different environments", *Solar Energy Materials and Solar Cells 125* (2014) 155-163.

[2] **V.S. Balderrama**, M. Estrada, A. Viterisi, P. Formentín, J. Pallarès, J. Ferré-Borrull, E. Palomares, L.F. Marsal, "Correlation between P3HT inter-chain structure and Jsc of P3HT:$PC_{70}BM$ blends for solar cells", *Microelectronics Reliability 53* (2012) 560-564.

[3] **V.S. Balderrama**, M. Estrada, A. Cerdeira, B.S. Soto-Cruz, L.F. Marsal, J. Pallarès, J.C. Nolasco, B. Iñiguez, E. Palomares, J. Albero, "Influence of P3HT:PCBM blend preparation on the active layer morphology and cell degradation", *Microelectronics Reliability 51* (2010) 597-601.

[4] **V.S. Balderrama**, Josep Albero, Pedro Granero, Josep Ferré-Borrull, Josep Pallarès, Emilio Palomares, and Lluis Francesc Marsal, "Design, Fabrication and Kinetic Recombination Analysis of Interdigitated Heterojunction Nanomorphology on P3HT/$PC_{70}BM$ Solar Cell", Paper is in preparation.

Other Journal Publications

[1] P. Granero, **V.S. Balderrama**, J. Ferré-Borrull, J. Pallarès, L.F. Marsal, "Light absorption modelling of ordered bulk heterojunction organic solar cells", *Current Applied Physics 13* (2013) 1801-1807.

[2] P. Granero, **V.S. Balderrama**, J. Ferré-Borrull, J. Pallarès, L.F. Marsal, "Two-dimensional finite-element modelling of periodical interdigitated full organic solar cells", *Journal of Applied Physics 113* (2013) 1-7.

[3] Abel Santos, **V.S. Balderrama**, María Alba, Pilar Formentín, Josep Ferré-Borrull, Josep Pallarès, Lluís F. Marsal, "Nanoporous Anodic Alumina Barcodes: Toward Smart Optical Biosensors", *Advanced Materials 24* (2012) 1050-1054.

[4] Abel Santos, **V.S. Balderrama**, María Alba, Pilar Formentín, Josep Ferré-Borrull, Josep Pallarès, Lluís F Marsal, " Tunable Fabry-Pérot interferometer based on nanoporous anodic alumina for optical biosensing purposes", *Nanoscale Research Letters 7* (2012) 1-4.

[5] Abel Santos, Lukas Vojkuvka, María Alba, **V.S. Balderrama**, Josep Ferré –Borrull, Josep Pallarès, Lluís F. Marsal, "Understanding and morphology control of pore modulations in nanoporous anodic alumina by discontinuous anodization", *Physical Status Solidi a-Applications And Materials Science 209* (2012) 2045-2048.

[6] P. Han, **V.S. Balderrama**, A. Mihi, P. Formentín, J. Ferré-Borrull, J. Pallarès, and L.F. Marsal, "Improving the efficiency of PTB1:PCBM bulk heterojunction solar cells by polymer blend aging", *Submitted to IEEE Journal Photovoltaics.*

[7] **V.S. Balderrama**, J.G. Sánchez, M. Estrada, J. Ferré-Borrull, J. Pallarès, and L.F. Marsal, "Relation of polymer degradation in air with the charge carrier concentration in PTB1, PTB7 and PCBM layers used in high efficiency solar cells", *Submitted to IEEE Journal Photovoltaics.*

[8] **V.S. Balderrama**, S. Schmeißer, E. von Hauff, J. Ferré-Borrull, J. Pallarès, and L.F. Marsal, "High performance and stability on PTB7: $PC_{70}BM$ inverted organic solar cells using vanadium oxide as transition metal oxide", Paper is in preparation.

[9] **V.S. Balderrama**, P. Granero, J. Ferré-Borrull, J. Pallarès, and L.F. Marsal, "Optimization of electrons and holes block layers on PTB7:$PC_{70}BM$ bulk heterojunction solar cells using PFN and V_2O_5", Paper is in preparation.

[10] **V.S. Balderrama**, W. Cambarau, E. Palomares, J. Ferré-Borrull, J. Pallarès, and L.F. Marsal, "Influence of ITO conductive layer on inverted and conventional PTB7:$PC_{70}BM$ photovoltaic structures explored by recombination using CE and TPV characterization", Paper is in preparation.

Conference talks and poster sessions

[1] J. Ferré-Borrull, **V.S. Balderrama**, P. Granero, P. Han, A. Mihi, J. Pallarès, and L.F. Marsal, "Fabrication, modeling and degradation studies of ordered bulk heterojunction organic solar cells with nanostructured interfaces", *Congreso Internacional de Metalurgia y Materiales 14° SAM-CONAMET / IBEROMAT 2014*, Presentation, Santa Fe, Argentina, Oct 21st 2014.

[2] **V.S. Balderrama**, J.G. Sánchez, P. Granero, J. Pallarès, J. Ferré-Borrull, and L.F. Marsal, "Aging of PTB7:$PC_{70}BM$ Blend Solution to Fabricate Standard Solar Cell and Its Influence on Electrical Performance", *Graduate Students Meeting on Electronics Engineering GSMEE 2014*, Poster, Tarragona, Spain, Jun 19th 2014.

[3] **V.S. Balderrama**, M. Estrada, P.L. Han, P. Granero, J. Pallarès, J. Ferré-Borrull, L.F. Marsal, "Stability analysis of organic solar cells fabricated with PTB1:PCBM in accordance with established ISOS-D1 protocols", *Spanish Nanophotonics Conference CEN2014*, Presentation, Santander, Spain, May 15th 2014.

[4] **V.S. Balderrama**, P. Granero, P.L. Han, J. Ferré-Borrull, J. Pallarès, and L.F. Marsal, "Fabrication, characterization and design modeling of well-ordered interdigitated organic solar cells", *28th European PV Solar Energy Conference and Exhibition EU PVSEC 2013*, Poster, Paris, France, September 29th 2013.

[5] **V.S. Balderrama**, P. Granero, G. Macías, P. Formentín, J. Pallarès, J. Ferré-Borrull, L.F. Marsal, "Fabrication and Electrical Characterization of Nanostructured Organic Solar Cells with Large-Area Interdigitated

Array", *Graduate Students Meeting on Electronics Engineering 2013*, Presentation, Tarragona, Spain, Jun 27th 2013.

[6] **V.S. Balderrama**, P.L. Han, P. Granero, J. Pallarès, J. Ferré-Borrull and L.F. Marsal, "Performance and degradation of organic solar cells due to air exposure manufactured with low-band gap material", *9th International Conference on Organic Electronics ICOE 2013*, Poster, Grenoble, France, Jun 17th 2013.

[7] **V.S. Balderrama**, J. Pallarès, J. Ferré-Borrull, L. F. Marsal, "Polymer Nanostructures for Organic Solar Cell Applications", *223rd The Electrochemical Society*, Presentation, Toronto, Ontario, Canada, May 12th 2013.

[8] **V.S. Balderrama**, J. Ferré-Borrull, J. Pallarès, and L.F. Marsal, "Fabrication of High-Ordered PBDTTT-CF Polymer Nanopillar Arrays for Optoelectronic Applications", *9th Spanish Conference on Electron Devices CDE-2013*, Poster, Valladolid, Spain, February 12th 2013.

[9] **V.S. Balderrama**, P. Formentín, J. Pallarès, L.F. Marsal, "Organic Nanostructures with Low Band-Gap Materials: Manufacturing by Via Template-Assisted Method and Characterization for Optoelectronic Applications", *Spanish Nanophotonics Conference CEN2012*, Presentation, Carmona, Sevilla, Spain, October 1st 2012.

[10] **V.S. Balderrama**, P. Formentín, J. Pallarès and L.F. Marsal, "Correlation Between Absorbance and Geometrical Characteristics of the P3HT Nanopillars for Photovoltaic Applications", *Graduate Students Meeting on Electronic Engineering GSMEE-2012*, Poster, Tarragona, Spain, Jun 17th 2012.

[11] **V.S. Balderrama**, P. Formentín, J. Pallarès, L. F. Marsal, "Exceptional Array of PBDTTT-CF and P3HT Nanopillar Polymers with a Low-

Band gap for Photovoltaic Applications", *9th International Conference on Organic Electronics ICOE 2012*, Presentation, Tarragona, Spain, Jun 6th 2012.

[12] **V.S. Balderrama**, P. Formentín, J. Pallarès, and L.F. Marsal, "Optical Properties on Nanopillar Arrays for Organic Solar Cells Application", *European Materials Research Society EMRS 2012*, Poster, Strasburg, France, May 14th 2012.

[13] **V.S. Balderrama**, A. Santos, P. Formentín, J. Ferré-Borrull, J. Pallarès, and L.F. Marsal, "Nanostructured conducting polymers for flexible optoelectronic applications", *221st ECS Meeting, © 2012 The Electrochemical Society*, Presentation, Seattle, Washington, USA, May 6-10th 2012.

[14] **V.S. Balderrama**, P. Formentín, J. Pallarès, L. F. Marsal, M. Estrada, "Three Dimensional Interpenetrating Network Film Morphology of the Organic Bulk Heterojunction Solar Cells based on P3HT:$PC_{[70]}BM$", *8th International Caribbean Conference on Devices, Circuits and Systems ICCDCS 2012*, Presentation, Playa del Carmen, Quintana Roo, Mexico, March 14th 2012.

[15] **V.S. Balderrama**, M. Estrada, P. Formentín, A. Viterisi, J. Ferré-Borrull, J. Pallarès, E. Palomares and L.F. Marsal, "Influence and Relationship of Film Morphology on Organic Solar Cells Manufactured with Different P3HT:$PC_{[70]}BM$ Blend Solutions", *International Conference on Electrical Engineering Computing Science and Automatic Control CCE 2011*, Presentation, Mérida, Yucatan, Mexico, October 26th 2011

[16] **V.S. Balderrama**, M. Estrada, P. Formentín, A. Viterisi, J. Ferré-Borrull, J. Pallarès, E. Palomares and L.F. Marsal, "Film Morphology

of the Organic Solar Cells P3HT:PCBM[70], *Graduate Students Meeting on Electronics Engineering GSMEE-2011*, Poster, Tarragona, Spain, Jun 10th 2011.

[17] L.F. Marsal, **V.S. Balderrama**, M. Estrada, A. Sánchez, P. Formentín, E. Palomares, J. Pallarès, J.C. Nolasco, "Effect of Degradation in Organic Solar Cells with P3HT:PCBM[70] Blends", *219th ECS Meeting, © 2011 The Electrochemical Society*, Presentation, Montreal, QC, Canada, May 01st 2011.

[18] **V.S. Balderrama**, M. Estrada, P. Formentín, B. Iñiguez, J. Ferré-Borrull, J. Pallarès, J. C. Nolasco, E. Palomares, A. Sánchez, L.F. Marsal, "Performance and degradation of organic solar cells with different P3HT:PCBM[70] blend composition", *8th Spanish Conference on Electron Devices, CDE 2011*, Poster, Palma de Mallorca, Spain, February 8th 2011.

[19] M. Estrada, **V. Balderrama**, J. Albero, J. C. Nolasco, A. Cerdeira, L.F. Marsal, J. Pallarès, B. Iñiguez, E. Palomares, "Effect of Variations in Blend Preparation on the Properties of P3HT:PCBM Blend Solar Cells", *27th International Conference on Microelectronics MIEL 2010*, Presentation, Nis, Serbia, May 16th 2010.

[20] M. Estrada, **V. Balderrama**, J. Albero, J. C. Nolasco, A. Cerdeira, L.F. Marsal, J. Pallarès, B. Iñiguez, E. Palomares, "Importance of blend preparation in P3HT:PCBM blend solar cells", *The International Conference Materials Science in the Age of Nano*, Presentation, La Habana, Cuba, November 20th 2009.

The visible and non-visible events perceived for the human being are the results of the imminent movements generated by the living nature.

Victor Balderrama

Thesis Contents

General information

Motivation

The advancement of new energy technologies is crucial for climate stability and global security. Solar energy resources are vast: more energy reaches our planet in one hour than humankind consumes in an entire year. The need for clean, inexpensive and renewable energy has increasingly turned research attention towards polymer photovoltaic cells. Organic solar cells offer a potential route to large-scale solar deployment because of the possibility of large cost reductions if earth-abundant materials and inexpensive production technologies are used. However, these devices still cannot perform as efficiently as silicon-based devices. The recent introduction of new materials and processing techniques has resulted in a remarkable increase in power-conversion efficiency of above 12%. Controlling the interpenetrating network morphology is a key factor in obtaining devices with improved performance. Among the structures that are being studied and used for photovoltaic applications the most promising are bulk heterojunction and nanostructured architectures. The electrical properties and physical mechanisms must be understood in the photovoltaic structures and which they can be improvement in the design processes, the fabrication, the characterization and the technology used.

Aims

The objectives of the present thesis are the following:

i. To fabricate, characterize and optimize organic solar cells using blend layers such as P3HT:PCBM, P3HT:$PC_{70}BM$ and PTB1:PCBM

ii. To obtain structures such as bilayer, conventional, and nanostructured organic solar cells that enable us to understand not only the origin of the governed mechanisms in its operation but also the relationship between the characteristics of the blend used and the parameters of the final device.

To attain these objectives, we

1. made a literature review of the state-of-the-art of solar cell architectures
2. studied and characterized the polymers that make up the blends.
3. studied methods for preparing the blends used to manufacture the solar cells.
4. electrically and optically characterized the different techniques used to understand the physical parameters of the photovoltaic cell.
5. applied protocols to follow the degradation process of the organic solar cells under different environments.

Thesis structure

Chapter 1 explains how the photovoltaic effect is generated in semiconductor polymer solar cells and different architectures.

Chapter 2 presents and discusses the criteria for selecting materials for solar cells, and justifies the choice of the various polymer and fullerene materials used in this thesis. The most important performance parameters that define the solar cell are presented.

Chapter 3 analyses the degradation of the organic solar cells based on poly (3-hexylthiophene:[6,6]-phenyl-C61-butyric acid methyl ester, P3HT:PCBM blends prepared under different conditions. The model used aims to provide greater insight into the mechanisms involved in the behavior of the device and its degradation after working in ambient conditions.

Chapter 4 focuses on the relation between variations in the characteristics of the poly (3-hexylthiophene-2,5-diyl) (P3HT) chains and the resulting solar cell short circuit current density when the blend layers are prepared at different concentration ratios. To vary the lamellar structure in the blend layers μ-XRD analysis was used.

Chapter 5 studies the degradation process in solar cells under nitrogen and air environment and with encapsulation in accordance with established ISOS-D1 protocols. The solar cells were prepared with PTB1:PCBM materials. The evolution of the electrical measurements under light and dark conditions is used to analyze the degradation process over 5300 h and the relationship it has with the physical mechanisms. An exponential function was used to model PCE decay over time in order to understand the degradation mechanisms.

Chapter 6 discusses the fabrication, characterization and analysis of nanostructured organic solar cells by nanoimprinting using P3HT and $PC_{70}BM$ as donor and acceptor materials, respectively. The nanostructured organic solar

cell was characterized by J-V, CE and TPV, and then compared with the bulk heterojunction and bilayer structures.

Chapter 7 presents the conclusions drawn from the results of the research carried out during the thesis.

Chapter 1

Generation of the photovoltaic effect in organic solar cells

This chapter explains how the photovoltaic effect is generated in organic solar cells in semiconductor polymers. Different types of architectures are presented as well as their advantages and disadvantages. The physical parameters of organic and inorganic materials are compared as photovoltaic devices. Finally, the structures that will be used in this thesis are briefly described.

1.1. A brief history of organic solar cells

The origin of organic solar cells (OSC) can be traced back to between 1970 and 1975, but they really gathered momentum as from 1986. Interest in OSC was mainly due to two factors: first, to reduce the CO_2 pollution of the planet caused by the continued accelerated burning of fossil fuels; and second, to make them more cheaply than silicon cells, the manufacture of which requires large amounts of energy. [1, 2]

The efficiency of organic solar cells (OSC) has increased over time: 0.001% in 1975 [3], 1% in 1986 [4], 4.8% in 2006 [5], 5% in 2006 [6], PCE > 6% in 2009 [7], 8.3% in 2010 [8], 9.1% in 2011 [9], and over 12% in 2013 [10]. **Fig. 1.1** compares the efficiencies of OSC using different technologies.

Research into OSC has increased significantly because of their considerable potential in terms of:

1. Semi-transparency
2. Flexibility and light weight
3. Low-cost of manufacture
4. Manufacture at low temperatures
5. Integration as a photovoltaic device for large areas
6. Modulation to change properties of the organic semiconductor material
7. New structures and morphologies, among others

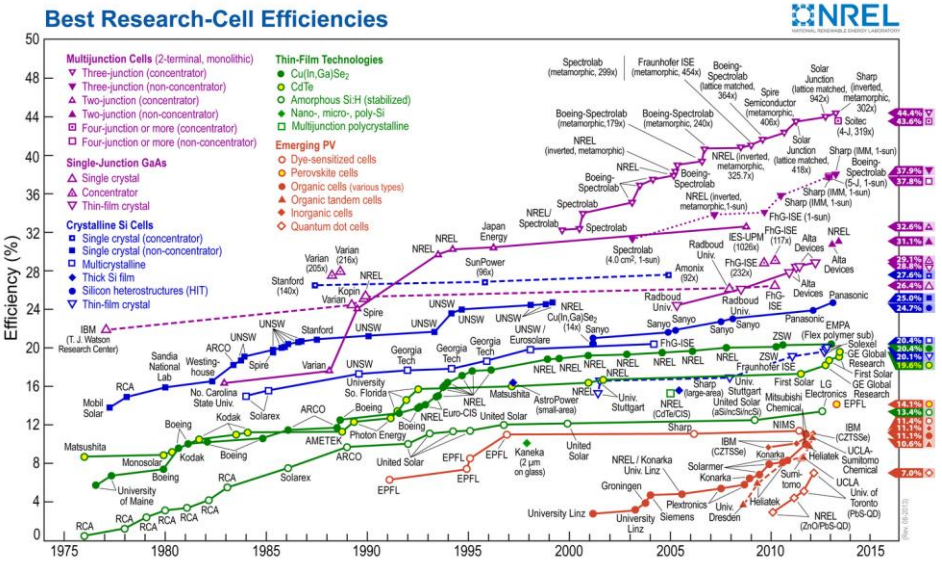

Fig. 1.1. Best recorded efficiencies reported in solar cells using different technologies.

Most research focuses primarily on understanding the physical mechanisms of how they work, stability problems and how their efficiency can be increased so that they can be used in applications. Once these obstacles have been overcome, they are expected to be commercialized. Whether they are viable for commercialization depends on the efficiency of amorphous silicon solar cells. This value must be equal to or greater than 13%, a target that is expected to be reached before 2020. [10]

Laboratories, research centres and private companies around the world have been working to improve the efficiency of OSC. Currently, the companies interested in working with these devices and setting the trend are: Konarka (US), Plextronics (US), Solarmer (US) Heliatek (Germany), Mitsubishi (Japan), Teijin DuPont Fims (Japan) Toray (Japan), Sumitomo Chemicals (Japan), Kolon (Korea), KNP Energy (Korea), GIST (Korea), KRICT (Korea), KIST (Korea) and Kimm (Korea), among others.

Table 1.1 shows some important milestones in the development of solar cells with polymeric materials. The information shown includes the materials, the blends, the structure, the technique used to deposit the active material, the additives used to improve the efficiency, and the substrate types used to allow for mechanical flexibility on the device structures.

1.2. Operation principles

Most organic solar cells consist of one or more active layers between two electrodes of different materials. [28] One of these electrodes must be transparent or semi-transparent, and indium tin oxide (ITO) is used frequently. The other electrode is a metal whose work function must be smaller to form an ohmic contact with the n-type material of the blend prepared. [29, 30]

Organic solar cells operate on the following principle (see **Fig. 1.2**):

1. - Photons are incident on the active layer, therefore giving the photo-excitation. This organic layer, in its simplest form, consists of a single layer of semiconducting polymer, although it is most often composed of a mixture of two or more semiconducting polymers. The first of these polymers is a p-type material, which acts as an electron donor (D) and the second is an n-type material and acts as an electron acceptor (A).

Year	*Development in the organic solar cells*	*Ref.*
2013	• In January 2013 Heliatek reported a new record efficiency of 12% for organic solar cells. They did not reveal the materials used.	11
2012	• Heliatek reported a new record efficiency of 10.7% for organic solar cells. They did not reveal the materials used.	12
2011	• In April 2011, the Mitsubishi Chemical Company reported a new record efficiency of 9.1% for organic solar cells. They did not reveal the materials used.	9
2010	• Konarka Technologies presented a PV bulk heterojunction. They did not reveal the materials used. The efficiency reported was 8.3%.	8
2009	• Sankai/Kawano presented a tandem structure using P3HT:bis[60]PCBM and P3HT:$PC_{70}BM$ as active blends.	13
2009	• Lim/Shu/Parkin fabricated a new n-type semiconductor material derived from pentacene. They manufactured the bulk heterojunction organic solar cell using P3HT.	14
2008	• Stefopoulos/Chochos presented a novel hybrid material – poly(3octylphenol) mixed with carbon nanotubes – which they used to obtain the photovoltaic device.	15
2008	• Neugebauer/Sariciftci used an additive for the first time to improve the efficiency of organic solar cells. The additive belonged to the alkali-thiol family.	16
2007	• Berson /De Bettignies manufactured a hybrid organic solar cell using carbon nanotubes as the semiconductor material. The structure was made with P3HT / CNT / PCBM.	17
2007	• Vak/Kim fabricated an organic solar cell using P3HT:PCBM as the active blend and was deposited by the spray method.	18
2005	• Huang /Efstathiadis made an organic solar cell with an ordered array of nanotubes.	19
2005	• Yoshioka/Williams/Wang presented a new method for depositing the organic active blend using ink printing.	20
2004	• Sanna /Cossu used flexible substrates to manufacture organic solar cells.	21
2004	• Sariciftci used a new co-polymer (PPE-PPV) to fabricate bulk heterojunction organic solar cells.	22
2002	• Sariciftci/Padinger reported the first bulk heterojunction organic solar cell using P3HT:PCBM as the active blend.	23
1995	• Yu/Hall manufactured the first bulk heterojunction organic solar cells using the stack polymer/polymer.	24
1994	• Yu reported the first photovoltaic bulk heterojunction device with the structure Polymer/C_{60}	25
1993	• Sariciftci fabricated the first photovoltaic heterojunction with the structure polymer/C_{60}.	26
1986	• Tang published for the first time the heterojunction device using phthalocyanine / tetracarboxylicl perilene in the photovoltaic device.	27

Table 1.1. Milestones in the development of organic solar cells between 1986 and 2013.

2. - The incident photons create excitons in the active layer, where the exciton is formed by an electron and hole polaron that are linked.

3. - In order to dissociate the exciton in the electron and hole polaron (hereinafter only electron and hole), an energy of 250 meV or more is required,

so the exciton must diffuse until the heterojunction is formed between the D and A materials. Generally, this process takes an ultra-short time interval of around 45 fs, and depends on the type of semiconductor polymers used. The exciton diffusion length is very short (between 10 and 20 nm).

4. - Once separated into electron and hole, these charge carriers must be transported through by the n-type (acceptor) and p-type (donor) materials, respectively, until they reach the electrodes where they must be collected. If the active layer is formed by a single semiconductor material, the separation process of the charge requires energies be provided by the asymmetry of the work functions of the electrodes.

5. - The charge carriers are collected at the electrodes; the holes at the anode and electrons at the cathode.

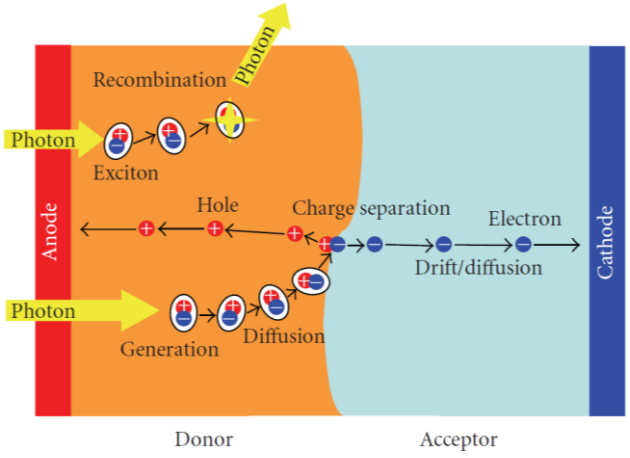

Fig. 1.2. Photovoltaic effect generated at the interface of the organic solar cells.

The next section classifies and explains the organic photovoltaic structures developed and studied in this thesis. The advantages and disadvantages of each one of them are also discussed.

1.3. Architecture of the organic solar cells

1.3.1. Classification

The structures for solar cells can be classified in a variety of ways. For example:

1. Single layer
2. Bilayer (BL)
3. Tandem
4. Bulk heterojunction (BHJ)
5. Inverted (INV)
6. Nanostructured (NS)
    - Hybrids (organic-inorganic) in the shape of nanopillars
    - Interdigitated (organic-organic)
    - Other types: nano-helical walls, nano-points, nano-tubes, nano-capsules, nano-cables, nano-dots (under development)
7. Hybrid solar cells
    - Dye
    - Dots
    - Nano-wires, etc.

Fig. 1.3 shows the various architectures manufactured and reported in this thesis. The references [31-37] describe the characteristics of each photovoltaic cell in greater detail.

The main reason to have different architectures in organic solar cells is to find the most optimal, stable and maximum performance parameters. To determine these characteristics, it is necessary to investigate the generation process, separation, transport and collection of the charge carriers, according to the basic operation principles (as described in section 1.2). They will also depend of the characteristics of the materials that are used, type of technology and the way in which they are managed and fabricated.

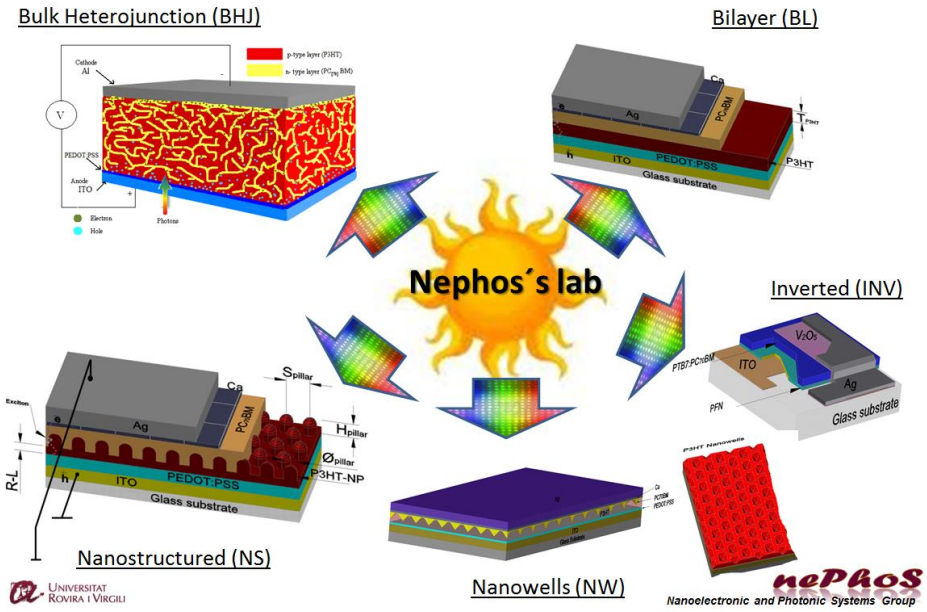

Fig. 1.3. Organic solar cells manufactured and analyzed in this thesis.

The next section below discusses the bilayer, bulk heterojunction and nanostructured organic solar cells that will be studied in this thesis.

1.3.2. Bilayer (BL) solar cell

Bilayer cell contains two layers between the conductive electrodes (see **Fig 1.4**). The two layers have different electron affinities and ionization

energies, so electrostatic forces are generated at the interface between the two layers. The materials are chosen to form a large enough local electric fields to split the excitons. The layer with the highest electron affinity and ionization potential is the electron acceptor, and the other layer is the electron donor. This structure is also called a planar donor-acceptor heterojunction.

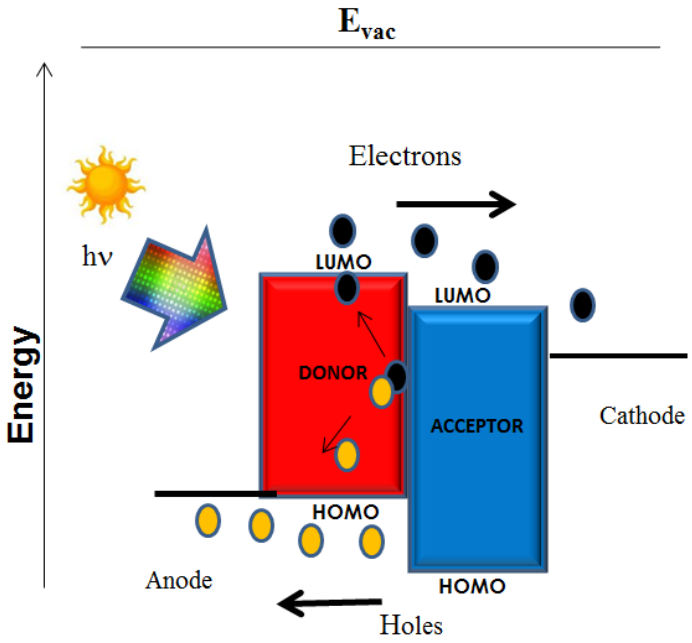

Fig. 1.4. Energy band diagram of BL organic solar cell shows the charge carriers collection direction.

The diffusion length of excitons in organic electronic materials is on the order of 10 nm as was explained above. In order to generate more excitons to diffuse to the layer interface and split into carriers, the layer thickness should be in the same range of diffusion length. However, the polymer layers typically need a thickness of at least 100 nm to absorb enough sun light. At such a large thickness, only a small fraction of the excitons can reach the heterojunction interface. Although the bilayer structure can improve the charge separation at the interfaces between donor and acceptor organic semiconducting layers, the

limitation is that the excitons created beyond of the 10 nm from the interface of D/A, they will not create free charge carriers, so that they cannot contribute in the performance for the photovoltaic cell. [38]

1.3.3. Bulk heterojunction (BHJ) solar cell

Bulk heterojunction (BHJ) organic solar cells are formed by a mixture of two or more polymeric materials with different electronic affinities and ionization potential. The polymeric materials should be diluted in a common solvent. The resulting mixture is deposited by spin coating to obtain a thin film with dominions of both materials in nanometric scale. The interpenetrated regions must be continues to transport the charge carriers towards electrodes as is shown in **Fig. 1.5**.

The active area between the in the bulk heterojunction of the cell is greater than in the device with bilayer structure. Inside the active layer phase segregations leads to the formation of the interpenetrated network, this depends on the conditions of the manufacturing process such as the temperature, annealing vapour, solvents, additives, etc.

A variety of BHJ solar cells with different kinds of polymer donors and fullerene acceptors (see **Fig. 1.6**), and some of their efficiencies have been reported. [39, 40]

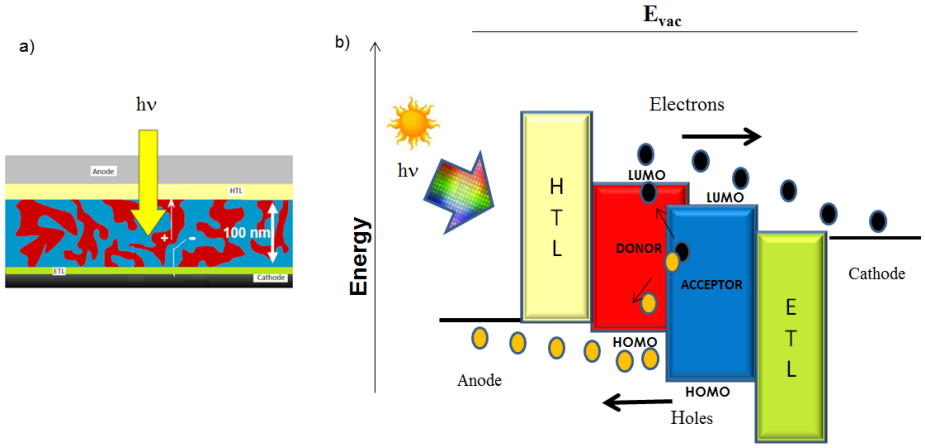

Fig. 1.5. (a) Structure of device; (b) Energy band diagram on BHJ organic solar cell shows the collection direction of the charge carriers. In the structure are added hole and electron transport layers (HTL and ETL).

1.3.4. Nanostructured (NS) solar cell

Nanostructured photovoltaic solar cells are considered to be ideal because they have a well ordered donor/acceptor interface in the nanometer scale between 10 and 20 nm, which is equivalent to the diffusion length of the exciton. The well-defined interfaces (D/A) in the solar cell are like small highways along which the charge carriers can travel easily to reach their respective metal contacts. [41, 42]

a)

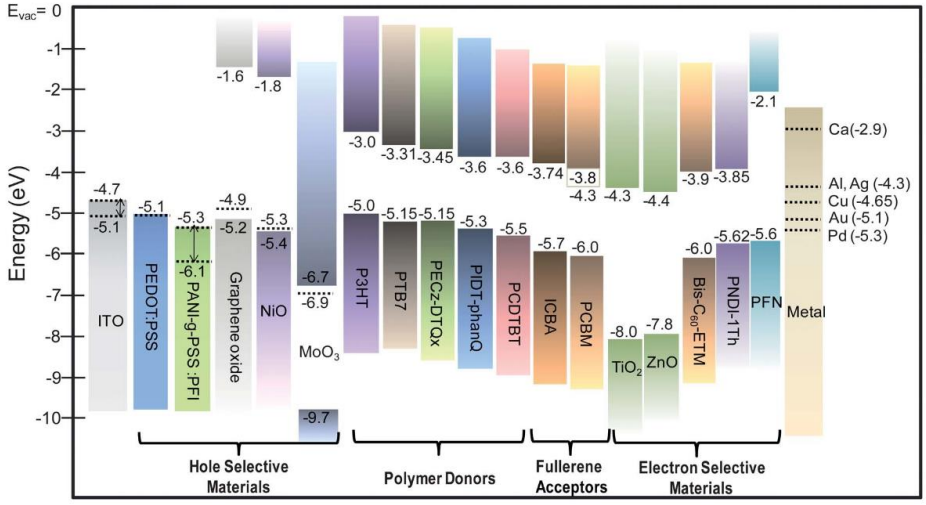

b)

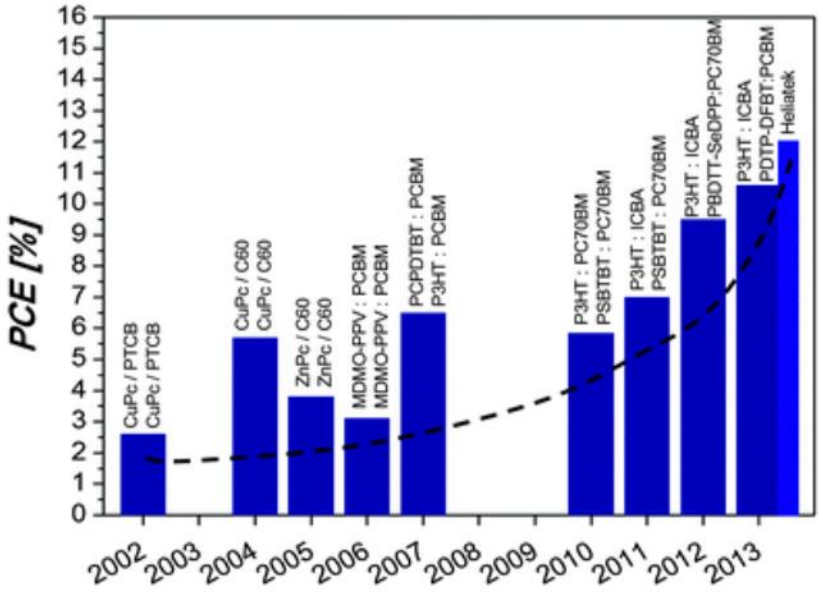

Fig. 1.6. (a) Schematic view of the energy gaps and energy levels of some organic materials used to fabricate photovoltaic devices. It shows the type of transparent electrodes, the hole selective materials, the polymer donors, the fullerene acceptors, electron selective materials and the metal electrodes. The dotted lines correspond to the

work functions of the materials. (b) Best efficiencies reported over time by some BHJ organic solar cells. [39, 40]

The solar cells with this interdigitated structure increase their interfacial area and also help to reduce charge carrier recombination. The result is an increase in cell efficiency. **Fig. 1.7** shows this interdigitated structure. The process by which this architecture is will be described in chapter 6.

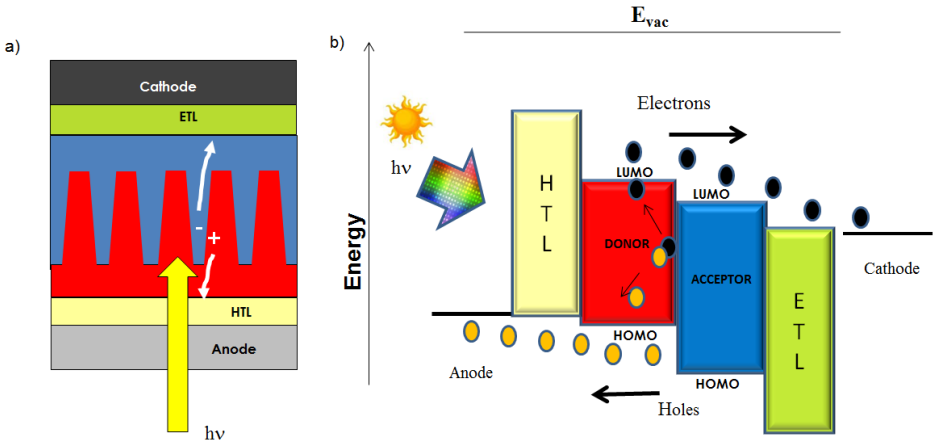

Fig. 1.7. (a) Nanostructured organic solar cell shows the cross section; (b) Energy band diagram of the nanostructured solar cell and shows the collection direction of the charge carriers (holes and electrons).

1.3.5. Inverted (INV) solar cell

Since their initial application in 2006, inverted organic solar cells (INV) have increasingly attracted attention due to their improved stability and compatibility with the roll-to-roll processes. The polarity of INV organic solar cells is reversed compared to that of conventional structures. The performance of inverted structures is critically dependent on the choice of the interfacial

layers, the combination of organic semiconductors choose to form the BHJ layer and the corresponding metallic contacts to collect the charge carriers. The most common electron conductor layers used for this structure are polyfluorene (PFN), titanium oxide (Ti_xO), zinc oxide (ZnO) and holes conductor layers are molybdenum oxide (MoO_3), vanadium oxide (V_2O_5) and tungsten oxide (WO_3) among others. [43-45] **Fig. 1.8** shows the typical structure and the energy band diagram.

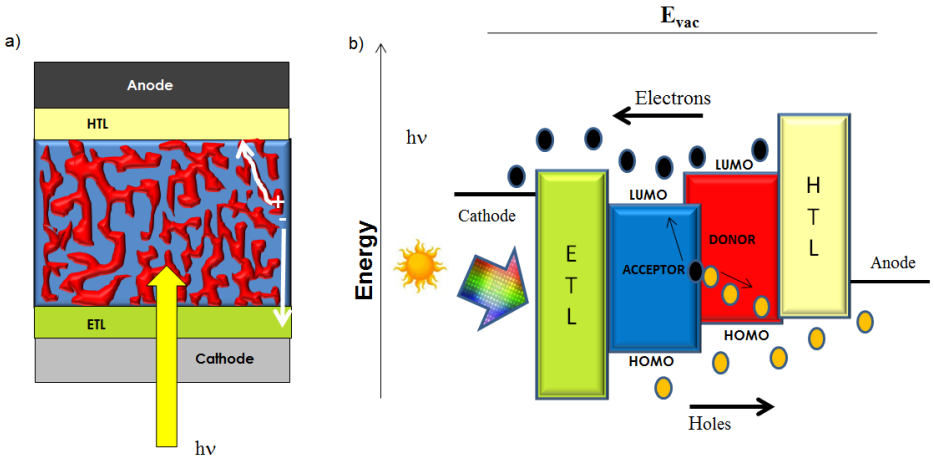

Fig. 1.8. (a) Inverted organic solar cell shows the structure; (b) Energy band diagram of an inverted organic solar cell which shows the collection direction of the charge carriers.

1.4. Differences between physical and chemical properties of the organic and inorganic materials

The mechanisms involved in the photovoltaic processes of organic cells are different from those in inorganic cells occur. Nevertheless, on the basis of the well-known operation principles of inorganic cells, we seek to provide a theoretical description that optimizes organic solar cells. Organic and inorganic semiconducting materials differ in the following aspects [46, 47]:

1. Inorganic semiconductor materials have a balance band and conduction band, whereas organic semiconducting refer to the same concept as highest occupied molecular orbital (HOMO) and lowest unoccupied molecular orbital (LUMO).

2. The binding energies are weaker in inorganic cells. For example, in silicon it is about $\Delta E = 25$ meV, whereas in organic cells it is $\Delta E = 250$ meV, so exciton dissociation in the inorganic materials occur at room temperature. Polymer materials require additional energy to be supplied. This is why dissociation occurs primarily at the interface between the materials (heterojunction), using the built-in potential.

3. Charge separation is difficult in organic semiconductors due to the relatively low dielectric constant (k), the value of which is between 3 and 4. This value reaches higher values in inorganic semiconductors (for example, about 11).

4. Therefore, the exciton must travel from the point at which it is generated to the point it will dissociate. This diffusion length is about 10 nm for polymers.

5. Hole diffusion length in amorphous silicon is around 0.1 to 2 μm, while in polymers it is around of 80 nm. It is the same occurs for the electrons.

6. Charge carrier mobility in polymers is reported to be between 10^{-5} and 1 cm^2 / V-s, while in amorphous silicon it is in the order of 1 cm^2 / V-s.

7. The absorption coefficient (α) in organic semiconductors is relatively high, so that a layer of 100 nm or less can be sufficient to absorb of the incident solar energy. For inorganic materials, thicker layers of tens of microns are necessary to absorb enough photons and generate the charge carriers required.

8. Organic semiconductors degrade in the presence of oxygen and water, and so are unstable in air. Inorganic semiconductors, on the other hand, are highly stable under air.

1.5. Advantages of organic solar cells

To date, the technological processing of organic solar cells is less complex and the manufacturing process less expensive, even in comparison with amorphous silicon. The use of such techniques as deposit by spin drop, ink injection and roll-to-roll processing will probably make manufacture in line possible.

The mechanical properties of polymeric films allow them to be deposited on large areas and flexible substrates using methods such as roll-to–roll. So solar cell panels can be installed on the surfaces of buildings or complex geometric surfaces without their electrical performance being affected.

As has been mentioned above, optical properties can be semi-transparent or have a high absorption coefficient inside the visible spectrum. Also, polymers can be designed with the band gap required for a specific structure and any other necessary properties.

The commercialization of organic solar cells will depend on factors such as their efficiency, lifetime and price per peak watt (Wp). At the moment, these parameters are still far below those obtained in amorphous silicon solar cells, so there is still a great deal of work to do in research if the expected results are to be obtained.

1.6. References

[1] E.S. Aydil, Nanomaterials for solar cells, *Nanotechnology Law & Business Fall*, Volume 4, (2007) No. 3, 275–291.

[2] C.J. Brabec, S. Gowrisanker, J.J. M. Halls, D. Laird, S. Jia, S. William, Polymer-Fullerene Bulk-Heterojunction Solar Cells, *Adv. Mater., 22*, (2010) 3839 – 3856.

[3] C.W. Tang and A.C. Albrecht, Photo voltaic effect of metal – chlorophyll-a-metal sandwich cells, *J. Chem. Phys., 62*, (1975) 2139–2149.

[4] M.C.W. Tang, Two-layer organic photovoltaic cell, *Appl. Phys. Lett., 48*, (1986) 183–185.

[5] M.A. Green, K. Emery, Y. Hishikawa and W. Warta, Solar Cell Efficiency Table (Version 28), *Res. Appl., 14*, (2006) 455 – 461.

[6] P. Schilinsky, Performance Analysis of printed bulk heterojunction solar cell, *Adv. Funct. Mater., 16* (2006) 1669–1672.

[7] M.A. Green, K. Emery, Y. Hishikawa and W. Warta, Solar Cell Efficiency Table (Version 37), *Res. Appl. 19* (2010) 84–92.

[8] M. Green, K. Emery, Y. Hishikawa and W. Warta, Solar Cell Efficiency Table (Version 37), *Res. Appl., 19* (2011) 84–92.

[9] Robert F. Service, Outlook Brightens for plastic solar cells, *Science, vol. 332* (2011) 293.

[10] M.A. Green, K. Emery, Y. Hishikawa, W. Warta, E.D. Dunlop, Solar cell efficiency tables (version 44), *Prog. Photovolt: Res. Appl., 22* (2014) 701−710.

[11] http://www.heliatek.com/newscenter/latest_news/neuer-weltrekord-fur-organische-solarzellen-heliatek-behauptet-sich-mit-12-zelleffizienz-als-technologiefuhrer/?lang=en

[12] http://www.heliatek.com/wp-content/uploads/2012/09/120427_PI_Heliatek-world-record-10_7-percent-efficiency.pdf

[13] J. Sakai, K. Kawano, T. Yamanari, T. Taima, Y. Yoshida, A. Fuji, M. Ozaki, Efficient organic photovoltaic tandem cells with novel transparent conductive oxide interlayer and poly (3-hexylthiophene): Fullerene active layers, *Sol. Energy Mater. Sol. Cells*, 94 (2009) 376−380.

[14] G. Lim Y.F., Shu Y., Parkin S.R., Anthony J.E., Malliaras G.G., Soluble n-type pentacene derivatives as novel acceptors for organic solar cells, *J. Mater. Chem., 19* (2009) 3049 – 3056.

[15] A.A. Stefopoulos, C.L. Chochos, M. Prato, G. Pistolis, K. Papagelis, F. Petraki, S. Kennou, J.K. Kallitsis, Novel hybrid materials consisting of regioregular poly(3-octylthiophene) covalently attached to single-wall carbon nanotubes, *Chem. - A European Journal*, 14 (2008), 8715–8724.

[16] A. Pivrikas, P. Stadler, H. Neugebauer, N.S. Sariciftci, Substituting the postproduction treatment for bulk-heterojunction solar cells using chemical additives, *Org. Electron., 9* (2008) 775–782.

[17] S. Berson, R. De Bettignies, S. Bailly, S. Guillerez, B. Jousselme, Elaboration of P3HT/CNT/PCBM composites for organic photovoltaic cells, *Adv. Funct. Mater., 17* (2007) 3363–3370.

[18] D. Vak, S.S. Kim, J. Jo, S.H. Oh, S.I. Na, J. Kim, D.Y. Kim, Fabrication of organic bulk heterojunction solar cells by a spray deposition method for low-cost power generation, *Appl. Phys. Lett., 91* (2007) 081102.

[19] Huang S., Efstathiadis H., Haldar P., Lee H. G., Landi B., Raffaelle R., Fabrication of nanorod arrays for organic solar cell applications, *Mater. Res. Soc. S. Proc., 836* (2005) 49–53.

[20] Y. Yoshioka, E. Williams, Q. Wang, D. Ginley, S. Shaheen, G. Jabbour, Progress in printed organic electronics and hybrid photovoltaics, *CLEO, 1* (2005) CMR5 314–315.

[21] O. Sanna, M. Cossu, T. Pilia, A. Bonfiglio, An original flexible structure for organic photovoltaic devices, *Mater. Res. Soc. Sym. Proc., 814* (2004) 259–264.

[22] H. Hoppe, D.A.M. Egbe, D. Mühlbacher, N.S. Sariciftci, Photovoltaic action of conjugated polymer/fullerene bulk heterojunction solar cells using novel PPE-PPV copolymers, *J. Mater. Chem., 14* (2004) 3462–3467.

[23] F. Padinger, R.S. Rittberger, N.S. Sariciftci, Effects of Postproduction Treatment on Plastic Solar Cells, *Adv. Funct. Mater., 13* (2003) 85–88.

[24] G. Yu, K. Pakbaz, A.J. Heeger, Charge separation and photovoltaic conversion in polymer composites with internal donor / acceptor heterojunctions, *J. Appl. Phys., 78* (1995) 4510–4515.

[25] G. Yu, K. Pakbaz, A. J. Heeger, Semiconducting polymers diodes: Large size, low cost photodetectors with excellent visible – ultraviolet sensitivity, *Appl. Phys. Lett., 64* (1994) 3422–3424.

[26] N.S. Sariciftci, L. Smilowitz, A. J. Heeger and F. Wudl, Semiconducting polymers (as donors) and buckminsterfullerene (as acceptor): photoinduced electron transfer and heterojunction devices, *Synt. Met., 59* (1993) 333–352.

[27] C.W. Tang, Two layer organic photovoltaic cell, *Appl. Phys. Lett., 48* (1986) 183–185.

[28] C.J. Brabec, N.S. Sariciftci, J.C. Hummelen, Plastic Solar Cells, *Adv. Funct. Mater., 11* (2001) 18–26.

[29] J. Huang, G. Li, and Y. Yang, Influence of composition and heat-treatment on the charge transport properties of poly (3-hexylthiophene) and [6,6]-phenyl C61- butyric acid methyl ester blends, *Appl. Phys. Lett., 87* (2005) 112105.

[30] D. Chirvase, J. Parisi, J.C. Hummelen and V. Dyakonov, Influence of nanomorphology on the photovoltaic action of polymer – fullerene composites, *Nanotechnology 15* (2004) 1317–1323.

[31] J.H. Schön, Ch. Kloc and B. Batlogg, Pentacene based photovoltaic devices, *Synt. Met., 124* (2001) 95–97.

[32] F. Fan, L.R. Faulkner, Photovoltaic effects of metal free and zinc phthalocyanines II- Properties of illuminated thin films cells, *J. Chem. Phys., 69* (1978) 3341–3349.

[33] G.D. Hans-Jürgen Prall, R. Koeppe, M. Egginger, R. Autengruber, and N.S. Sariciftci, Enhanced spectral coverage in tandem organic solar cells, *Appl. Phys. Lett., 89* (2006) 073502.

[34] Woon-HyukBaek, H. Yang, T. Yoon, C.J. Kang, H.H. Lee, Y. Kim, Effect of P3HT:PCBM concentration in solvent on performances of organic solar cells, *Sol. Energy Mater. Sol. Cells, 93* (2009) 1263–1267.

[35] S. Gunnes, H. Neugebauer, and N.S. Sariciftci, Conjugated Polymer-Based Organic Solar Cells, *Chem. Rev., 107* (2007) 1324–1338.

[36] M. Cravino, N.S. Sariciftci, For review on fullerene in double – cable polymers, *J. Mater. Chem., 12* (2002) 1931–2159.

[37] Z. Fan, H. Razavi, J. Do, A. Moriwaki, O. Ergn, Y. Chueh, Three – dimensional nanopillar - array photovoltaics on low-cost and flexible substrates, *Nat. Mater., 8* (2009) 648–653.

[38] H. Kim, S. Nam, J. Jeong, S. Lee, J. Seo, H. Han, Y. Kim, Organic solar cells based on conjugated polymers : History and recent advances, *Korean J. Chem. Eng., 31* (2014) 1095–1104.

[39] H.-L. Yip, A.K.Y. Jen, Recent advances in solution-processed interfacial materials for efficient and stable polymer solar cells, *Energy Environ. Sci., 5* (2012) 5994–6011.

[40] T. Ameri, N. Li, C.J. Brabec, Highly efficient organic tandem solar cells: a follow up review, *Energy Environ. Sci.,* 6 (2013) 2390–2413.

[41] D. Chen, W. Zhao, T.P. Russell, P3HT Nanopillars for Organic Photovoltaic Devices Nanoimprinted by AAO Templates, *ACS Nano., 6* (2012) 1479–1485.

[42] S. Moungthai, N. Mahadevapuram, P. Ruchhoeft, G.E. Stein, Direct Patterning of Conductive Polymer Domains for Photovoltaic Devices, *ACS Appl. Mater. Interfaces, 4* (2012) 4015–4023.

[43] F. Xie, W.C.H. Choy, C. Wang, X. Li, S. Zhang, J. Hou, Low-Temperature Solution-Processed Hydrogen Molybdenum and Vanadium Bronzes for an Efficient Hole-Transport Layer in Organic Electronics, *Adv. Mater., 25* (2013) 2051–2055.

[44] G. Teran-Escobar, J. Pampel, J.M. Caicedo, M. Lira-Cantu, Low-temperature, solution-processed, layered V_2O_5 hydrate as the hole-transport layer for stable organic solar cells, *Energ. Environ. Sci., 6* (2013) 3088–3098.

[45] T. Ameri, G. Dennler, C. Waldauf, P. Denk, K. Forberich, M.C. Scharber, C.J. Brabec, K. Hingerl, Realization, characterization, and optical modeling of inverted bulk-heterojunction organic solar cells, *J. Appl. Phys.*, *103* (2008) 084506.

[46] A. Checknane, H. S. Hilal, F. Djeffal, B. Benyouncef, J. P. Charles, An equivalente circuit approach to organic solar cell modeling, *Microelectron. J.*, *39* (2008) 1173–1180.

[47] K. Takahashi & M. Konagai, Amorphous Silicon Solar Cells, Tokyo Institute of Technology, *North Oxford Academic Publishers Ltd*., (1986).

Chapter 2

Organic semiconductor materials and photovoltaic parameters

The present chapter examines the criteria for selecting the semiconductor materials to be used for manufacturing organic solar cells. The photovoltaic parameters are described in order to provide insight the physical mechanisms involved when solar cells are exposed to light and dark conditions. An electrical circuit model is shown which represents the organic solar cell. The data extracted from the model will be used to correlate the physical parameters with the performance of photovoltaic devices.

2.1. General characteristics of organic materials

Organic compounds are chemical substances based on carbon and hydrogen that can also contain oxygen, nitrogen, sulphurs, phosphorus, boron, and halogens. These molecules appear in a wide variety of structures: chains, branches, rings, and even three-dimensional adjustments, all of which depend on the precursors and the conditions to fabricate and synthesize the materials and after they can be deposited by some technique. [1, 2]

The semiconducting properties of the organic compounds depend on the addition of small amounts of donors and acceptors to the material. The property of organic layers has been used to manufacture photovoltaic devices, diodes, transistors, etc.

As has been mentioned above, nowadays, numerous classes of semiconductor materials have been discovered with various structures. All these semiconductor structures share one characteristic: they all contain conjugated π bonds, in which the presence of highly polarizable mobile electrons plays an important role in the electrical performance of the material. Sigma bonds are non-conjugated and play different role.

The key to understanding the formation of these conjugated compounds is carbon chemistry. Carbon has an atomic number of 6 and a mass number of 12; its nucleus contains 6 protons and 6 neutrons and it is surrounded by 6 electrons, distributed in the following way: two in level 1s, two in level 2s and two in level 2p.

Its electronic configuration in the ground state is: $1s^2\ 2s^2\ 2p_x^1\ 2p_y^1$ $2p_z$. It is, however, tetravalent that is to say, it can form 4 bonds. When it receives external excitation, one of the electrons in orbital 2s moves to orbital $2p_z$, giving rise to the following electron distribution in the atom:

$1s^2\ 2s^1\ 2px^1\ 2py^1\ 2pz^1$

This transfer of one of the electrons (orbital s) to the p orbital of the same energy level makes the tetravalent carbon and is known as promotion. Once the electron has been promoted from the 2s orbital to the 2p orbital, the electron from the 2s orbital can combine with one or more 2p orbitals. This process is known as hybridization. There are three types of hybridization:

sp3 hybridization: the 2s electron combines with three 2p orbitals to form four hybrid sp3 bonds. As shown in **Fig. 2.1a** the angle between each bond is 109.5°. This type of hybridization produces tight bonds that are known as sigma-type bonds, with well localized electrons, resulting in excellent insulating materials that are not very reactive in the presence of air (see **Fig. 2.1 b).**

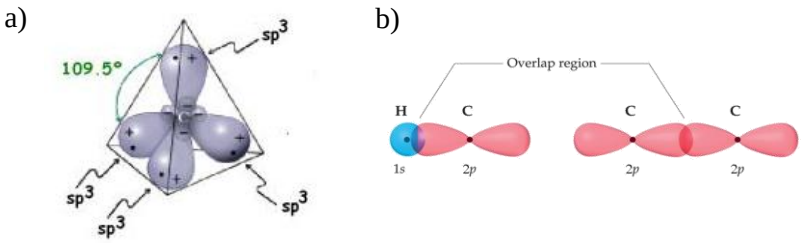

Fig. 2.1. a) Carbon hybridization is represented by its suborbital sp3; b) sigma-type bond is shown when two carbons interact with this hybridization.

sp2 hybridization: the 2s electron combines with two 2p orbitals to give 3sp2, leaving a one orbital 2p without hybridization. The three hybrid orbitals are arranged symmetrically in a plane with an angle of 120^o between them, while the p orbital without hybridization is left in a perpendicular plane.

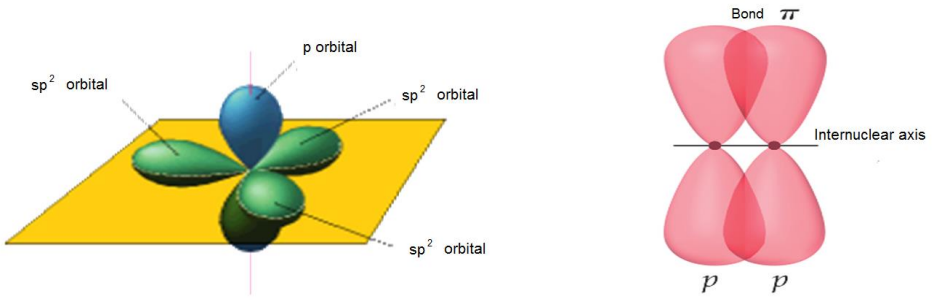

(a) (b)

Fig. 2.2. a) Hybridization of carbon is represented by its suborbital sp2; b) π–type bond between two p orbitals.

Two carbons with sp2 hybridization give rise to a weaker π-type bond, which is formed by the interaction, or lateral superposition, of both orbitals without hybridization see **Fig. 2.2b**. This bond is the one that gives rise to delocalized electrons and most organic semiconductors have this characteristic.

sp 1 hybridization: the 2s electron combines with one 2p orbital to give two sp1 bonds locate in the plane X at 180^{o} and two p orbitals. Y and Z axis are located two p orbitals without hybridization see **Fig. 2.3**. These p orbitals can give rise to two π-type bonds, as in the previous above.

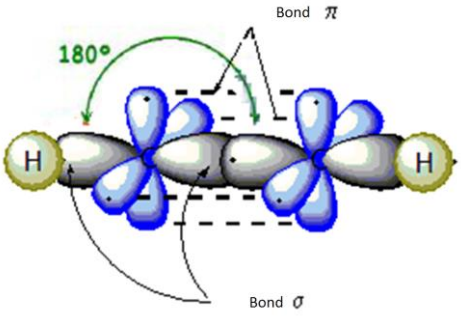

Fig. 2.3. Hybridization of carbon is represented by their sp1suborbital.

2.2. Organic semiconductors for photovoltaic applications

The great diversity of organic semiconductor materials for photovoltaic applications was one of the major technological developments that revolutionized the organic electronics industry.

The first applications appeared in 1970, with phthalocyanine and merocyanine molecules. [3] Ten years later, such polymeric materials as poly-acetylene polymers were created and applied to solar cells.

2.2.1. Characteristics of organic semiconductors

If they are to be applied in solar cells, organic semiconductors must have an optical band gap that can be efficiently excited by solar radiation in the visible and infrared region at wavelengths longer than 450 nm, (equivalent corresponding values lower than 2.75 eV). Donor and acceptor materials are needed to manufacture the photovoltaic cell. The combination of donors and acceptors must allow for correct displacement between its HOMOs and LUMOs. The polymers selected must also be able to be dissolved in reliable solvents and subsequently deposited. [4]

The main problems in organic semiconductor materials that must be resolved are listed below:

a) High band-gaps are of 2 - 3 eV.

b) Absorption takes place in a small fraction of the solar spectrum.

c) Incompatible solubility means that some organic semiconductor cannot be dissolved with others.

d) The way in which they are deposited.

e) The organization of their molecules.

f) Stability and the degradation.

g) The technology is not suitable, etc.

Generally, the parameter used to measure the performance in organic solar cells is efficiency. The reason for the low yield obtained when the semiconductor materials are used to manufacture organic solar cells is that photoexcitation does not form enough free charge carriers in the active layer of the material. [5]

Numerous investigations are now being carried out to solve the problems of organic semiconductors among them the synthesis of new molecules of low molecular weight. This new synthesis of organic semiconductors has intensified the study of organic solar cells.

Organic semiconductor materials are dividing into two different classes depending on the size of the molecules:

1. Materials of low molecular weight or small molecules (oligomers).
2. Materials of high molecular weight or large molecules (polymers).

Oligomers and polymers are made up of monomers, which are simple chemical molecules that connect to each other to form larger molecules. The combination of few monomers, generally fewer than 10, form oligomers and many repeated units are regarded polymers. Small molecule materials are deposited by evaporation or sublimation in the gaseous phase, whereas polymers are deposited by centrifugation and ink injection among other low cost, and low temperature techniques.

2.2.2. Semiconductor donor molecules

In polymers, donor material is that which allows the conduction of holes in the material but in the heterojunction it provides or donates the electrons to the layer. **Fig. 2.4** shows some donor polymer molecules, which have such molecules as nitrogen, oxygen and sulphur in their structure. [4, 6]

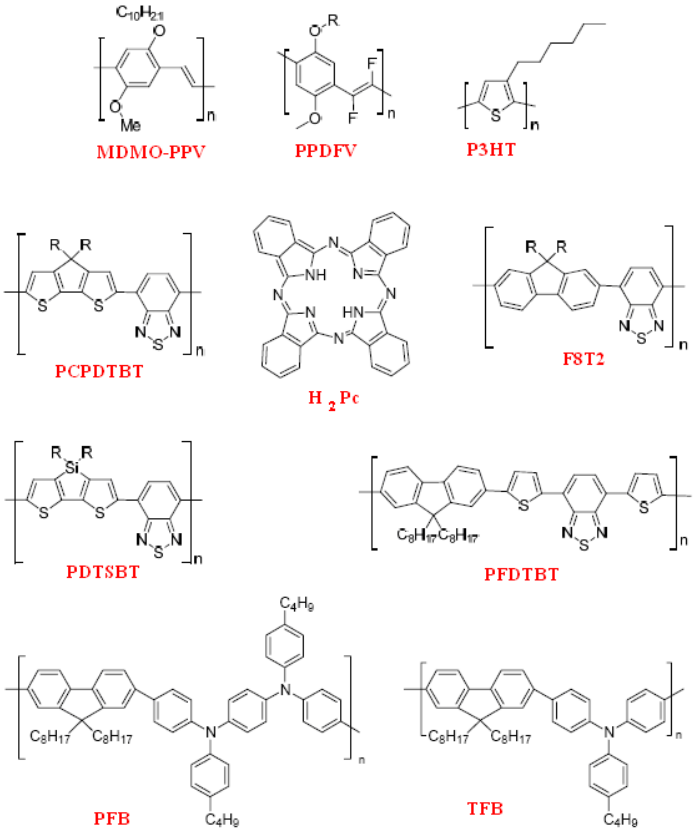

Fig. 2.4. Donor polymer semiconductors (p-type) were reported in [4, 6].

2.2.3. Semiconductor acceptor molecules

Acceptor material is that in which electrons are transported and which receives electrons from donor material. Examples of this kind of material are small molecule polymers to whose structure have been added CN and thiazole groups. In general fullerene families such as C60, PCBM $PC_{70}BM$, etc., are used, which have high electron affinity. [7] Donor and acceptor materials must meet some requirements if they are to be applied in organic solar cells. **Fig. 2.5** shows the representative acceptor materials. [8]

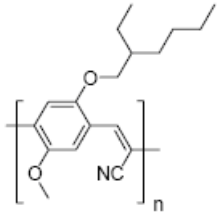

CN-MEH-PPV

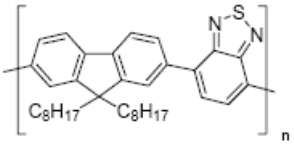

F8BT

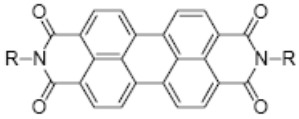

R-Ptcdi

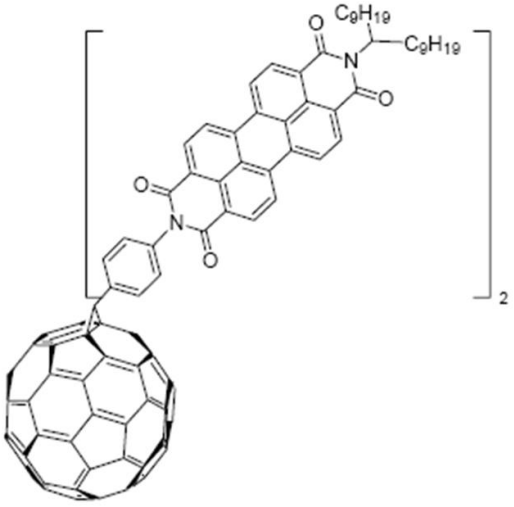

Fullerene- perylene

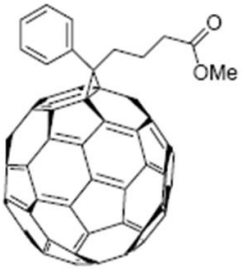

PCBM 60

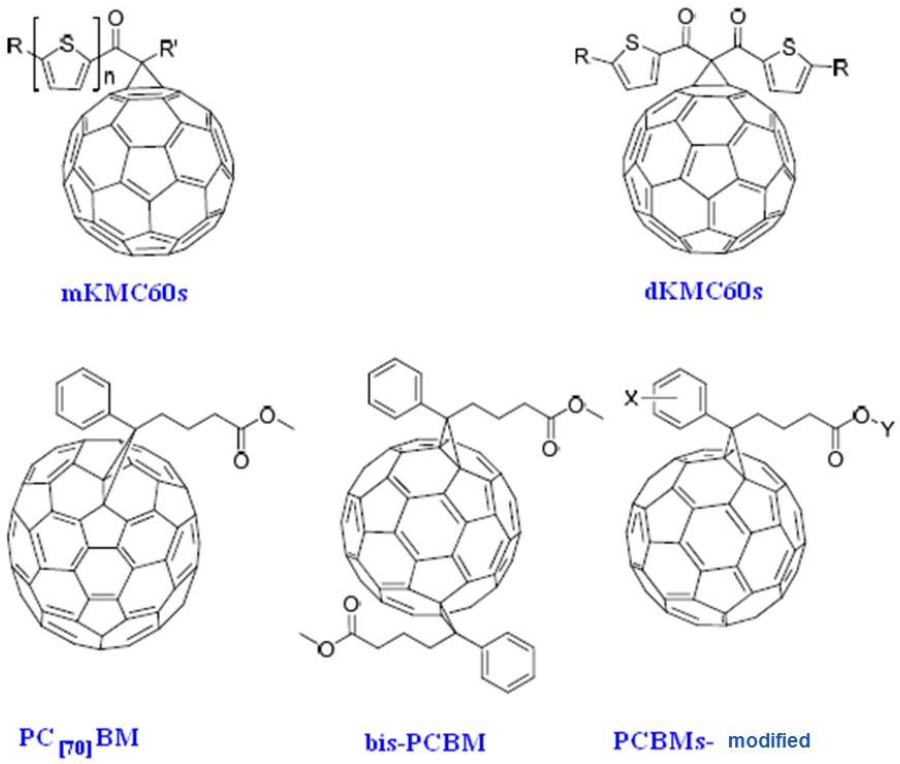

Fig. 2.5. Acceptor semiconductors (n-type) were reported in [7, 8].

2.3. Selection of semiconductor materials for organic solar cells

The material for this thesis was selected on the bases of a previous study of the chemical, physical and optical properties described in the literature as well as the benefits obtained by different researchers and provided by the infrastructure and technology in our laboratories.

The semiconductor materials selected for manufacturing the organic solar cell configurations presented in the thesis were poly (3-hexilthiophene)

(P3HT), poly[[4,8-bis (octyloxy) benzo [1,2-b:4,5-b'] dithiophene-2,6-diyl] [2-[(dodecyloxy) carbonyl] thieno[3,4-b]thiophenediyl]] (PTB1) was used as p-type semiconductor material and the fullerene [6,6]-phenyl C_{61}-butyric acid methyl ester (PCBM) and fullerene [6,6]-phenyl C_{71}-butyric acid methyl ester ($PC_{70}BM$) as n-type semiconductor material. [7, 9] The structures chosen were bulk heterojunction (BHJ), bilayer (BL), nanostructured (NS). These structures will be presented in the following chapters of this thesis.

In this section, we will present the chemical and physical properties of the semiconductor materials used to manufacture the organic solar cells.

2.3.1. Properties of PEDOT:PSS

Poly (3,4-ethylenedioxythiophene) / poly (styrenesulfonate) (PEDOT : PSS) is a mixture of two monomers. Poly (3,4-ethylenedioxythiophene) or PEDOT is a conjugated polymer with a high conductivity of 750 S/cm [10], but which is highly insoluble.

The other component is a colloid in an aqueous solution of sodium polystyrene sulfonate, an insulator which dilutes the PEDOT. Islands of PEDOT form inside the PSS matrix, and the product can be diluted in water. The product is used as a synthetic metal, and can be deposited by spin-coating, ink printing and other techniques.

As was seen **Fig. 2.6,** its chemical structure is complex. It is optically transparent to visible light of 80% and although a relatively good conductor, its conductivity is five times lower than that of ITO and is another transparent synthetic metal. Some modifications have been made so that its conductivity is about 160 S / cm [10, 11].

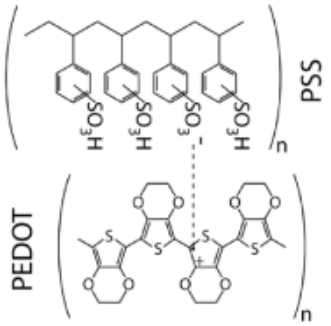

Fig. 2.6. Chemical structure of PEDOT:PSS.

2.3.2. Properties of P3HT

P3HT is formed by the thiophene and an alkyl functional group. The hexyl group is at third carbon of the thiophene (see **Fig. 2.7**).

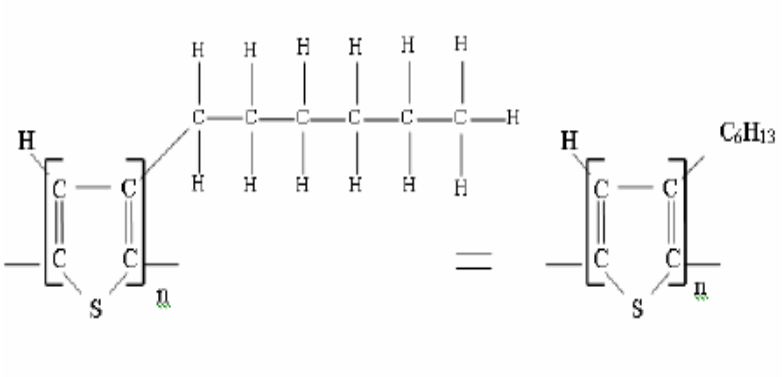

Fig. 2.7. Chemical structure of P3HT.

The hexyl radical makes the polymer soluble, processable and stable. Polymers whose functional groups are alkyls are known as poly (3-alkylthiophenes). Other examples of these compounds are the poly (3-octylthiophene) (P3OT), poly (3-decylthiophene) (P3DT) and poly (3-hexadecylthiophene) (P3HDT). [11]

The P3HT presents a low optical Eg of about 1.7 and 1.8 eV, and achieves a degree of regioregularity in which the hole mobility, according Sirringhaus, is 1 cm^2 / V-s when deposited on SiO_2. [12] Even when it is deposited on polymers the mobility values are around $1x10^{-2}$ cm^2 / V-s. Mobility is an important factor that determines the efficiency of the solar cell.

Regioregularity (RR) is defined as the degree of order of the polymer chain (structural ordering). There are two types: head-tail and tail-tail. Head-tail regioregularity is preferred because it improves the polymer conjugation structure and it allows the interchange of charge carriers, while the tail-tail regioregularity configuration does the opposite.

Higher RR in P3HT improves the mobility of the charge carriers and also reduces the optical band-gap. [13] A smaller optical band-gap in P3HT means that more photons can be absorbed from the solar spectrum.

P3HT is unstable in the presence of oxygen or water vapour, and its conductivity can increase when reacting with them, so it needs to be handled under inert environments (i.e. glove box under nitrogen) or encapsulation to prevent the polymer from degrading. P3HT polymer can be diluted using di-chlorobenzene, chlorobenzene and chloroform where the solubility values are 20.5, 19.4 and 18.7 respectively.

2.3.3. Properties of PTB1

The PTB1 polymer is synthesized via Stille polycondensation using an ester substituted 2,5-dibromothieno[3,4- b] thiophene and dialkoxyl benzodithiophene distannane monomers. The complete name of this polymer is poly [[4,8-bis (octyloxy) benzo (1,2-b:4,5-b') dithiophene-2,6-diyl) (2-((dodecyloxy) carbonyl) thieno(3,4-b) thiophenediyl]]. Molecule PTB1 is shown in **Fig. 2.8.** Quinoidal structure in PTB1 is stabilized by the

incorporation of thieno[3,4-b]thiophene units in backbone, as results PTB1 shows a low band gap.

Thieno[3,4- b]thiophene makes the polymer soluble and oxidative stable. Molecular weight is 22.9 kg/mol with a polydispersity of 1.25. The polymer solution in o-dichlorobenzene is reported with an absorption maximum at 682 nm with the onset at 774 nm. In solid film, the polymer exhibits slightly red-shifted absorption around 690 nm with the onset at 784 nm, which coincides with the corresponding maximum photon flux region in solar spectrum ~700 nm. The absorption coefficient in polymer film at 690 nm is 7.5×10^{-3} nm^{-1}. Optical band gap reported ~1.62 eV. Energy levels of highest occupied molecular orbital (HOMO) and the lowest unoccupied molecular orbital (LUMO) were reported of -4.90 and -3.20 eV, respectively. [14, 15]

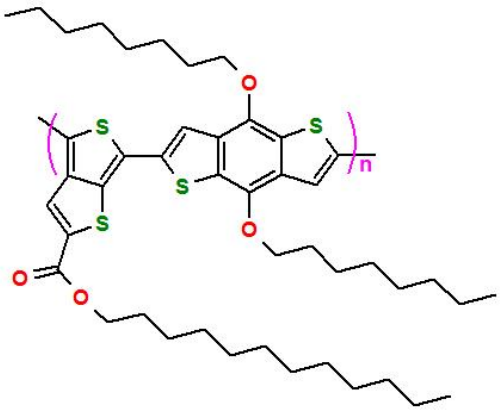

Fig. 2.8. Chemical structure of PTB1.

2.3.4. Properties of PCBM and $PC_{70}BM$

The $PC_{70}BM$ and PCBM the molecule of which has a diameter ~ 0.7 nm, is a derivative of fullerene. Fullerenes are soluble in some organic solvents and insoluble in polar solvents or hydrogen bonds (water). Their density is

about 1.68 g / cm^3. They have a high electron affinity. [16] The alkyl chain of fullerene makes it soluble enough to mix with the polymers. [17] The diluents used for the fullerenes are anisole, chlorobenzene and chloroform because solubility values were around of 20 for the PCBM and 19.46, 19.4 and 18.7, respectively, for the diluents. The structure of the molecule was represented in **Fig. 2.5**.

2.3.5. Selection of materials for electrical contacts

The materials selected as electrical contacts for the final device were calcium and silver because good ohmic contact is necessary to collect charge carriers after they have been generated. More detail will be shown in the chapters below.

2.4. Photovoltaic parameters

The characterization of solar cells is important not only for controlling the manufacturing process but also for the development of new technologies. A wide range of characterization techniques are used for photovoltaic devices. Generally, they extract the parameters of solar cell and study its structure and the materials of which it is made up. [18] In this thesis we will use electrical and optical characterization to characterize first the layers and then the structures.

The main cell parameters are obtained by applying J-V curves in light and dark conditions, see **Fig. 2.11**.

2.4.1. Ideal solar cell

The current through an ideal solar cell can be expressed by:

$$I = I_L - I_o * \left(e^{\frac{qV}{nkT}} - 1 \right) \qquad (2.1)$$

where I_L is the photocurrent, I_o is saturation current, n is the ideality factor and k is the Boltzmann constant.

The saturation current reflects the behavior of the charges that can overcome the energy barrier in reverse bias at the junction and depends on the height of the barrier formed, the density of minority charge carriers in the vicinity of the barrier and the temperature. In general, saturation current is extracted from Eq. 2.1, in which the values must fit with the J-V experimental curve. If I_o is constant for a specific temperature (T) the charge transport is by diffusion which dominates over the recombination transport, as is the case of Germanium diodes. In polymers recombination dominates over diffusion, so this parameter is not constant but varies with voltage. The higher the diode recombination, the greater I_0 will be. [19, 20]

Therefore, Eq. (2.1) can be rewritten as:

$$I = I_o(T) \cdot (e^{\frac{qV}{nkT}} - 1) \qquad (2.2)$$

where I_0 can be represented as:

$$I_o = I_{oo} \exp \frac{-E_a}{kT} \qquad (2.3)$$

q is the electron charge, V is the applied voltage, n is the ideality factor, k is Boltzmann constant, T is the temperature, Ioo is a constant and E_a is the activation energy of the saturation current.

In real solar cells, the presence of parasitic resistances reduces their efficiency. The most common parasitic resistances are series resistance (R_S) and shunt resistance (R_{sh}). [21, 22]

The series resistance in a solar cell may be due to the resistance of the active layer or resistance between the metal contacts. In the first case, the resistance depends on the resistivity and thickness of the active layer, and the presence or absence of a space charge. The R_s will be extracted from J-V curve.

Shunt resistance, on the other hand, is caused by leakage currents in the peripheral device or by localized defects that may have occurred in the manufacturing process or short circuits in the metallization of the contacts near the junction.

The ideality factor n reflects the dominant transport mechanism on the diode and is obtained by determining the slope of log (J) versus V. In general the curve can show one or several slopes in regions other than that of the voltage applied, which indicates that the dominant transport mechanism can vary with the voltage. If n = 1, the transport mechanism into the active layer is by diffusion or metal-semiconductor junction is formed. If n = 2, the transport mechanism is by recombination. If n > 2 can be associated with the presence of deep and shallow traps in the bulk of the active layer. [23] In some cases, the J-V curve cannot show linear regions or too high values of n. These can be re-analyzed by applying other models the structure and using other elements.

2.4.2. Electrical equivalent circuit diagrams

The simplest equivalent circuit for representing the various elements of the solar cell is shown in **Fig. 2.9.** [24]

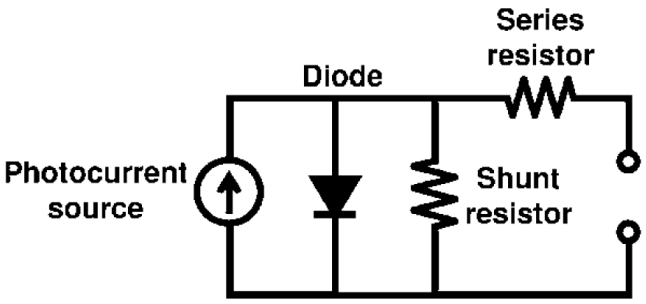

Fig. 2.9. Equivalent circuit used in typical organic solar cells.

Other models may involve some loss mechanism during charge transport inside the solar cells. For instance, the effects of space-charge limited current (I_{SCLC}) can be incorporated as is shown in **Fig. 2.10**. In this case a second diode is added with its respective shunt resistance.

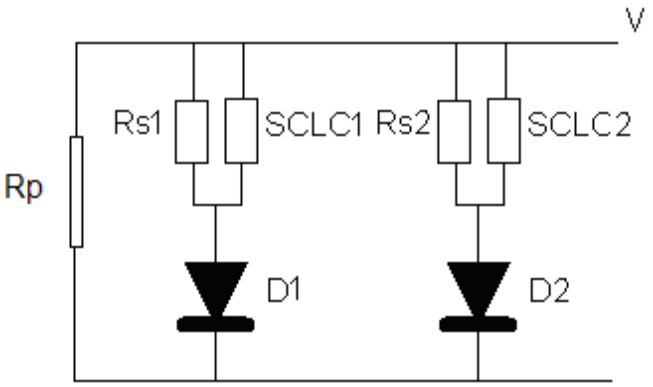

Fig. 2.10. Equivalent circuit which incorporates the I_{SCLC} and one additional diode in parallel to represent other phenomena that may occur in the structure of the cell.

2.5. Main performance parameters of organic solar cells

The basic parameters of organic solar cells are obtained from the J-V characteristic under light and dark conditions. Typical J-V curves are shown in **Fig. 2.11**.

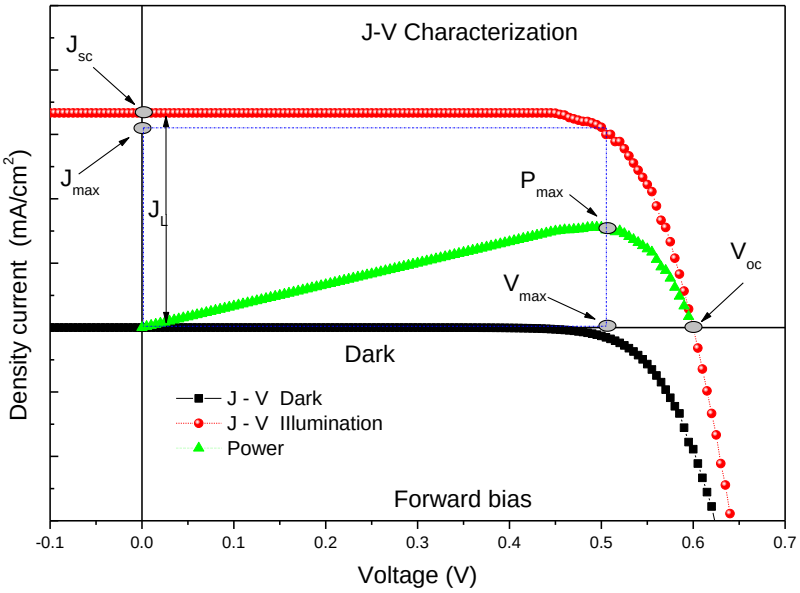

Fig. 2.11. J-V characteristic under dark and light at 1 sun (100 mW/cm^2).

2.5.1. Open circuit voltage (Voc)

The open circuit voltage (Voc) is the maximum voltage available in the solar cell under standard illumination when the current does not flow. The value is determined when the J-V obeys the following condition (see **Fig. 2.11**).

$$J(V_{oc}) = 0 \qquad (2.4)$$

2.5.2. Short circuit current density (J_{SC})

Short circuit current density (J_{sc}) is the current through the solar cell when the voltage across its terminals is zero: that is, when the cell is in short circuit. [25] This parameter is determined in **Fig. 2.11** by the condition:

$$J_{sc} = |J(V = 0)| \quad (2.9)$$

J_{sc} is caused by the generation and collection of light-generated carriers. For an ideal solar cell is not considered the loss of charge carriers. Jsc and the current caused by all the light-generated carriers J_L, can be considered identical. [26] Therefore J_{sc} is the largest current that can be extracted from the solar cell. [27]

J_{sc} depends on such factors as [27-29]:

1. The area of the solar cell
2. The number and energy of the incident photons
3. The thickness of the active layer, since some of the light energy can traverse the active layer without being absorbed
4. The spectrum of the incident light
5. The optical properties of the layers on which light is incident, that is, reflection and absorption
6. The probability of charge collection in the solar cell that include the carrier recombination, layer morphology, type of structure used, properties of the metal contact, among others.

If the short circuit current of the organic solar cell is to be compared with other similar structures the areas need to be standardised. The short circuit current density (Jsc, A/cm^2) is obtained by dividing Isc by the area For most solar cell measurements the spectrum is normalized to AM 1.5G.

2.5.3. Maximum power P_{max} (I_{max} & V_{max})

The power produced by the cell is calculated as:

$$P = I(V)*V \qquad (2.5)$$

The point of maximum power (P_{max}) is determined by searching for the maximum value of I (V) x V, as is shown in **Fig. 2.12**. The line formed by the filled rectangles represents the power curve where this peak is observed. Once P_{max} has been located, it is possible to determine the maximum current I_{max} and the maximum voltage V_{max}. [19]

2.5.4. Fill factor (FF)

The J_{sc} and V_{oc} are the current and voltage peak of the solar cell, respectively. At these points power is zero. The fill factor (FF) is, together with the V_{oc} and J_{sc}, a basic parameter of the characteristics of the solar cell. The FF is defined as:

$$FF = \frac{J_{max} * V_{max}}{J_{sc} * V_{oc}} = \frac{A1}{A2} \qquad (2.6)$$

Graphically FF is the ratio between the A1 and A2 areas shown in **Fig. 2.12.** If the ratio of these two areas is close to 1, the power delivered by the solar cell is almost ideal. The theoretical maximum of FF can be determined from condition [19]:

$$\frac{d(V * I)}{dV} = 0 \qquad (2.7)$$

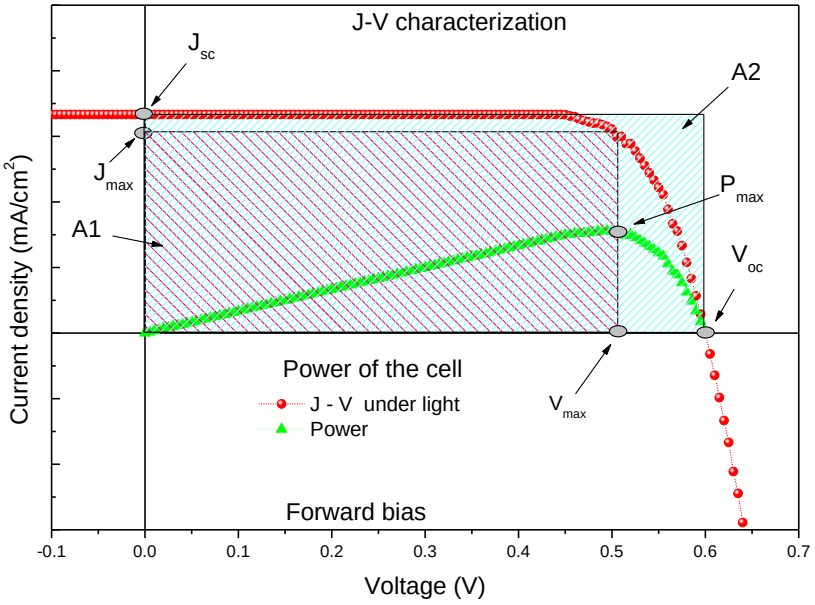

Fig. 2.12. Graphic representation obtained for FF in a typical J-V characteristic.

2.5.5. Power conversion efficiency (PCE)

The efficiency is the parameter used to evaluate the performance of the organic solar cell. It is defined as the ratio between the output power and the incident light supplied to the solar cell. The PCE depends on the intensity of the incident sunlight (wavelength λ) and temperature (T). Therefore, the conditions under which the solar cell is measured must be carefully controlled so that the performance parameter can be compared with that of the other devices. Solar cells are measured under standard AM1.5 G conditions and at a room temperature of 24 °C. The PCE is determined using the formula:

$$PCE = \frac{P_{máx}}{P_{Light}} = \frac{I_{\max} * V_{\max}}{P_{Light}} \qquad (2.8)$$

Solving to P_{max} from 2.5 and substituting in 2.8 we get:

$$PCE = \frac{J_{sc} * V_{oc} * FF}{P_{Light}} \qquad (2.9)$$

Fig. 2.13 shows the effect of R_s and R_p on J-V curves.

The main effect of R_s is to reduce the FF, although excessive values also affect the J_{sc}. [22] If R_p is low, the current through the heterojunction is reduced, which causes a loss in output power and a reduction in FF and PCE.

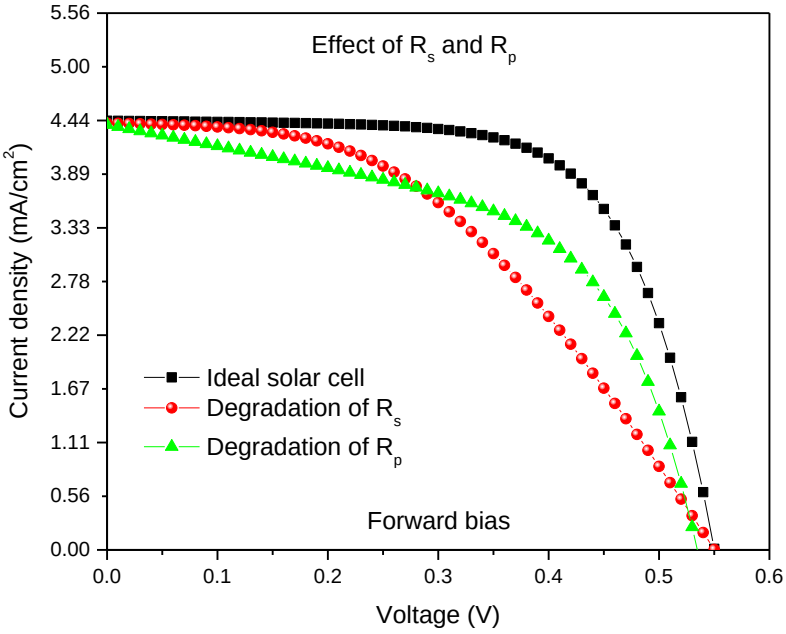

Fig. 2.13. Effect of series and shunt resistances on organic solar cells under light conditions.

2.5.6. Rectification ratio (RR)

The rectification ratio is the ratio of the current at a particular direct voltage to the same voltage and reverse bias.

$$RR = \left(\frac{J_{Forward\ \ bias}}{J_{Reverse\ \ bias}} \right)_V \qquad (2.10)$$

2.6. References

[1] H. Klauk, Organic Electronics Materials, Manufacturing and Applications, Edit. WILEY-VCH Verlang GmbH & Co. KGaA, Edition 1st, (2006).

[2] J.C. Sanchez, Master Thesis, Characterization of Organic materials for Electroluminescence Diodes (OLEDs), SEES CINVESTAV, January (2007).

[3] C.W. Tang and A.C. Albrecht, Photo voltaic effect of metal – chlorophyll-a-metal sandwich cells, *J. Chem. Phys., 62* (1975) 2139–2149.

[4] J.C. Novas, E. Armelin, J.I. Iribarren, C. Aleman, F. Liesa, La modelización molecular como herramienta para el diseño de nuevos polímeros conductores, *Red de revistas Científicas de America Latina y del Caribe, España y Portugal, vol 15* (2005) 239–244.

[5] J.C. Brabec, G. Srinivas, J.MJ. Halls, L. Darin, J. Shijun, P.W. Shawn, Polymer-Fullerene Bulk-Heterojunction Solar Cells, *Adv. Mater., 22* (2010) 3839–3856.

[6] H. Shirakawa, Angew, The Discovery of Polyacetylene Film: The Dawning of an Era of Conducting Polymers (Nobel Lecture), *Chem. Int. Ed. 40* (2001) 2575.

[7] B.A. Greeg, Excitonic Solar Cells, *J. Phys. Chem. B 107* (2003) 4688–4698.

[8] Y. Dong, Bundang-gu, Seongnam-si, Gyeonggi-do, Next- Generation Organic Solar Cell Technology and Market Forecast, February (2010) 463–828.

[9] V.S. Balderrama, M. Estrada, P.L. Han, P. Granero, J. Pallarès, J. Ferré-Borrull and L.F. Marsal, Degradation of Electrical properties of

PTB1:PCBM solar cells under different environments, *Sol. Energy Mater. Sol. Cells 125* (2014) 155–163.

[10] C. Yi-Ying, W. Leeyih, S. Wei-Fang, Polymer solar cell with poly(3,4-ethylenedioxythiophene) as transparent anode, *Org. Electron., 9* (2008) 968–973.

[11] J.S. Henry, H. Kenrick, M. Chiesa, R.H. Friend, Morphological and electronic consequences of modifications to the polymer anode PEDOT:PSS, *Polymer 46* (2005) 2573–2578.

[12] H. Sirringhaus, P.J. Brown, R.H. Friend, M.M. Nielsen, Two-dimensional charge transport in self-organized, high-mobility conjugated polymers, *Nature 401* (1999) 685–688.

[13] T. Chen, X. Wu, R.D. Rieke, Regio-controlled Synthesis of Poly(3-Alkylthiophenes) Mediated by Rieke Zinc: Their Characterization and Solid-State Properties, *J. Am. Chem. Soc., 117* (1995) 233–244.

[14] J. Hou, H.-Y. Chen, S. Zhang, G. Li, Y. Yang, Synthesis, Characterization, and Photovoltaic Properties of a Low Band Gap Polymer Based on Silole-Containing Polythiophenes and 2,1,3-Benzothiadiazole, *J. Am. Chem. Soc., 130* (2008) 16144−16145.

[15] Y. Liang, Y. Wu, D. Feng, S.T. Tsai, H.J. Son, G. Li, L. Yu, Development of new semiconducting polymers for high performance solar cells, *J. Am. Chem. Soc., 131* (2009) 56−57.

[16] F. Langa and J. F. Nierengarter, Principles Fullerenes and applications, Edit. The Royal Society of Chemistry, (2007), Printed by Henry Lings Ltd. Dorchester Dorset, U.K.

[17] D. Sukeguchi, S.P. Sing, M.R. Reddy, H. Yoshiyama, New diarylmethanofullerene derivatives and their properties for organic thin film solar cells, Beilstein *J. Org. Chem.*, 5 (2009) No.7 1–12.

[18] K. Takahashi, M. Konagai, Amorphous Silicon Solar Cells, Edit. North Oxford Academic A division of Kogan Page, Edition 1st (1986).

[19] A. Muñoz-Lasso, Modelo Circuital de células Solares de Película Delgada, *Tecnociencia*, *5* (2003) 33–50.

[20] C. Waldauf, M.C. Scharber, P. Schilinsky, J.A. Hauch, and C. J. Brabec, Physics of organic bulk heterojunction devices for photovoltaic applications, *J. Appl. Phys.*, *99* (2006) 104503.

[21] I. Torres, Celdas Solares de alto rendimiento, Universidad de Pamplona, Ciudad Universitaria, Bloque reingeniería, Jdlemos@udea.edu.co, (1992).

[22] K. Petritsch, PhD Thesis Organic Solar Cell, Technisch-Naturwissenschaftliche Fakultät der Technischen Universität Graz (Austria), Cambridge and Graz, July (2000).

[23] M. Bashahu, P. Nkundabakura, Review and test of methods for the determination of the solar cell junction ideality factors, *Sol. Energy*, 81 (2008) 856–863.

[24] A. Checknane, H.S. Hilal, F. Djeffal, B. Benyoucef, J.P. Charles, An equivalent circuit approach to organic solar cell modeling, *Microelectron. J.*, *39* (2008) 1173–1180.

[25] J. Merten, J. M. Asensi, C. Voz, A. Shah, R. Platz, J. Andreu, Improve Equivalent Circuit and Analytical Model for Amorphous Silicon Solar Cells and Modules, *IEEE Trans. Electron Devices*, *45* (1998) 423–429.

[26] A.L. Fahrenbruch, R.H. Bube, Fundamentals of solar cells, Edit. Academica Press Inc., Edition 1st, (1983).

[27] M.A. Green, Solar Cells Operating Principles, Technology, and System Applications, Edit. Prentice Hall Series in Solids State Physical Electronics, edition 1st (1982).

[28] H.J. Hovel, Solar Cells, Vol.11, Edit. Academic Press New York – San Francisco London (1975).

[29] S.J. Fonash, Solar Cell Device Physic, Edit. Academic Press, Inc., New York E.E.U.U. (1981).

Chapter 3

Degradation analysis of P3HT:PCBM blend layers in combination with electrical model

Polymeric solar cells have attracted much attention during the last years due to their lower fabrication cost and possibility of using flexible substrates. The efficiency reported until now is less than 12%. Among factors affecting polymeric solar cells efficiency, the active layer morphology related to blend preparation and annealing, is one of the most important. In this chapter we analyze the behavior of solar cells based on poly (3-hexylthiophene:[6,6]-phenyl-C_{61}-butyric acid methyl ester, P3HT:PCBM blends prepared under different conditions. Basic parameters are extracted from measured characteristics in dark and under illumination, while modeling is used to understand the mechanisms involved in the device behavior.

3.1. Introduction

Polymeric solar cells during the last years have been fabricated where is tried to improve their efficiency, and maintaining the low cost fabrication. Many factors have been reported to affect solar cells parameters, among which the active layer morphology, related to blend preparation and annealing, is very important. [1-4] From another point of view, modeling of solar cells has also attracted much attention trying to predict the device behavior, as well as variations of its electrical parameters with device processing. Equivalent circuits (EC) that are generally used to describe solar cells can consider 1, 2 or more junctions, plus series and shunt resistances, where elements can be associated to physical mechanisms. [5, 6]

Several polymers, methanofullerenes and their blends have been studied as the active layer of polymeric solar cells. [7-12] Among them, blends of poly (3-hexylthiophene) (P3HT) and [6,6]-phenyl-C_{61}-butyric acid methyl ester (PCBM) are providing among highest reported efficiencies, in the order of 5 %. Cell parameters are very sensitive to small variations in blend preparation, as for example, ratio of P3HT to PCBM, solvent, temperature during preparation, film thickness, time during the stirring and annealing. [4] For these reason, characterizing the active layer morphology is of much importance to device improvement.

In this chapter we have analyzed the behavior of solar cells based on P3HT:PCBM blends prepared under different conditions. Basic parameters are extracted from measured characteristics in dark and under illumination. Modeling is used to understand mechanisms involved in the device behavior and its degradation, after been left in ambient conditions for several days. Cells are compared regarding the mechanisms involved in the dissociation of charges,

as well as regarding their series resistance, shunt resistance, open circuit voltage V_{oc} and short circuit current I_{sc}, as prepared and after several days working in ambient conditions.

3.2. Materials and methods

This section is shown how was the preparation of different solutions that were used to manufacture the different photovoltaic devices. After, the solar cells are electrically characterized under dark and under illumination. The conditions to do these studies are described below.

3.2.1. Experimental

Solar cells were prepared by spin-coating a poly(3,4-ethylenedioxythiophene) poly(styrenesulfonate), PEDOT:PSS, layer on top of an indium tin oxide (ITO) substrate, over which the active layer of a P3HT:PCBM blend was spin-coated, followed by annealing and thermal evaporation of aluminium. The active layer blend was prepared in 2 ways.

Blend 1.-- 4.8 mg of PCBM were diluted in 0.6 ml of chlorobenzene, stirring during 2 hours at room temperature, after which, 6 mg of P3HT were added to prepare a (1:0.8) wt% blend. The solution was left stirring for 18 hours at room temperature. Before spin coating, the solution was heated to 60 ^{o}C for 5 min.

Blend 2.-- 8 mg of P3HT were dissolved in 0.85 ml of chlorobenzene, stirring for 3 hours at 60 ^{o}C, alter which 8 mg of PCBM were added and the solution was left stirring at 60 ^{o}C for 18 hours, to obtain a (1:1) wt% P3HT:PCBM blend.

The solar cells were prepared as follows:

A photolithography was done to the glass substrates with a previous deposited ITO layer, in order to define ITO regions. The next step was to deposit by spin-coating a PEDOT:PSS Baytron-P layer of less than 50 nm and annealed it at 110 ^{o}C during 5 min. The P3HT:PCBM blend, prepared using one of the indicated above procedures, is then spin coated to provide a layer thickness around 100 nm. Both layers are eliminated from the borders of the substrate before metal deposition. Finally, aluminium contacts are deposited through a shadow mask to form the final structure. A final annealing is done at 150 ^{o}C for 2 min. The cell area is a square of 3 mm by 3 mm. Two substrates, with 4 cells on each one were fabricated with each blend.

3.2.2. Conditions and electrical characterization

Dark and under illumination at 1 sun I-V characteristics were measured in N_2 just after fabrication. Samples were left 3 days in ambient conditions without encapsulation and measured again in N_2.

To understand the mechanisms involved in device behavior right after fabrication and after its degradation, dark and illuminated I-V curves were modeled using an equivalent circuit. Extracted parameters were got and they are shown in next paragraph.

3.3. Results and discussion

In this section, we have demonstrated that the preparation of different blend solutions have an important influence on the performance parameters of the devices. Depending of the environment exposed the devices in this case

under nitrogen and air environment with a short period of time, the devices presented a degradation ratio.

3.3.1. I-V characterization under light and dark

Fig. 3.1 shows the electrical equivalent circuit used to describe dark and illuminated I-V characteristics, where D2 represents the P3HT:PCBM heterojunction, D1 represents a Schottky diode associated to regions of P3HT in contact with aluminium, where a rectifying contact is formed and charge dissociation can also occur. Rs1 and Rs2 are series resistance associated to diode D1 and D2 respectively and Rsh2 is the overall shunt resistance. The element SCLC incorporates the effect of space charge limited current which has to be considered as bias is increased.

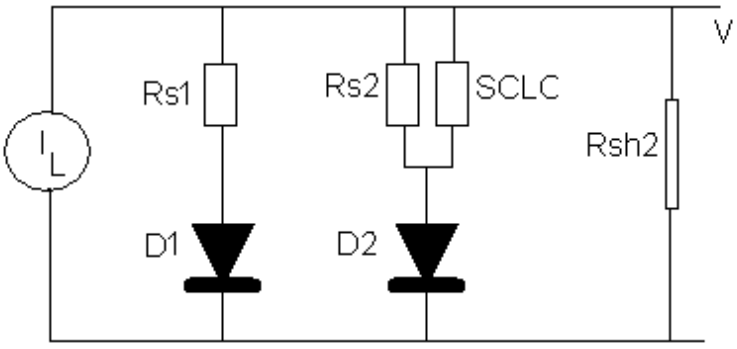

Fig. 3.1. Equivalent circuit for modeling cells I-V characteristics. D1 and D2 are diodes to represent two rectifying mechanism; Rs1 and Rs2 are the series resistance associated to D1 and D2 respectively; Rsh2 the shunt resistance resultant for the overall cell structure; the element SCLC incorporates the effect of space charge limited current and I_L represents the effect of light**.**

The SCLC current is expressed as usual [4]:

$$I_{SCLC} = k \cdot \left(\frac{V - V_D}{Vo} \right)^m , \qquad (1)$$

where V is normalized to $V_o=1$ V, and V_D is the voltage across the diode, while k and m are fitting parameters. I_L represents the current due to illumination.

Fig. 3.2 shows measured and modeled dark I-V curves, while the **Fig. 3.3** shows the I-V curves under illumination for cells fabricated with the two blends. The effects of degradation after three days working in ambient conditions are also shown.

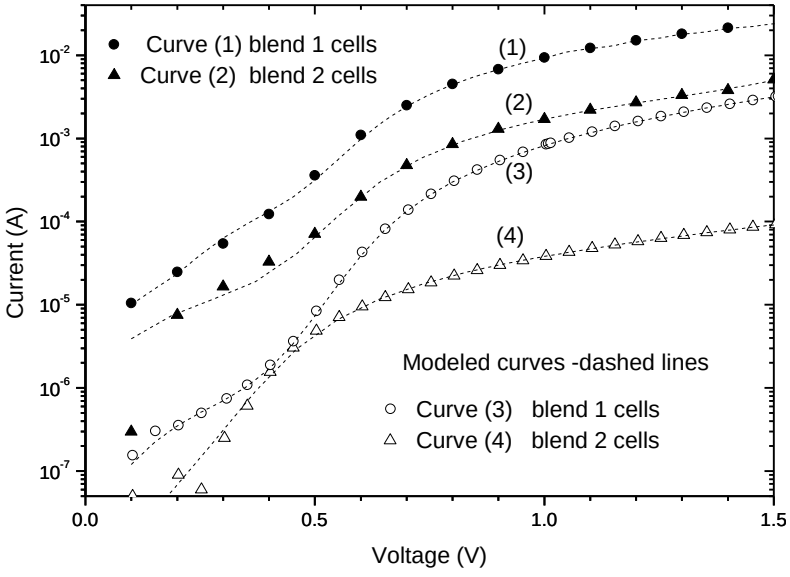

Fig. 3.2. Measured and modeled cells I-V characteristics in dark conditions; curves (1) and (2) correspond to devices just after preparation; curves (3) and (4), after 3 days working in ambient conditions.

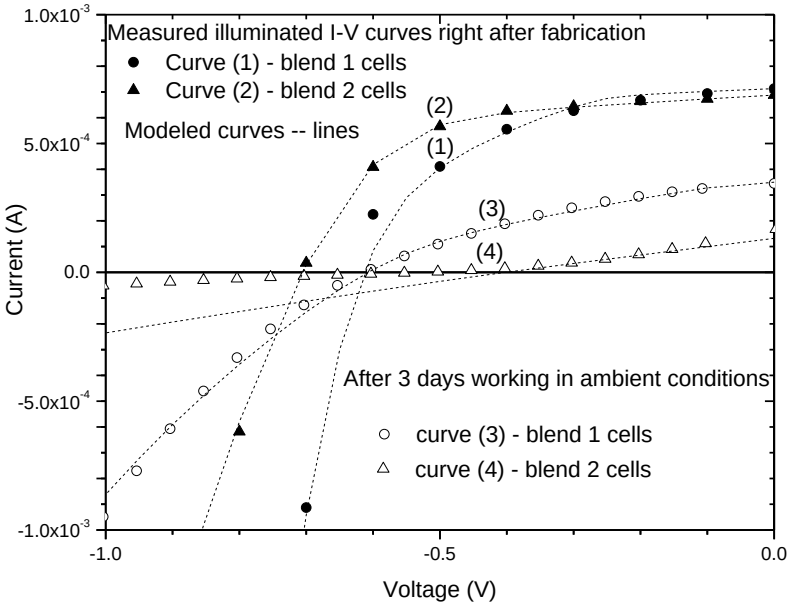

Fig. 3.3. Measured and modeled characteristic I-V curves under illumination for the same devices shown in Fig 3.2; curves (1) and (2) correspond to devices just after preparation; curves (3) and (4), after 3 days working in ambient conditions**.**

Table 3.1 shows extracted model parameters for a representative cell prepared with each blend working in dark conditions, right after preparation and after 3 days in ambient conditions. Table 3.2 shows extracted model parameters of the same cells in Table 3.1, working under illumination.

First of all, it was noticed that I-V curves of cells prepared with blend 2 can be modeled using only diode D2, obtaining the ideality factor around n2=2 which suggests the presence of a recombination process associated to the heterojunction at the interface of P3HT and PCBM regions. I-V curves of cells fabricated with blend 1, required two diodes, D1 and D2, in order to obtain precise modeling. The ideality factor of D1 was around n_1=1 and for D2 again around n_2=2, which suggests the presence of a metal semiconductor junction in addition to the heterojunction, for dissociating the excitons.

Blend	n_1	I_{01} [A]	R_{S1} [Ω]	n_2	I_{02} [A]	R_{S2} [Ω]	R_{SH2} [Ω]	k2 [A]	m2
1	1	$3x10^{-10}$	$1.8x10^{3}$	1.9	$8x10^{-9}$	34	$9x10^{3}$	$2x10^{-3}$	3
1a	1	$3x10^{-10}$	$4.5x10^{5}$	1.9	$3x10^{-10}$	360	$1x10^{6}$	$2.7x10^{-3}$	2
2	-	-	-	2.1	$8x10^{-9}$	220	$2.5x10^{4}$	$3x10^{-3}$	3
2a	-	-	-	2.1	$1.3x10^{-9}$	12000	$9x10^{6}$	$2.5x10^{-5}$	3

Table 3.1. Model parameters for all blends, as prepared and after degradation, measured under dark conditions. n_1 and n_2 are the ideality factors; I_{01} and I_{02} are the saturation currents for diodes D1 a D2. R_{S1} and R_{S2} are the series resistance associated to D1 and D2 respectively; R_{SH2} the shunt resistance resultant for the overall cell structure; *k* and *m* are fitting parameters associated to each diode.

Blend	n_{1il}	I_{01il} [A]	R_{S1il} [Ω]	n_{2il}	I_{02il} [A]	R_{S2il} [Ω]	R_{SH2il} [Ω]	$k2_{il}$ [A]	m_{2il}	V_{OC} [V]	I_{SC} [mA]
1	1	$2x10^{-10}$	800	2.1	$8x10^{-9}$	28	$9x10^{3}$	$2.5x10^{-3}$	2	0.6	0.7
1a	1	$2x10^{-10}$	1600	2.1	$3x10^{-10}$	320	$5x10^{3}$	$3x10^{-3}$	2	0.6	0.35
2	-	-	-	2.1	$5.0x10^{-9}$	124	$9x10^{3}$	$4x10^{-3}$	3	0.7	0.69
2a				2.1	$1x10^{-10}$	5000	$6x10^{3}$	$4x10^{-3}$	3	0.5	0.17

Table 3.2. Model parameters for all blends, as prepared and after degradation, measured under illumination conditions. V_{OC} is the open circuit voltage and I_{SC} is the short circuit current. The rest of the parameters in which the sub index il was added, have the same meaning as in Table 3.1 but correspond to the cell working under illumination.

3.3.2. Analysis of behavior of the blend layers with the model

The different behaviors on the devices fabricated with both blend solutions used can be explained considering that the phase separation of the

constituents of the blend can give rise to different regions in the active layer, among which we can distinguish the following situations:

1) PCBM regions that contact the Al electrode and P3HT; 2) PCBM Regions that contact PEDOT:PSS electrode and P3HT; 3) PCBM regions surrounded only by P3HT, which do not contact any of the two electrodes; 4) PCBM regions that contact P3HT and both electrodes. A schematic representation of these regions is shown in **Fig. 3.4 a**.

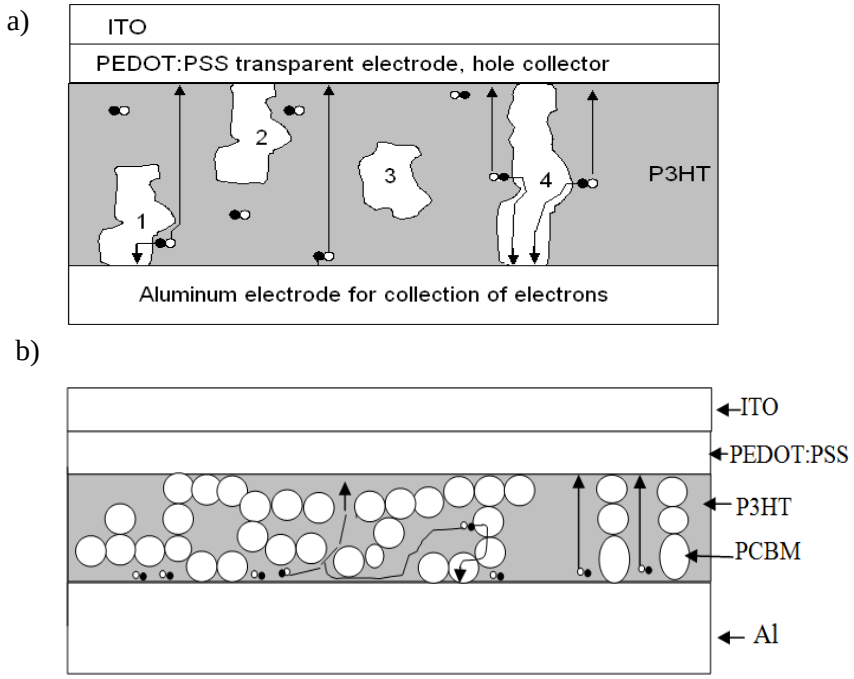

Fig. 3.4. a) Schematic representation of some possible distributions of PCBM regions inside the active blend: colored regions correspond to P3HT where photons are absorbed and holes (open circles), are transported to the transparent electrode. Non-colored regions correspond to PCBM, where electrons (black circles) are transported toward the cathode Al electrode. Generated excitons are dissociated at the distributed heterojunctions or at the Schottky junctions formed between Al and P3HT. Arrows indicate the direction of charge transport for recollection at the electrodes; b) Schematic

representation to show the increase in pass length of holes dissociated at the Schottky diode in a more interpenetrated morphology of the blend.

The PCBM in the first type of regions will provide the path for electrons injected from the P3HT regions, to be collected at the Al electrode. The holes will travel across the P3HT region to be collected at the PEDOT:PSS electrode. Excitons generated by the incident light within the P3HT layer at less then 10 nm from these PCBM regions, will be capable of reaching the interface between P3HT and PCBM, dissociate at the heterojunction and travel through the respective paths toward the corresponding electrode.

As these regions extend more toward the surface, they will be able to receive and dissociate more of the excitons generated across the complete width of the active layer. If they contact both electrodes, as in case 4, they will provide complete recollection of excitons generated within 10 nm and along the depth of the active layer, effect that can be described by diode D2.

Regions described in cases 2 and 3, will not provide a path for electrons toward the Al electrode, even if the excitons reach the heterojunction.

Excitons generated in the P3HT layer, within 10 nm along the Al electrode, may be dissociated at this metal-semiconductor junction, after which the electrons will be collected at the Al and the holes, after traveling across the P3HT region, at the anode and contribute to the diode current. This effect is described by diode D1. The different regions can be also formed by the overlap or near-by location of small sphere-like regions of the same material as observed in SEM cross sections shown in [1, 13] and represented in **Fig. 3.4b** where PCBM regions are the white spheres. The interface between the two phases can present an interpenetrated surface or not. In the first case the path of holes from the Al-P3HT contact to the top electrode will be larger producing larger series resistance.

In addition, pinholes and non-uniformities in the active layer may produce additional conduction between electrodes, giving rise to a shunt resistance, represented in the EC as R_{SH2}.

According to this representation, the active layer of blend 1 cells seems to contain less interpenetrated regions of PCBM that reaches both electrodes, or at least cover most of the active layer depth. Dissociation at the heterojunction is efficient, and the length of the corresponding material that charge carriers dissociated at the heterojunction have to travel to reach the electrodes is smaller and so R_S is smaller. At the same time, holes dissociated at the Al-P3HT contact will also have a shorter distance to travel to the upper contact. The distribution of regions with Schottky contact provides that the effect of charge separation at the Al electrode, although not predominant, can be detected.

For cells from blend 2, series resistance is almost one order higher and the effect of the Schottky diode is practically not observed. These results suggest that the morphology of the active layer for blend 2 contains a more interpenetrated distribution of P3HT and PCBM, providing more heterojunction surface, but longer path for carriers to reach the electrodes. The separation of carriers is also efficient, but the path to travel is longer, resulting in higher values of R_{S2}. In this case, although regions with Al-P3HT contact are present, the current due to the dissociation at the heterojunction is more important that the one due to the Schottky diode and its contribution is not observed in the I-V curve. After staying 3 days in ambient conditions, the increase in R_{S2} for blend 2 cells was around five times greater than for blend 1 cells, which is in agreement with having a more interpenetrated morphology. The increase in series resistance observed when the devices are left in ambient conditions has been attributed to several factors as reduction of mobility, metal corrosion at the contact or changes in the contact barrier and charge space regions [14, 15].

The effect of the reduction of series resistance observed under illumination was more important in the longer path device, around 20% and 40% for blend 1 and blend 2 cells respectively just after fabrication and around 10% and 50% respectively after degradation.

The shunt resistance behaves in a similar way. Right after fabrication, in dark conditions, its value is similar for blends 1 and 2 cells reducing only slightly when working under illumination. After degradation, in a similar way as the series resistance, its value increases. The increase was again more significant in blend 2 than in blend 1 cells and it was interesting to observe that when illuminated, $Rsh2_{il}$, returned to its value in dark before degradation, while series resistance only presented a maximum reduction of nearly 50 %.

The increase in both series and shunt resistance can be caused by the reduction in the mobile charge density and mobility probably associated to creation of traps due to the interaction of oxygen and water with the polymer. When left in ambient conditions without encapsulation, water and oxygen molecules can enter through the outer cell electrode, especially through pinholes or grains in the electrode and diffuse inside the polymeric material reacting with polymer molecules. [12] The interaction of O_2 and water with the polymers is well known as one of the causes of modification of their properties. [12] Illumination produces an increase in mobile charge density that compensates the previous charge density reduction during degradation. Experimental work must be done to confirm this hypothesis.

The increase of series resistance is responsible for the reduction of the short circuit current I_{SC} observed in all cells, as well as for the more significant reduction for blend 2 cells corresponding to longer charge paths, see curve (3) and (4) in **Fig. 3.3** and **Table 3.2.** The average efficiency of blend 1 and blend 2 cells reduced from around 2.0% and 2.7 %, respectively to around 0.14% and

1%. V_{OC} remained the same for blend 1 cells. For blend 2 cells, V_{OC} seems to have reduced more than 0.2 V, however, what really occurs is that the I-V under illumination is deformed, showing an inflection point, that has been interpreted as a counter diode appearing at the Al electrode due to corrosion or other type of degradation at the electrode [12] or due to the presence of slow charge transfer. [16] In general, although not much different in cell parameters, blend 1 cells show better stability.

In all cases, when cells remain sufficiently long in ambient conditions, series resistance continues increasing until the photovoltaic effect disappears.

3.4. Conclusions

Combining measured I-V characteristics with modeling under dark and illuminated conditions, it is possible to relate variations in device behavior with the morphology of the active layer, as well as possible causes of degradation. It was observed that relatively small variations in the active layer preparation procedure can produce significant variations in the cell series resistance. For cells from both blends, the ideality factor of I-V characteristics under dark and illuminated for V>0.5 V, was around 2 indicating that the dissociation process is associated to the bulk heterojunction. For blend 1 cells, the effect of the Schottky diode at the interface of P3HT with Al in addition to the heterojunction is observed, suggesting that Schottky diode regions contribute more to the current than in blend 2 cells. The lower series resistance observed in blend 1 cells is also consistent with less interpenetrated regions. The increase in both series and shunt resistance can be caused by the reduction in the mobile charge density and mobility associated to creation of traps produced by the

interaction of oxygen and water with the polymer. This effect is more significant for cells where charges have longer paths to travel toward the electrode.

3.5. References

[1] H. Hoppe, DAM Egbe, D. Mühlbacher, N.S. Sariciftci, Photovoltaic action of conjugated polymer/fullerene bulk heterojunction solar cells using novel PPE-PPV copolymers, *J. Mat Chem., 23* (2004) 3462–2467.

[2] D. Chirvase, J. Parisi, J.C. Hummelen, V. Dyakonov, Influence of nanomorphology on the photovoltaic action of polymer–fullerene composites, Nanotech., 15 (2004) 1317–1323.

[3] M. Al-Ibrahim, O. Ambacher, S. Sensfuss, G. Gobsch, Effects of solvent and annealing on the improved performance of solar cells based on poly3-hexylthiophene Fullerene, *Appl. Phys. Lett., 86* (2005) 201120.

[4] W. Ma, C. Yang, K. Lee, A.J. Heeger, Thermally Stable, Efficient Polymer Solar Cells with Nanoscale control of interpenetrating Network morphology, Adv. Funct. Mater., 15 (2005) 1517–1622.

[5] J. Pallares, R. Cabre, L.F. Marsal, R.E.I. Schropp, A compact equivalent circuit for the dark current-voltage characteristics of nonideal solar cells, *J. Appl. Phys., 100* (2006) 084513.

[6] P. Kumar, S.C. Jain, V. Kumar, S. Chand, R.P. Tandon, A model for the *J-V* characteristics of P3HT:PCBM solar cells, *J. Appl. Phys., 105* (2009) 104507.

[7] S.E. Shaheen, C.J. Brabec, N.S. Sariciftci, 2.5% efficient organic plastic solar cells, *Appl. Phys. Lett., 78* (2001) 841–843.

[8] A.C. Arias, J.D. MacKenzie, R. Stevenson, J.J.M. Halls, M. Inbasekaran, E.P. Woo, D. Richards, R.H. Friend, Photovoltaic

Performance and Morphology of Polyfluorene Blends: A Combined Microscopic and Photovoltaic Investigation, *Macromolecules, 34* (2001) 6005–6013.

[9] N. Camaioni, G. Ridolfi, G. Casalbore-Miceli, G. Possamai, M. Maggini, The Effect of a mild thermal treatment on the performance of Poly(3-alkythiophene)/Fullerene solar cells, *Adv. Mater., 14* (2002) 1735–1738.

[10] G. Dennler, M.C. Scharber, C.J. Brabec, Polymer-fullerene bulk-heterojunction solar cells, *Adv. Mater., 21* (2009) 1323–1338.

[11] L.M. Chen, Z. Hong, G. Li, Y. Yang, Recent Progress in Polymer Solar Cells: Manipulation of Polymer:Fullerene Morphology and the Formation of Efficient Inverted Polymer Solar Cells, *Adv. Mater., 21* (2009) 1434 – 1449.

[12] M. Jorgensen, K. Norrman, F.C. Krebs, Stability/degradation of polymer solar cells, *Sol. Energy Mater. Sol. Cells., 92* (2008) 686–714.

[13] H. Hoppe, N.S. Sariciftci, Morphology of polymer/fullerene bulk heterojunction solar cells, *J. Mater. Chem., 16* (2006) 45–61.

[14] M. Glatthaar, N. Mingirulli, B. Zimmermann, T. Ziegler, R. Kern, N. Niggemann, A. Hinsch, A. Gombert, Impedance spectroscopy on organic bulk-heterojunction solar cells, *Phys. Stat. Sol. A., 202* (2005) 125–127.

[15] M.J. Deen, M.H. Kazemeini, Photosensitive Polymer Thin-Film FETs Based on Poly (3-octylthiophene), *Proc. IEEE., 93* (2005) 1312–1320.

[16] M. Glatthaar, M. Riede, N. Keegan, K. Sylvester-Hvid, B. Zimmermann, M. Niggemann, A. Hinsch, A. Gombert, Efficiency limiting factors of organic bulk heterojunction solar cells identified by

electrical impedance spectroscopy, *Sol. Energy Mater. Sol. Cells.* 91 (2007) 390–393.

Chapter 4

Relation between inter-chain structure and the Jsc in P3HT:$PC_{70}BM$ solar cells

In this chapter, we have analyzed the relation between variations in the characteristics of the Poly (3-hexylthiophene-2,5-diyl) (P3HT) chains and the resultant solar cell short circuit current density. We show that the lattice constant between two lamellar structure of P3HT inside of the P3HT:Phenyl C_{70} Butyric Acid Methyl Ester ($PC_{70}BM$) blend reduced as the $PC_{70}BM$ percent in weight was reduced in the analyzed range. The presence of nanodomains, which can be related to the intensity of the peak, also affects the short circuit current density. In this study the optimum value of the percent in weight of $PC_{70}BM$, to obtain high short circuit current density was obtained for 1:0.5 ratio in the blend. The distance constant between the lamellar structures of P3HT for each blend made was directly extracted from the Bragg's law in combination with the μ-XRD analysis. The results were correlated with the electrical characterization

for each blend and we found that when decreases the distance between two lamellar structures of P3HT there is a better performance on photovoltaic devices.

4.1. Introduction

Most bulk heterojunction (BHJ) organic solar cells use as active layer, a blend of a conjugated polymer and a fullerene. Currently, this kind of organic solar cell is the most promising for the accomplishment of a low-cost, light-weight, large area, flexible, easily processed, and renewable energy source. [1] The main progress in bulk heterojunction organic solar cells has been achieved by introducing new materials with low band gap, process and new technologies. [2-5] Power conversion efficiencies (PCE) above 12 % were first reported in 2013. [6] The PCE of such devices is predominantly influenced by the optical and electronic properties of the donor and acceptor materials and the morphology of the blend controlling the domain size. [7-9]

Having domain sizes well defined in the bulk of the active layer helps to have a good performance on the charge carrier transport across of their respective materials (i.e. holes in donor material and electrons in acceptor material) and finally be collected in their respective metal contacts. Result of the foregoing is a reduction of the charge carrier recombination during the transport, situation that is desirable in the photovoltaic devices.

Although blends of poly (3-hexylthiophene-2,5-diyl) (P3HT):Phenyl C_{70} Butyric Acid Methyl Ester ($PC_{70}BM$) have been much studied, not enough attention has been paid to the study of P3HT inter-chains with the $PC_{70}BM$ and to the relation between the short circuit current density (J_{sc}) and the morphology, since the process of the charge generation and separation should

strongly depend on the interface properties, while the charge carrier transport will be determined by the bulk properties of the components of the active layer as was describe above.

In this chapter we will show that the quantity of fullerene in the blend modifies the interchain distance-spacing (d_{100}) in P3HT associated with the interdigitated alkyl chains, which affects the J_{sc}. The crystalline structures of the active layers were analyzed using micro-X-ray diffraction. This information in combination with the Braggs' law was used to calculate the distance-spacing in P3HT. The findings in distance-spacing in all blends together with complementary electrical characterization were subsequently correlated with the performance of the organic solar cells.

4.2. Materials and methods

This section is shown how was the preparation of different solutions that were used to manufacture the different photovoltaic devices. After, the solar cells are electrically characterized under dark and light. The conditions to do these studies are described below.

4.2.1. Device preparation

Indium tin oxide (ITO) coated glass substrates (with nominal sheet resistance of 15 ohm/square and the thickness of 120 nm) were purchased from PsiOTec Ltd. Poly-(ethylene dioxythiophene) doped with poly-(styrene sulphonic acid) (PEDOT:PSS) FHC was acquired from Ossila Ltd., P3HT (melting point 238 ºC, M_w ~17500 g mol^{-1}, 99.995 % region-regularity) and $PC_{70}BM$ (M_w ~1030.99 g mol^{-1}) were purchased from Sigma-Aldrich. High-

purity (99.99 %) silver (Ag) pellets were obtained from Testbourne Ltd., and calcium (Ca) pellets with high-purity (99.99 %) was purchased from Kurt J. Lesker.

Photovoltaic (PV) devices were fabricated on pre-cleaned patterned ITO glass substrates. A 30 nm PEDOT:PSS was applied onto the substrates by spin coating at 3500 rpm for 45 s. The PEDOT:PSS film was annealed at 110 ºC for 20 min. On top of the PEDOT:PSS the P3HT:$PC_{70}BM$ blend layer was deposited.

The P3HT:$PC_{70}BM$ blends at different ratios S1 (1:0.5), S2 (1:0.8), S3 (1:1.0) S4 (1:1.2) and S5 (1:1.5) corresponding at weight percent (wt%) of $PC_{70}BM$ at 33%, 45%, 50%, 54% and 60%, respectively. The weighing of semiconductor materials for each mixture was made strictly for any variations that may affect our study. All the blends solutions were prepared in o-dichlorobenzene:chlorobenzene (ODCB:CB) solution at a volume ratio of 6:4 (v/v) and left stirring over 17 h at 50 ºC. The active film was deposited by spin coating at 600 rpm for 45 s to obtain 80 nm of thickness. The cathode layer was deposited by thermal evaporation in an ultra-high vacuum chamber (1×10^{-6} mbar). Metals were evaporated through a shadow mask leading to devices with an active area of 0.09 cm^2. Ca (20 nm) and Ag (100 nm) were deposited at a rate of 0.15 Å s^{-1} and 0.5–0.8 Å s^{-1}, respectively. Each substrate contained four organic solar cells, which structure is shown in **Fig. 4.1**.

Final thermal annealing was done on a hot plate at 135 ºC for 20 min. All processing was done in a glove box under nitrogen atmosphere.

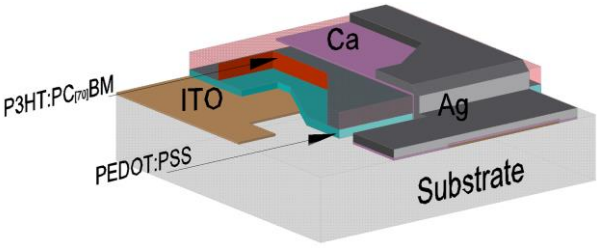

Fig. 4.1. Schematic structure of organic bulk heterojunction solar cell with the structure ITO/PEDOT:PSS/P3HT:$PC_{70}BM$/Ca/Ag.

4.2.2. Electrical and optical characterization

The crystalline structure of the active layer was analyzed using micro-X-ray diffraction (μ-XRD) measurements from a Bruker-AXS D8-Discover diffractometer equipped with a parallel incident beam (i.e. Göbel mirror), a vertical θ-θ goniometer, a XYZ motorized stage and with a general area diffraction system (GADDS). Samples were placed directly on the sample holder for reflection mode. An X-ray collimator system close to the sample allows to analyze areas of 500 μm. Diffraction patterns were recorded over an angular 2θ range of 3^o to 40^o. The data were collected with an angular step of 0.05^o at 10 s per step. The X-ray diffractometer was operated at 40 kV and 30 mA to generate $Cu_{k\alpha}$ radiation. The wavelength used was 0.154 nm.

The current density-voltage (J-V) characteristics of the devices were measured with a Keithley 2400 source measurement unit in combination with a solar simulator (Abet Technologies model 11000 class type A). The appropriate filters were utilized to faithfully simulate the AM 1.5G irradiation solar spectrum under standard specifications. [10] A light intensity of 100 mW/cm^2 equivalent at 1 sun illumination was used to test the organic solar cell devices. The light intensity of the solar simulator was calibrated with a silicon photodiode (NREL).

4.3. Results and discussion

In this section, we have demonstrated that the preparations of different blend solutions at different ratios have an important influence on the performance parameters of the devices and these are correlated with the interchains of the polymer in the blend. An optimum ratio of the polymer and fullerene to manufacture the blend layer is possible to get a high density current in the photovoltaic devices.

4.3.1. Electrical characterization by J-V under light

The J–V characteristics of the devices were measured in a sealed capsule under inert nitrogen atmosphere immediately after removing from the vacuum system. The short circuit current density, open circuit voltage (V_{oc}), fill factor (FF) and power conversion efficiency (PCE) of the fabricated devices are summarized in **Table 4.1**. The extracted parameters of each device under illumination were done using an electrical circuit to model the measured J-V characteristics. [11-13]

Fig. 4.2 shows the J-V curves under illumination of the devices prepared with blend compositions S1, S2, S3, S4 and S5 and measured at 300 K. Devices made with the S1 blend shows the best performance with a J_{sc} of 7.77 mA/cm^2, V_{oc} of 0.64 V, FF of 61% and PCE of 3.01%. These results agree with other reports made in a similar manner of fabrication having the power conversion efficiency with values around of 3%. [14, 15] The total of devices that were made with each blend solutions was sixteen.

No. of Blend	V_{oc} (V)	J_{sc} (mA/cm²)	FF (%)	PCE (%)	R_s (Ω)	R_{sh} (Ω)	I_o (pA)	n
S1	0.64	7.77	61	3.01	30	8.0×10^4	0.6	1.59
S2	0.63	7.00	48	2.13	40	1.8×10^5	0.8	1.61
S3	0.63	6.22	46	1.81	75	6.0×10^6	0.9	1.70
S4	0.62	4.43	43	1.17	100	2.5×10^6	0.5	1.71
S5	0.61	7.71	50	2.34	35	1.0×10^5	0.9	1.60

Table 4.1 Performance parameters and parameters extracted from the model used for all the blend films under standard light conditions (100 mW/cm^2) 1 sun at 300 K. J_{sc} is the short circuit current density, V_{oc} is the open circuit voltage, FF is the fill factor, PCE is the power conversion efficiency, I_o is the saturation current for the diode D, n the ideality factor, finally R_s and R_{sh} are the series and shunt resistance for the overall cell structure. [11-13]

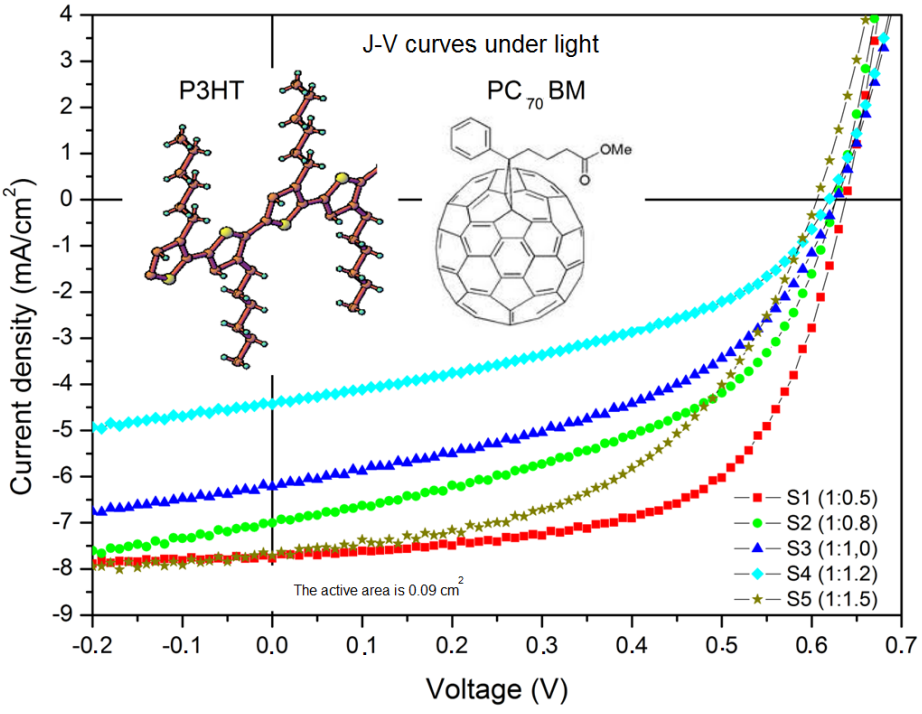

Fig. 4.2. J-V characteristics are shown for the different blend layers manufactured with P3HT:$PC_{70}BM$.

Cells using S2, S3, S4 and S5 blends presented an average J_{sc} of 9.90%, 19.9%, 43% and 0.77% less than that S1 blend. The effect of reduction of J_{sc} as the $PC_{70}BM$ in the blend was increased has been reported before [16, 17] and is attributed to the disorder induced in the structure when the amount of fullerene in the blend is increased. To confirm this assumption we show the μ-XRD for different blend solutions.

4.3.2. Analysis by μ-XRD in the different blend layers

Results from μ-XRD analysis are shown in **Fig. 4.3 a), b)** and **Table 4.2.** In **Table 4.2** it is seen the relation of J_{sc} with the strong first and second order reflections at 2θ angles for layer blends S1, S2, S3, S4 and S5.

For all the samples, the first peak in the diffractogram due to reflections of $2\theta_{(100)}$ angle is around 5 degrees. The peak in this region corresponds to the plane (100) and the value of $2\theta_{(100)}$ angle is related to the alkyl interchain distance-spacing (d_{100}) in P3HT, also known as the lattice constant. [18] The intensity of the peak is related to the presence of nanodomains. [19]

The peak intensity was the highest for S1, followed by S5. However, the values of the peak intensities of S2, S3 and S4 were 15.2%, 35.7% and 44.3% less than that S1 layer. The alkyl interchain distance-spacing d_{100} in P3HT was calculated using Bragg's law [19]:

$$2\, d \sin\theta = n\lambda, \qquad (1)$$

where 2θ is the angle between the incident and scattered X-rays wave vectors, λ is the wavelength incident beam (λ = 0.154 nm) and n is the interference order.

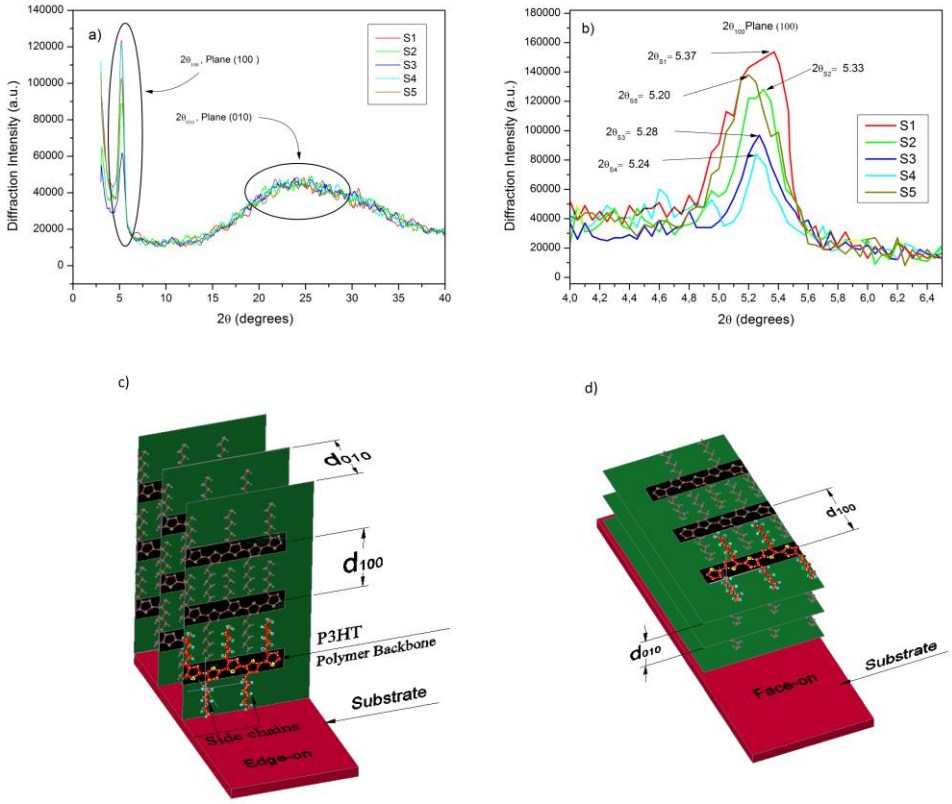

Fig. 4.3. Diffractogram of μ-XRD of P3HT:$PC_{70}BM$ for film blends S1, S2, S3, S4 and S5: a) Range values of 2θ from 3° to 40°. b) Zoom of the first order reflections angle in the plane (100), corresponding to the interchain distance spacing in P3HT represented as is shown in c) the edge-on. d) Represent the other form of in face-on orientation for P3HT for the plane (010).

Using the Eq. 1, it is calculated the distance-spacing d_{100} in P3HT for S1, S2, S3, S4 and S5 and are shown the values in **Fig. 4.4**. For this reason, the interdigitated alkyl chains distance in S1 blend are packed closer in the lamellar structure with edge-on see **Fig. 4.3 c)** and are reported in ref. [19-22]. This more

packed chains perpendicular to the substrates will improve transport of charge carriers, increasing J_{sc}.

No. of Blend	wt (%)	J_{sc} (mA/cm²)	$2\theta_{(100)}$ (degrees)	Diffraction Intensity $_{(100)}$ (a.u.)	$2\theta_{(010)}$ (degrees)	Diffraction Intensity $_{(010)}$ (a.u.)
S1	1:0.5	7.77	5.37	151000	24.51	53496
S2	1:0.8	7.00	5.33	128000	24.85	52871
S3	1:1.0	6.22	5.28	97000	24.60	51111
S4	1:1.2	4.43	5.24	84000	24.45	50000
S5	1:1.5	7.71	5.20	138000	23.74	55979

Table 4.2 Values obtained from μ-X-ray diffractions diffractograms of the different P3HT:$PC_{70}BM$ blends S1, S2, S3, S4 and S5. $2\theta_{(100)}$ and $2\theta_{(010)}$ are the angle between the incident and scattered X-ray wave vectors for the first and second order reflections, respectively.

The presence of more nanodomains correctly oriented between the electrodes will also enhanced carrier transport. According to results in **Fig. 4.4**, the increase of wt% of $PC_{70}BM$ in the blend increases the separation between main chains. However, the peak intensity related to the presence of nanodomains first reduces with the increase of wt% but starts to increase again for sample S5. Since the values of J_{sc} for S1 and S5 are similar, it confirms that, as expected, both the presence of the nanodomains and the interchain distance affect the transport properties.

The second peak localized at $2\theta_{(010)}$ angle around 24 degrees, corresponds to the plane at (010) and is related to the face-to-face packing ring d_{010} of P3HT in the blend, see its representation in **Fig. 4.3 d)** and are reported in ref. [19, 23]. The smaller the separation the better transport properties, which in this case will correspond again to S1.

The less interchain spacing d_{100} and d_{010} in both planes (100) and (010) for P3HT was observed for the blend P3HT:$PC_{70}BM$ with a ratio of 1:0.5 wt % as shown in **Fig. 4.4**.

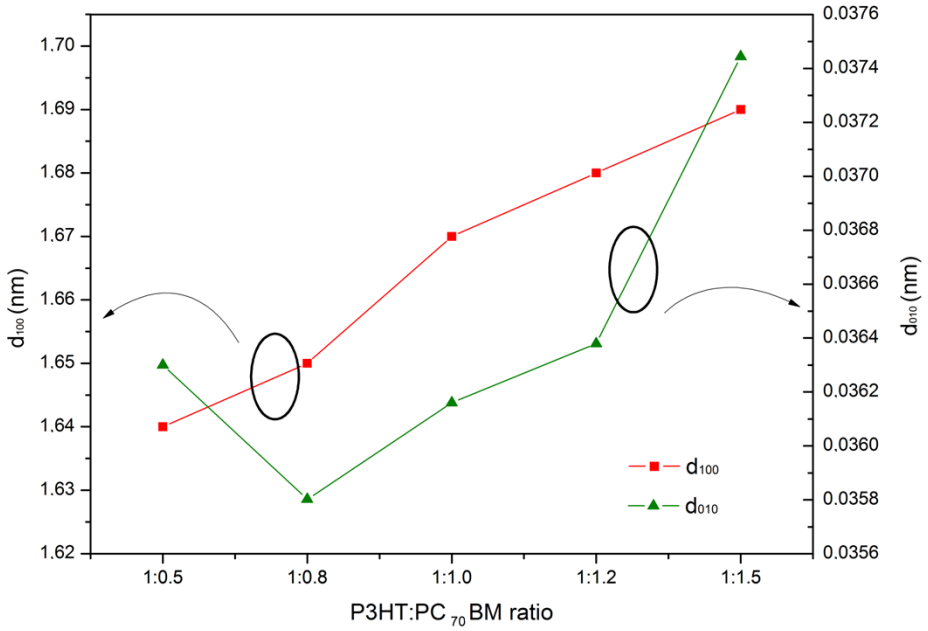

Fig. 4.4. The graph shows the distance-spacing of distribution for d_{100} and d_{010} that there between two lamellar structure of P3HT inside of the blend layer P3HT:$PC_{70}BM$ in the plane (100) and (010) with a ratio at 1:0.5, 1:0.8, 1:1.0, 1:1.2 and 1:1.5 wt %.

As the continuum percolation paths in the layer of the blend are reduced, the charge mobility reduces and less charge carriers are collected at the contacts, which turns into a reduction of the J_{sc} of the device. In this same experiment, it is seen that as the wt% of $PC_{70}BM$ increase, V_{oc} reduces, which a behavior is reported before. [14] The excess of the $PC_{70}BM$ can alter the distribution of regions corresponding to the constituent of the blend, affecting the transport of charge carrier between the electrodes and increase the charge carrier recombination in the photovoltaic device. [9]

4.4. Conclusions

In this chapter, we have presented that the lattice constant between two lamellar structures of P3HT inside of the blend P3HT:$PC_{70}BM$ of bulk heterojunction composites is affected by the $PC_{70}BM$ amount in the blend. Increasing the amount of $PC_{70}BM$ increases the disorder of the interchains of the polymer in the blend and there is an increase in the charge carrier recombination. The micro-X-ray diffraction showed that the less interchain distance-spacing d_{100} in P3HT of 1.64 nm, corresponded to the blend S1 (1:0.5 wt%), which showed highest $J_{sc,}$ since this condition helps to have a better charge carrier transport through the active layer. The μ-XRD analysis also confirms the presence of nanodomains in the polymer active layer. The information of μ-XRD analysis was correlated with the values of the electrical characterization in order to understand how the parameters of the organic solar cells are affected.

4.5. References

[1] C.J. Brabec, Organic photovoltaics: Technology and market, Sol. Energy Mater. Sol. Cells, 83 (2004) 273–292.

[2] W. Cai, X. Gong, Y. Cao, Polymers solar cells: recent development and possible routes for improvement in the performance, *Sol. Energy Mater. Sol. Cells, 9* (2010) 114–127.

[3] M. Helgesen, R. Sondergaard, F.C. Krebs, Advance materials and processes for polymer solar cell devices, *J. Mater. Chem., 20* (2010) 36–60.

[4] G. You, J.C. Hummelen, F. Wudl, A. Heeger, Polymer photovoltaic cells: enhanced efficiencies via a network of internal donor–acceptor heterojunctions, *Science 270* (1995) 1789–1791.

[5] Y. Zhang, Z. Li, S. Wakim, S. Alem, S. Tsang, J. Lu, J. Ding, Y. Tao, Bulk Heterojunction solar cells based on a new low-band gap polymer: morphology and performance, *Org. Electron., 12* (2011) 1211–1215.

[6] M. Green, K. Emery, Y. Hishikawa, W. Warta, E.D. Dunlop, Solar Cell Efficiency Table (Version 39), *Res. Appl., 20* (2012) 12–20.

[7] J. Peet, A.J. Heeger, G.C. Bazan, Plastic solar cells: Self-assembly of bulk heterojunction nanomaterials by spontaneous phase separation, *Acc. Chem. Res., 42* (2009) 1700–1708.

[8] M.C. Scharber, D. Muhlbacher, M. Koppe, P. Denk, C. Waldauf, A. Heeger, C.J. Brabec, Design rules for donors in bulk heterojunction solar cells: Towards 10% energy conversion efficiency, *Adv. Mater., 18* (2006) 789–794.

[9] V.S. Balderrama, M. Estrada, A. Cerdeira, B.S. Soto-Cruz, L.F. Marsal, J. Pallares, J.C. Nolasco, B. Iñiguez, E. Palomares, J. Albero, Influence of P3HT:PCBM blend preparation on the active layer morphology and cell degradation, *Microelectron. Reliab., 51* (2011) 597–601.

[10] S.E. Shaheen, C.J. Brabec, N.S. Sariciftci, F. Pandinger, T. Fromherz, 2.5 % efficient organic plastic solar cells, *J. Appl. Phys., 78* (2001) 841–843.

[11] J.C. Nolasco, A. Sanchez-Diaz, R. Cabré, J. Ferré-Borrull, L.F. Marsal, Relation between the barrier interface and the built-in potential in pentacene/C60 solar cell, *Appl. Phys. Lett., 97* (2010) 013305.

[12] J. Pallarés, R. Cabré, L.F. Marsal, R. Schropp, A compact equivalent circuit for the dark current-voltage characteristics of nonideal solar cells, *J. Appl. Phys., 100* (2006) 084513.

[13] J.C. Nolasco, R. Cabré, J. Ferré-Borrull, L.F. Marsal, M. Estrada, J. Pallarés, Extraction of poly (3-hexylthiophene) (P3HT) properties from dark current voltage characteristics in a P3HT/n-crystalline-silicon solar cell, *J. Appl. Phys., 107* (2010) 044505.

[14] S.S. Bavel, M. Barenklau, G. With, H. Hoppe, J. Loos, P3HT/PCBM bulk heterojunction solar cells: impact of blend composition and 3D morphology on device performance, *Adv. Funct. Mater., 20* (2010) 1458–1463.

[15] J.A. Renz, T. Keller, M. Schneider, S. Shokhovets, K.D. Jandt, J. Gobsch, H. Hoppe, Multiparametric optimization of polymer solar cells: a rout to reproducible high efficiency, *Sol. Energy Mater. Sol. Cells 93* (2009) 508–513.

[16] W. Ma, C. Yang, X. Gong, K. Lee, J. Heeger, Thermally stable, efficient polymer solar cells with nanoscale control of the interpenetrating network morphology, *Adv. Funct. Mater., 15* (2005) 1617–1622.

[17] D. Chirvase, J. Parisi, J.C. Hummelen, V. Dyakonov, Influence of nano-morphology on the photovoltaic action of polymer-fullerene composites, *Nanotechnology 15* (2004) 1317–1323.

[18] G. Li, Y. Yao, H. Yang, V. Shrotriya, G. Yang, Y. Yang, Solvent annealing effect in polymer solar cells based on poly(3hexylthiophene) and methanofullerenes, *Adv. Funct. Mater., 17* (2007) 1636–1644.

[19] T. Erb, U. Zhokhavets, G. Gobsch, S. Raleva, B. Stühn, P. Schilinsky, C. Waldauf, C.J. Brabec, Correlation between structural and optical properties of composite polymer/fullerene films for organic solar cells, *Adv. Funct. Mater., 15* (2005) 1193–1196.

[20] H. Sirringhaus, P.J. Brawn, R.H. Friend, M. Nielsen, K. Bechgard, B.M.W. Langeveld-Voss, A.J.H. Spiering, R.A.J. Jansen, E. W. Meijier, P. Herwig, D.M. de Leeuw, Two-dimensional charge transport in self-organized, high-mobility conjugated polymers, *Nature 401* (1999) 685–688.

[21] Y. Kim, S. Cook, S. Tuladhar, S.A. Choulis, J. Nelson, J.R. Durrant, D.C.C. Bradley, M. Giles, I. McCulloch, C-S. Ha, M. Ree, A strong regioregularity effect in self-organizing conjugated polymer films and high-efficiency polythiophene:fullerene solar cells, *Nat. Mater., 5* (2006) 197–203.

[22] H. Yang, S. LeFevre, C.Y. Ryu, Solubility-driven thin film structures of regioregular poly(3-hexilthiophene)using volatile solvents, *Appl. Phys. Lett., 90* (2007) 172116.

[23] T. Chen, X. Wu, R.D. Rieke, Regio controlled synthesis of poly(3-alkylthiophenes) mediated by rieke zinc: Their characterization and solid-state properties, *J. Am. Chem. Soc., 117* (1995) 233–244.

Chapter 5

Analysis of degradation mechanisms in PTB1:PCBM solar cells under different environments

The degradation on the organic solar cells is one of many issues that are not yet understood so that it is necessary to do some investigations. In this chapter we investigate the degradation of bulk heterojunction solar cells based on the polymer poly [[4,8-bis (octyloxy) benzo (1,2-b:4,5-b') dithiophene-2,6-diyl) (2-((dodecyloxy) carbonyl) thieno(3,4-b) thiophenediyl]] (PTB1) and the fullerene [6,6]-phenyl C_{61}-butyric acid methyl ester (PCBM) under different environments: dry nitrogen atmosphere (H_2O < 0.1 ppm, O_2 < 0.1 ppm), air (60 ± 5% relative humidity) and under encapsulation in accordance with established ISOS-D1 protocols. The evolution of the electrical measurements under dark and illumination conditions is used to analyze the degradation process during

5300 h and its relationship with the physical mechanisms. The degradation in the efficiency of the solar cells is mainly due to a reduction of short circuit current density (J_{SC}) and fill factor (FF) while open circuit voltage (V_{OC}) is the most stable parameter in all studied conditions. The T_{S80} lifetimes for power conversion efficiency (PCE) of samples exposed to nitrogen and air environments and under encapsulation were 990 h, 4 h and 48 h, respectively. The analysis of the PCE decay permits to identify and evaluate the intensity of different degradation mechanisms (intrinsic polymer chemical reactions or by diffused environmental oxygen or water) in the different conditions.

5.1. Introduction

During the last years, it can be seen a rapid and significant advance in the field of organic solar cells, where devices with efficiencies of 12% have already been reported. [1] The use of polymeric organic semiconductor materials mixed with fullerene to fabricate bulk heterojunction (BHJ) cells has been one of the most important discoveries to improve the characteristics of organic photovoltaic devices. [2] Among advantages of these organic semiconducting materials with respect to inorganic materials are of low-cost, light-weight, possibility to deposit on large areas and on flexible substrates, as well as simpler processing techniques allowing the fabrication of devices for different applications, which sometimes are not possible to obtain for inorganic materials. [3, 4] Inside solar energy harvesting, in order to make an effective use of the photovoltaic effect in organic materials, it is necessary to develop appropriate architectures, semiconducting materials that reach or cover up as much as possible the solar spectrum, as well as good control of the molecular ordering inside the active layers. [5] In spite of the important advances obtained

at present, the reliability of the cells is still low and their lifetime short and not many studies are devoted to understanding the degradation processes and to solve them. [6]

The main progress in bulk heterojunction organic solar cells (BHJ-OSC) has been achieved by introducing new materials with low-band gap, new processes and new technologies. [7-10] The efficiency in polymer-blend BHJ devices has been steadily improved, but their practical application is limited by the relatively short lifetime of the devices. During the last years, much effort is being made to understand the causes of the degradation process in organic photovoltaic devices [11-13] and how to overcome them. However, it is a complex problem that depends on many factors, such as the device structure, the active material layer and the device fabrication process, among others. [14-18]

The poly [[4,8-bis (octyloxy) benzo (1,2-b:4,5-b') dithiophene-2,6-diyl) (2-((dodecyloxy) carbonyl) thieno(3,4-b) thiophenediyl]] (PTB1) has been used as a promising donor in junction-type solar cells, due to its low-band gap, relatively high molecular weight, solubility in halogenated solvents, high carrier mobility, long exciton diffusion length and strong absorption in the visible region. [19-21] The energy levels of the highest occupied molecular orbital (HOMO) and the lowest unoccupied molecular orbital (LUMO) are reported to be -4.90 eV and -3.20 eV, respectively. [19, 22] A power conversion efficiency of 4.76% has been reported for devices fabricated from blends of PTB1 with [6,6]-phenyl C_{61}-butyric acid methyl ester (PCBM) [21], however, an analysis of the degradation behavior for this type of BHJ-OSC when the devices are operated in air, nitrogen and under encapsulation has not yet been reported.

Most studies regarding the lifetime and degradation of OSC have focused on P3HT polymer and the main factor responsible for the degradation is related to the permeation of oxygen and water molecules into the active layer or

the metal electrode. [8, 10, 12, 17] Oxygen and water can react with the polymeric or organic materials, as well as with the metal at the contact electrode, changing their properties. Other cases of degradation observed are associated with the illumination when the oxidation of the active layer is accelerated in combination with the presence of molecular oxygen and water. [23, 24]

In this chapter, we present a long-term stability study of BHJ-OSC based on low-band gap PTB1 polymer done under ISOS-D1 protocols. [25] Several samples were analyzed under different environments such as in dry nitrogen, air and under encapsulated (adhesive applied) with UV curing. The observed degradation of the OSC electrical parameters over a time interval up to 5300 h are studied and related to the physical mechanisms taking place in the device. The study is done by modelling the evolution of power conversion efficiency parameter as the sum of two different exponential decays and obtaining characteristic decay times that are then related to the possible predominant degradation mechanisms.

5.2. Materials and methods

This section describes the preparation and the exposition under different environments the solar cells. Protocols ISOS-D1 was applied on all the devices under analysis. The solar cells were electrically characterized under light and dark conditions. The parameters and conditions to do these studies are described below.

5.2.1. Device preparation and characterization

Indium tin oxide (ITO) coated glass substrates of 15 Ω/square and 120 nm of thickness were purchased from PsiOTec Ltd. PEDOT:PSS FHC was acquired from Ossila Ltd.; PTB1 (M_w ~22900 g mol^{-1}) and PCBM (M_w ~910.88 g mol^{-1}) were purchased from One-material and Sigma-Aldrich, respectively. High-purity (99.99%) Ag wire was obtained from Testbourne Ltd., and Ca pellets with high-purity (99.99%) were purchased from Kurt J. Lesker.

Photovoltaic (PV) devices were fabricated on pre-cleaned, patterned ITO glass substrates. 30 nm of PEDOT:PSS was deposited on the substrates by spin coating at 3500 rpm for 45 s and annealed at 110 ºC during 20 min. The PTB1:PCBM active blend with a weight ratio of 1:1 was dissolved in 15 mg/ml of o-dichlorobenzene (ODCB) solution and left stirring around 24 h at 40 ºC. The active film was deposited on top of the PEDOT:PSS layer by spin coating at 1000 rpm for 30 s, obtaining 100 nm of thickness. Afterwards, the cathode layer, consisting of 25 nm of Ca and 100 nm of Ag, was deposited by thermal evaporation in an ultra-high vacuum chamber (9 x 10^{-7} mbar), at a rate of 0.04 nm/s and 0.05-0.08 nm/s respectively, on top of the active layer. **Appendix A** is depicted the process fabrication of the organic solar cell.

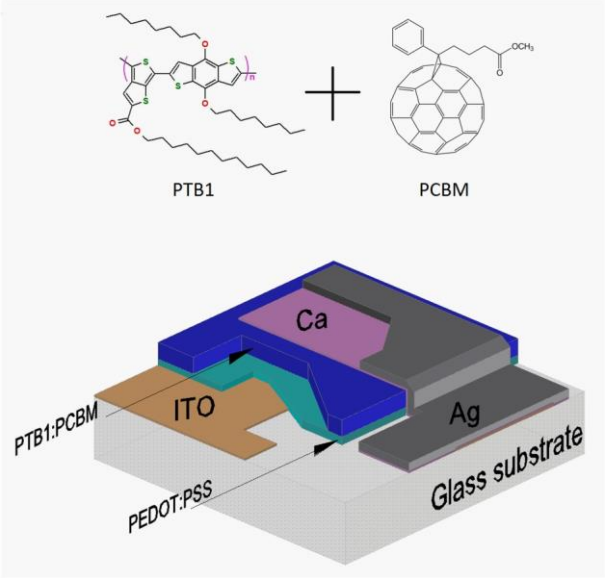

Fig. 5.1 Schematic structure of organic bulk heterojunction solar cell with the structure ITO/PEDOT:PSS/PTB1:PCBM/Ca/Ag. The inset shows molecular structures of the PTB1 and fullerene derivatives.

The active area of the devices was 0.09 cm^2 as defined by the geometric overlap between ITO and Ag. No further annealing was done on the solar cells after the evaporation of metallic contacts. **Fig. 5.1** shows the device structure used for this analysis. In the same figure, the molecular structure of PTB1 and PCBM is shown. All process steps were done in a glove box under nitrogen atmosphere. Several OSC were prepared on the same substrate to check the reproducibility of the electrical characteristics of devices fabricated at the same time and their further degradation behavior.

5.2.2. Degradation testing conditions and protocols

The stability testing used in this analysis was in accordance with ISOS-D1 protocols. [25] Three groups of devices were prepared to study the

degradation process of their electrical characteristics under 3 different environments: a) in electronic grade 99.999% N_2 (H_2O < 0.1 ppm, O_2 < 0.1 ppm), b) in ambient conditions (60 ± 5% RH) and c) encapsulated. The photovoltaic cell characteristics, namely the open circuit voltage (V_{OC}), short circuit current density (J_{SC}), fill factor (FF) and power conversion efficiency (PCE) of the devices were measured with a Keithley 2400 source measurement unit in combination with a solar simulator (Abet Technologies model 11000 class type A, Xenon arc), automatically controlled with a computer. Appropriate filters were used to reproduce the AM 1.5G spectrum. A light intensity of 100 mW/cm^2 was used to test the organic solar cell devices under illumination. In addition J–V dark curves were collected for all the photovoltaic devices.

During the first 288 hours, all sample groups were stored in N_2 at 23 ^oC. In this time the devices were measured under light at 1sun and after the samples were stored under darkness. The photovoltaic solar cells in this period of time did not show any substantial change in their PCE. So, the group of devices was divided into three subgroups. The first group named S1 remained in a dry N_2 environment, in the dark and at 23 ^oC for the rest of the experiment. The second group of devices, named S2, was transferred to ambient conditions, exposed in air and kept in an open chamber in the dark with storage temperature at 23 ^oC, while the third group of devices, named S3, was encapsulated using a top glass sealed to the bottom glass with the glue adhesive [3-(2,3-epoxypropoxy)propyl]-trimethoxysilane, hydroxypropyl methacrylate (EPT-HM)). The encapsulated cells were exposed to UV radiation (ELC-410 light curing system) for not more than 20 s to cure the glue. The process was done under nitrogen atmosphere. After encapsulation, the S3 group was transferred to ambient conditions and kept in an open chamber in the dark with storage temperature of 23 ^oC. The current density–voltage (J–V) curves under illumination and dark were measured for the three groups of cells.

5.2.3. ISOS-D1 protocols

Appendix B is depicted in general the ISOS-D1 protocols applied to the organic solar cell. The ISOS protocols require to report four pairs of values to accurately describe the pattern of the decay of a given solar cell performance metrics (Efficiency, or alternatively V_{OC}, J_{SC}, FF). The first measurement point, E_0 is the initial testing measurement immediately after the device fabrication, and its corresponding time T_0 is considered as the origin. A second measurement pair (E_S, T_S) corresponds to an efficiency value and a time after a first stabilization of the device, before subjecting it to further ageing conditions. This time can be arbitrarily defined in order to describe accurately this stabilization process. The third and fourth pairs of parameters, (E_{80}, T_{80}) and (E_{S80}, T_{S80}) represent the performance of the device after it has decayed 20% from its initial or second testing measurement, respectively. [25, 26, 27] Furthermore, lifetimes of photovoltaic cells at T_{S50}, T_{S30} and T_{S10} were obtained, analyzed and compared between them and with the different groups of devices (S1, S2 and S3). Four devices of each group were taken to follow the degradation.

The optical microscope ZEISS AXIO Imager was used to obtain images from the surfaces of the metallic contact of the devices to correlate to them with the process of degradation exposed in the different environments.

5.3. Results and discussion

The analyses of the degradation over time in the solar cells exposed under different environments were analyzed by J-V curves. The predominant degradation mechanisms were correlated with the performance parameters of the cells. The PCE decay obtained over time was modelled by the superposition of two exponential functions. The parameters extracted from the exponential function were interpreted as the degradation ratio that experiment each group of devices exposed under different environments.

5.3.1. J-V characterization of devices under N_2 environment

Table 5.1 shows the average parameters of the organic solar cells just after fabrication. The variation from sample to sample is due to small variations in the thickness or quality of the Ca/Ag top electrodes and/or modifications in film morphology. The champion OSC of our process presented a PCE of 5.2%. For this study, we analyzed cells with efficiency of 4.4±0.2%. During 288 h, the degradation process was nominally identical for all devices presenting similar qualitative behavior. The V_{OC}, J_{SC}, FF and PCE fell 2.9%, 19%, 1.9% and 22%, respectively regarding cells just after fabrication. This time was chosen as the second measurement time, T_S = 288 h. The analysis of degradation began after the three groups were formed, and exposed under different environments as was mentioned above. The study is presented in relative values with respect to this T_S and following the ISOS-D1 protocols.

Right after fabrication	V_{OC} [mV]	J_{SC} [mA/cm^2]	FF [%]	PCE [%]
Champion OSC	600	12.6	68.2	5.2
Average values (twenty-five devices)	577±8	11.4±0.7	67.1±3.7	4.4±0.2

Table 5.1 Champion and average performance parameters of PTB1:PCBM solar cells just after fabrication.

Fig. 5.2a shows typical degradation of J–V curves under illumination, for samples kept in N_2. The samples were only exposed to light during the J–V measurement (for less than 1 min per measurement) and afterwards were returned to glove box.

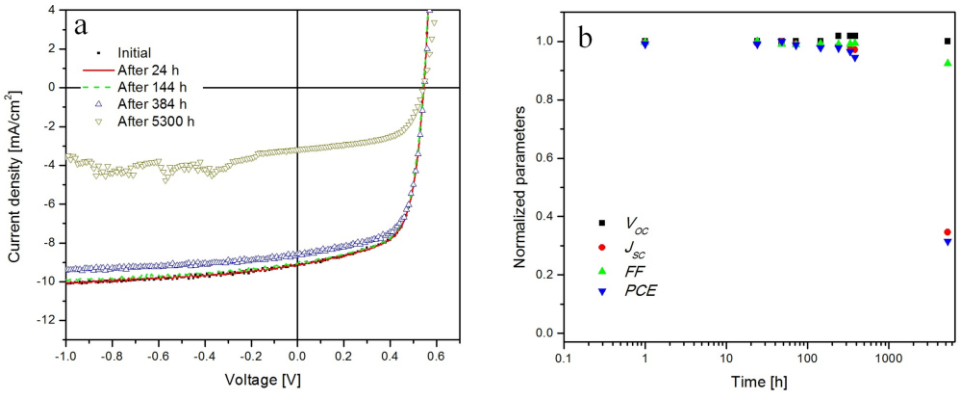

Fig. 5.2 (a) Illuminated J–V curves of PTB1:PCBM solar cells of S1 group for different degradation times under nitrogen environment during 5300 h. All of the devices were measured under AM 1.5G spectrum condition (100 mW/cm^2). (b) Normalized performance parameters of devices regarding to their initial values as a function of time. V_{OC} is open circuit voltage, J_{SC} is the short circuit current density, FF is fill factor and PCE is power conversion efficiency.

The normalized behaviors with the new initial time of cell average parameters are presented in **Fig. 5.2b.** Following the ISOS-D1 protocol, the

lifetimes of the studied devices are summarized in **Table 5.2**. The table displays the values of E_S (the initial PCE after the stabilization phase) and the times T_{S80}, T_{S50}, T_{S30} and T_{S10}, as defined in the protocols [25] for all the studied devices. The reported *PCE* value corresponds to the median of the measured values, while the T_S are taken from the most stable device. The lifetimes reached up for the S1 group of devices under nitrogen environment at T_{S80}, T_{S50}, and T_{S10} are presented in **Table 5.2**. The performance parameters such as V_{OC}, J_{SC}, FF and PCE decreased slowly until T_{S96} reached in less than 80 hours and falling down at 0%, 0.5%, 1.5% and 4.3% respectively. The performance loss of solar cells in this time period is negligible. After, PCE presented an exponential decay until T_{S30} in 5300 h. A T_{S30} the V_{OC}, J_{SC}, FF and PCE fell 1.0%, 65.2%, 7.7% and 69.4% respectively. The variation of PCE with time is mainly due to the variation of J_{SC}.

Standard Lifetime	N_2
T_{100} [PCE, %]	3.23
T_{S80} [h]	990*
T_{S50} [h]	2980*
T_{S30} [h]	5300
T_{S10} [h]	>5300

Table 5.2 Summary lifetime data for device under N_2 environment conditions given in hours.

The decay on the PCE is modeled by the superposition of two exponential functions with different time constants, as was previously done in ref. [28, 29].

$$PCE(t) / PCE(0) = A1\, e^{(-t / T1)} + A2\, e^{(-t / T2)} \qquad (1)$$

where *PCE(0)* is the relative initial power conversion efficiency (t = 0 h). The time constants of degradation (*T1*, *T2*) and the weighing (*A1*, *A2*) as the

degradation power factor of the individual exponential functions are obtained via a least-square fit.

For the cells left in N_2, **Fig. 5.3** shows measured and modeled curve using Eq. (1). The value of *T1* and *T2* was 4800 h for both of them, while A1 = A2 = 0.5. The high degradation time constant and slow degradation can be attributed to that main degradation mechanism by chemical reaction between the polymeric and metallic materials and not being important by the effect of very low content of both water and oxygen in the N_2 gas, (< 0.1 ppm). These results are in good agreement with previous works that report long lifetimes of devices fabricated with other materials exposed only under nitrogen environment. [30, 31] These works indicate that the dominant process is the degradation of the electrode-organic material interface due to water and oxygen diffusion. Furthermore, the polymer can be doped by the diffusion of calcium ions from the electrode, causing additional polymer degradation.

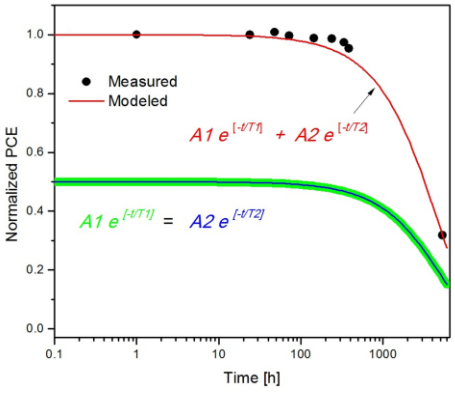

Fig. 5.3 Fit of the PCE normalized versus time using Eq. (1) for the S1 group of solar cells. The filled symbols are the experimental data and the line is the fitting curve.

Fig. 5.4a shows J–V curves under dark for S1 devices initial and degraded as a function of exposure time in nitrogen environment. It is well known that, at high voltage / high forward bias current, J is dominated by the

overall series resistance (R_S) that includes the bulk and the contact resistance of the device. This resistance R_S is related to the transport properties of the semiconductor material and to the properties of the contacts [32] and its value per unit area, R_{S0}, can be calculated by the inversed slope of the J–V curve at the highest operating voltage range where the curve becomes linear: $R_{S0} = (J/V)^{-1}$.

At low voltage / low current, near J_{SC}, J is dominated by the shunt resistance, R_{SH}, which is related to the recombination of charge carriers near the dissociation site (e.g. Donor/Acceptor interface of both organic materials PTB1:PCBM in this case), that is, it also depends on the transport properties of the semiconductor. The value of shunt resistance per unit area, R_{SH0}, can be calculated by calculating the inverse slope around 0 V of the J–V curve, $R_{SH0} = (J/V)^{-1}$.

R_{S0} and R_{SH0} for S1 devices, extracted from dark J–V curves, are shown in **Fig. 5.4b**. It is observed that, R_{S0} in S1 photovoltaic devices, increases from 1.35 Ω-cm^2 reaching 3.66 Ω-cm^2 after 5300 h. R_{SH0} started from a value of 1.46 x 10^6 Ω-cm^2, and after falling until reach 8.16 x 10^2 Ω-cm^2 at 5300 h.

The small increase of R_{S0} can be attributed to several factors such as the degradation of the active layer of the solar cells due to small reaction with water or oxygen, the electro-chemical reaction within the PEDOT:PSS layer or at its interface with the active and ITO layers, the reaction of calcium with silver electrode. Some of these possibilities were analyzed in detail as in [28].

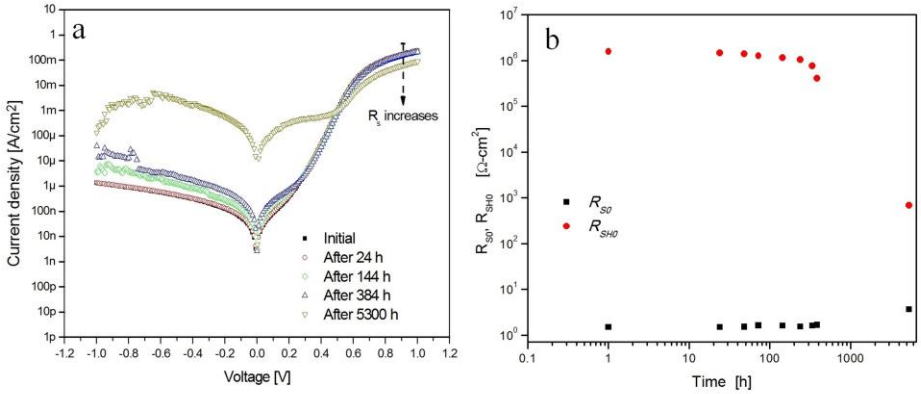

Fig. 5.4 (a) Dark J–V curves for S1 group of devices under nitrogen environment and its degradation process through time by 5300 h. (b) Variation of shunt resistance per unit area, R_{SH0} and series resistance per unit area, R_{S0} over time.

5.3.2. J-V characterization of devices under air environment

Fig. 5.5a shows illuminated J–V curves as a function of time of devices named S2, left in ambient conditions, while **Fig. 5.5b** shows the variation with time in ambient conditions of the performance parameters. Parameters were normalized to their initial values before exposure to air. In this case, a rapid degradation was observed similarly as in [33]. The lifetimes reached up by S2 group of devices under air environment are shown in **Table 5.3**. The performance parameters such as V_{OC}, J_{SC}, FF and PCE decreased rapidly in T_{S10} by 80 hours being of 5.3%, 83.8%, 30.9% and 90.1% respectively. Finally with T_{S1} for 384 h under air the V_{OC}, J_{SC}, FF and PCE fell 60.3%, 99.7%, 94.1% and 99.9%, respectively.

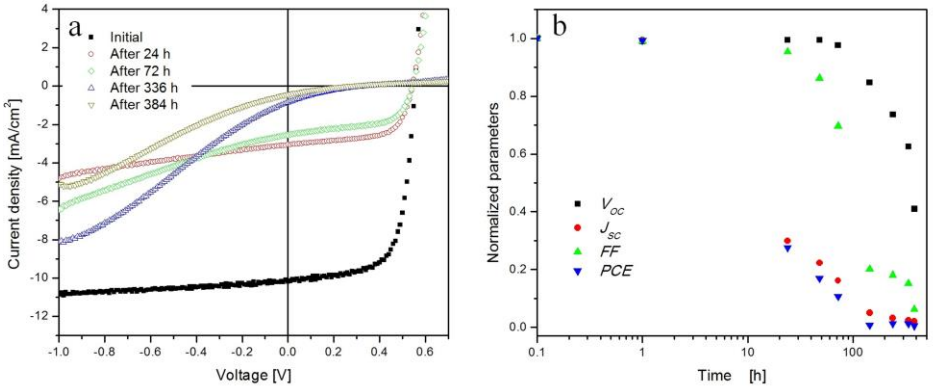

Fig. 5.5 (a) Illuminated J–V curves of PTB1:PCBM solar cells of S2 group for different degradation times under air environment during 384 h. All of the devices were measured under AM 1.5G spectrum condition (100 mW/cm^2). (b) Normalized performance parameters of devices regarding to their initial values as a function of time. V_{OC} is open circuit voltage, J_{SC} is the short circuit current density, FF is fill factor and PCE is power conversion efficiency.

Applying Eq. (1) to PCE, the experimental curve was modeled with T1 and T2 equal to 10 h and 80 h respectively, while A1 = 0.76 and A2 = 0.30, as it is shown in **Fig. 5.6** . We can suggest that the degradation mechanism present in the devices for the first and second time constant of degradation T1 and T2 is due to by water and oxygen, respectively as was observed similarly in [28].

Standard Lifetime	Air
T_{100} [PCE, %]	3.85
T_{S80} [h]	4*
T_{S50} [h]	11*
T_{S30} [h]	24
T_{S10} [h]	80

Table 5.3 Summary lifetime data for device under air environment conditions given in hours.

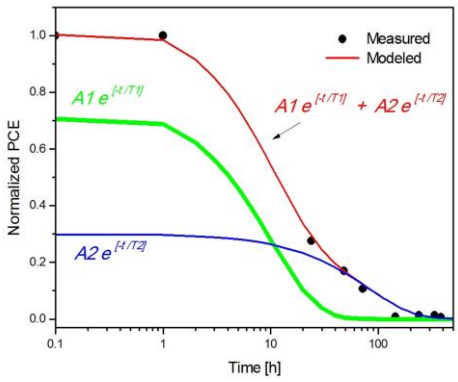

Fig. 5.6 Fit of the PCE normalized versus time using Eq. (1) for the S2 group of solar cells under air environment. The filled symbols are the experimental data and the line is the fitting curve.

For devices with normal geometric (no inverted), manufactured with PEDOT:PSS as hole transport layer and under air environment, the degradation process has been observed that the effect of water in the degradation process is significantly more important than the effect of molecular oxygen, [14, 31, 34], probably because the PEDOT:PSS accelerates the oxidation process due to its hygroscopic nature. The degradation we observed in air shows a similar behavior in the sense that, if water is present, its effect will be predominant. [29, 35]

Degradation of the J–V curves under dark for S2 devices is shown in **Fig. 5.7a** as a function of exposure time in air, from which the values of R_{S0} and R_{SH0} were extracted. **Fig. 5.7b** shows the variation with time of R_{S0} and R_{SH0}. R_{S0} had a rapid increase from 1.37 Ω-cm^2 to 1.38 *k*Ω-cm^2 regarding of its initial time to 384 h, respectively, probably caused by the reduction in the mobile charge density and mobility associated to creation of deep and shallow tramps due to the interaction of oxygen and water with the polymer, as was reported in [36] or due to the creation of an isolation layer between the blend active layer and the metallic contact, hindering the carrier charges to be collected. This is consistent with the strong reduction in FF observed in **Fig. 4b**. R_{SH0} started with a value of

1.27 x 10^6 Ω-cm^2 before exposure in air. Afterwards, it falls, reaching 6 x 10^3 Ω-cm^2 at 384 h.

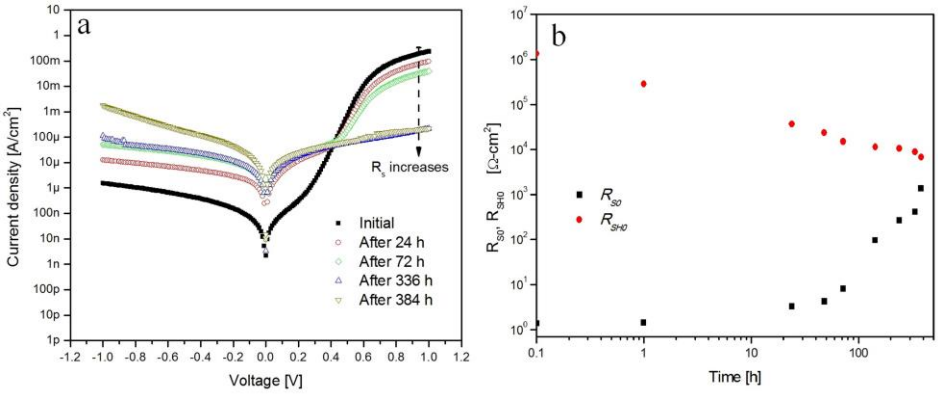

Fig. 5.7 (a) Dark J–V curves for S2 group of devices under air environment and its degradation process through time for 384 h. (b) Variation of shunt resistance per unit area, R_{SH0} and series resistance per unit area, R_{S0}, over time.

5.3.3. J-V characterization of devices under encapsulation

In order to create robust devices capable of sustained operation in ambient working conditions it is necessary a package. Among materials used to encapsulate are glass, polyethylene terephthalate (PET), polyethylene naphthalate (PEN). [13, 23, 26, 37, 38] We choose glass substrate as transparent and airtight barrier in combination with the UV thermosetting epoxy glue EPT-HM material to encapsulate the group of devices named S3. **Fig. 5.8a** shows illuminated J–V curves of S3 samples as a function of time, while **Fig. 5.8b** shows the evolution of performance parameters normalized to their relative initial values after encapsulation. The lifetimes reached up by the S3 group of devices under encapsulation at T_{S80}, T_{S50}, and T_{S10} are presented in **Table 5.4**. The V_{OC}, J_{SC}, FF and PCE start to reduce moderately in T_{S70} by 80 hours being of

0.1%, 24.9%, 0.8% and 29.1% respectively. Finally with T_{S15} by 5300 h under encapsulation the V_{OC}, J_{SC}, FF and PCE fell 3.4%, 76.1%, 34.8% and 85.1%, respectively.

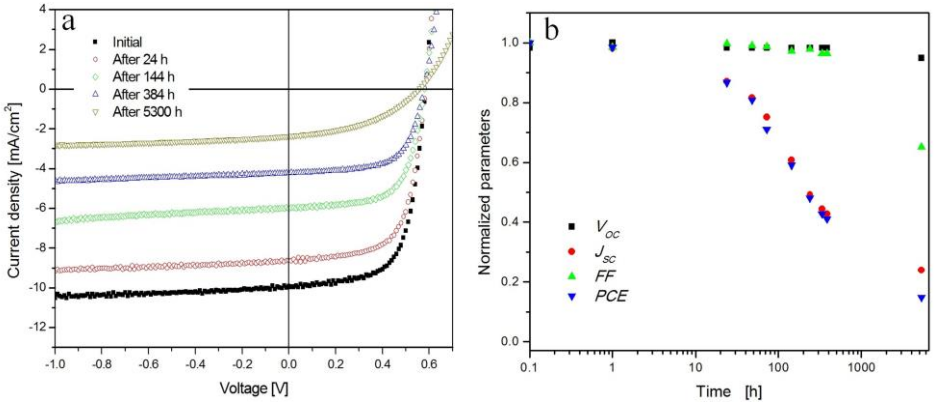

Fig. 5.8 (a) Illuminated J–V curves of PTB1:PCBM solar cells of S3 group for different degradation times under encapsulation during 5300 h. All of the devices were measured under AM 1.5G spectrum condition (100 mW/cm^2). (b) Normalized performance parameters of devices regarding to their initial values as a function of time. V_{OC} is open circuit voltage, J_{SC} is the short circuit current density, FF is fill factor and PCE is power conversion efficiency.

Standard Lifetime	Encapsulation
T_{100} [PCE, %]	3.82
T_{S80} [h]	48
T_{S50} [h]	240*
T_{S30} [h]	1880*
T_{S10} [h]	>5300

Table 5.4 Summary lifetime data for device under encapsulation environment conditions given in hours.

Applying Eq. (1) to PCE, the experimental curve was modeled with T1 and T2 equal to 4800 h and 80 h respectively, while A1 = 0.47 and A2 = 0.53, as it is shown in **Fig. 5.9**. We can observe that the PCE of the devices shows a time constant of degradation similar to the samples held in N_2 and air.

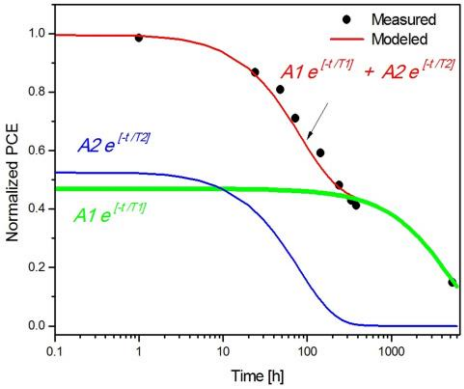

Fig. 5.9 Fit of the PCE normalized versus time using Eq. (1) for the S3 group of solar cells. The filled symbols are the experimental data and the line is the fitting curve.

We can suggest that the degradation mechanism present in the devices for the first and second T1 and T2 is due to chemical reaction of the materials and oxygen, respectively. After a certain amount of time, the oxygen present in the glue material can become active and reach the device, making the degradation process to occur faster being with more influence in this analysis. In the molecular structure of glue material used for encapsulation has oxygen as is shown in **Fig. 5.10**. The adhesive material to encapsulate the PTB1:PCBM solar cells was [3-(2,3-Epoxypropoxy)propyl]-trimethoxysilane, hydroxypropyl methacrylate (EPT-HM) in combination with UV curing. The EPT-HM was bought at Henkel Company. To support the above indicated, we made a micro-analysis of X-ray of this epoxy glue material that was used for the encapsulation of devices and the results are presented in **Appendix C**.

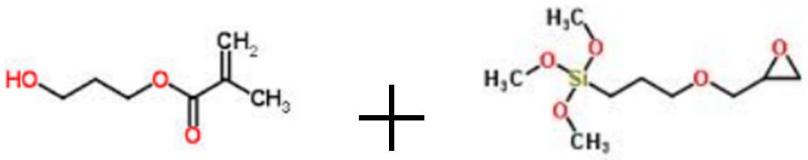

Fig. 5.10 Molecular structure is shown for EPT-HM material.

Despite being protected by the glue, it seems quite inevitable that after a sufficiently long time, water and other oxidizing agents present in the external ambient conditions, diffuse across the glue or enters though the edges of the seal, reaching the device and contributing also to its degradation, although this is expected to take longer times. Some reports affirm that the degradation of the adhesive used to seal the devices may induce the release of some by-products which can induce the decay of the cell. [37] At the end of its lifetime is possible that other oxidizing agents can also contribute to accelerate the process of degradation.

Fig. 5.11a shows dark J–V curves of initial and degraded S3 devices as a function of time under encapsulation. **Fig. 5.11b** shows the trend of R_{S0} and R_{SH0} for the same samples. R_{S0} shows a moderate increase from 1.76 Ω-cm^2 to 16.42 Ω-cm^2 in the interval from initial time to 5300 h, respectively. R_{SH0} started from a value of 1.9 x 10^6 Ω-cm^2 just before of being encapsulated, after it has a small fall reaching a value of 5.1 x 10^4 Ω-cm^2 at 144 h and again it has a little increase until 4.2 x 10^5 Ω-cm^2 at 5300 h.

Appendix D is depicted the possible degradation processes involved in the organic solar cell.

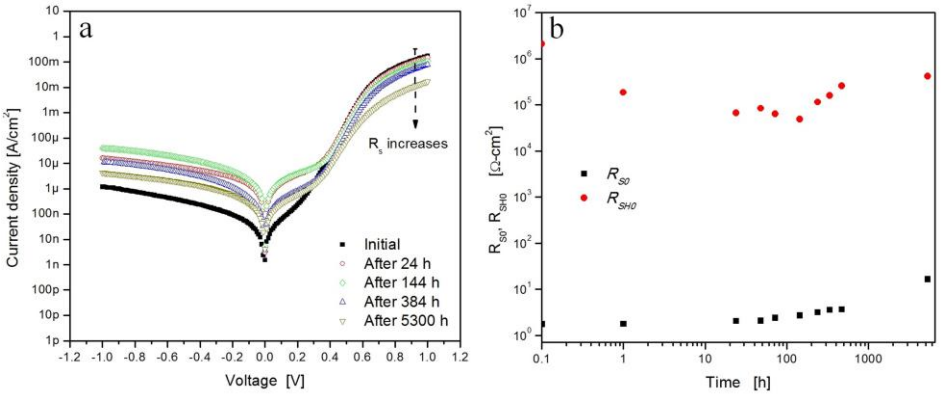

Fig. 5.11 (a) Dark J–V curves for S3 group of devices under encapsulation and its degradation process through time by 5300 h. (b) Variation of shunt resistance per unit area, R_{SH0} and series resistance per unit area, R_{S0}, over time.

From the **Table 5.2**, **Table 5.3** and **Table 5.4** we can analyze that at T_{80} for devices under encapsulation the lifetime is 12 times more than that air devices. Although degradation is higher for encapsulated devices in 21 times more than for devices stored in nitrogen environment, results show that both approaches protect the device from degradation compared to leaving them in air, remarking the importance of finding an efficient encapsulation procedure and material in order to extend the lifetime of the solar cells.

Table 5.5 shows the summary of values extracted from Eq. (1) (i.e. T1, T2, A1 and A2) for each group of cells analyzed under different environments. The result of divide A1/A2 was called as *r*. The calculated values of *r* when the samples were left in nitrogen, air and encapsulated environment presented and followed a behavior to be $r = 1$, $r > 1$ of 2.53 and $r < 1$ of 0.88, respectively.

Environment	A1 [%/%]	T1 [h]	A2 [%/%]	T2 [h]	r= A1/A2
Nitrogen	0.50	4800	0.50	4800	1 (r=1)
Air	0.76	10	0.30	80	2.53 (r>1)
Encapsulated	0.47	4800	0.53	80	0.88 (r<1)

Table 5.5 Parameters obtained from fit of the normalized PCE by Eq. (1) for each group of cells analyzed under different environments. T1 and T2 are the time constants, A1 and A2 are the degradation power factors and *r* is the ratio of A1/A2.

5.3.4. Optical microscopic images

Fig. 5.12 shows the optical microscope images of the superficial area of Ca/Ag metallic contact to observe the effect of degradation in different ambient for the analyzed devices. **Fig. 5.12 a**) and **b)** show the clean surface of the metallic contact for the samples right after fabrication. **Fig. 5.12 c)** and **d)** show the same surface after 5300 h in N_2 ambient, where small protrusions around of 500 nm are observed. **Fig. 5.12 e)** and **f)** show the contact surfaces in devices after 384 hours in air. The corrosion is more evident showing protrusions up to 1500 nm size. Ca is highly reactive with water and oxygen at room temperature, although the reaction with oxygen is less. [39] The enhanced degradation in air can be explained by this situation, since the presence of water in the air is relatively high, compared to the encapsulated devices, where the presence of oxygen is predominant in one period of its lifetime, or to the devices kept in N_2 only is predominant by the effects of chemical degradation between the materials of the layers. In all cases, the oxidized material causes an expansion in all directions resulting in the formation of protrusions on the outer electrode surface centered on the microscopic pinholes. [31, 40]

Other effects that can occur are the diffusion of Ag and Ca in combination with H_2O and O_2 continues into the active layer (PTB1:PCBM) causing a degradation everywhere.

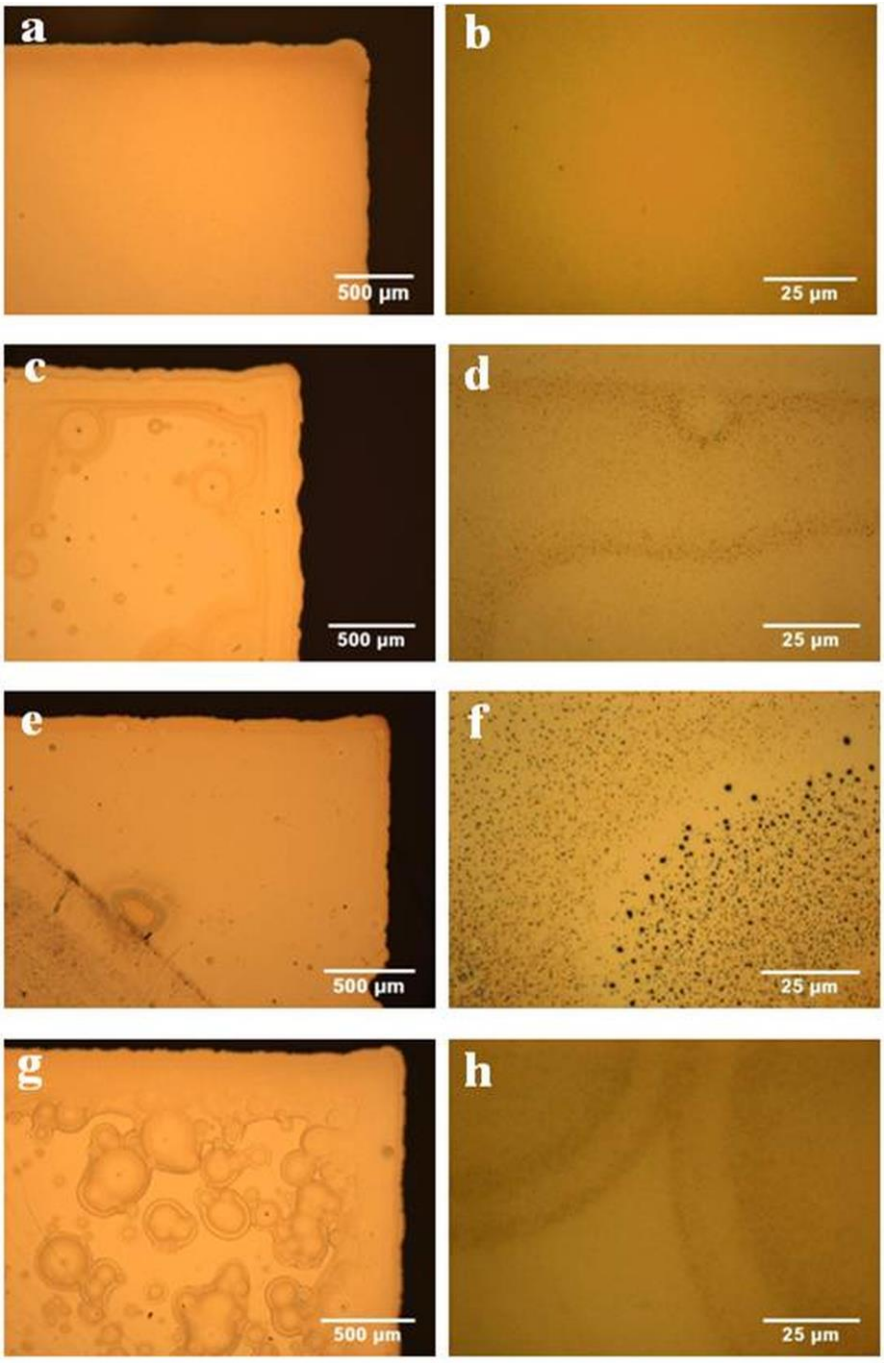

Fig. 5.12 Optical microscopic images of the metallic contact surface of PTB1:PCBM solar cells from all groups exposed in their different environments and degraded over time. Images a), c), e) and g) were obtained at 25 X of magnification and the images b), d), f) and h) were obtained at 500 X. The images a) and b) represent the metallic contact surface free of protrusions right after manufacture. Images c) and d) represent the metallic contact surface of S1 devices under nitrogen environment obtained at 5300 h; e) and f) are the images of S3 devices exposed in air environment obtained at 384 h; g) and h) are the images of S3 devices under encapsulation obtained at 5300 h.

This degradation could cause the loss of conjugation in the polymer, a decrease in the interface area between polymer/acceptor materials and the formation of organo-calcium, organo-silver and oxides compounds with the polymer. [41] Also, when the ITO and PEDOT:PSS interface is exposed to H_2O and O_2 the hygroscopic nature of PSS has the absorption of water in it can cause the etching of the ITO layer as already mentioned. [11] The distinctive *S*-shaped J–V curve measured under illumination that was observed in samples left in air can be attributed also to the formation of an insulating layer at the Ag/Ca electrode after reacting with water or oxygen, as reported in [42-44]. All these effects will be enhanced when devices are left in ambient conditions.

Fig. 5.12 g) and **h)** show contact surfaces in encapsulated devices, where the average size of protrusions was less than 300 nm after 5300 h. Although the size of the protrusion is smaller the damaged area is bigger, which it is consistent with the more pronounced degradation observed with respect to samples left in N_2.

In summary, the principal contribution to the decreases in the efficiency is the degradation of the polymer and the calcium electrode-polymer interface. The calcium is highly reactive with the water and oxygen due to low work function. Furthermore, the chemical interaction between the calcium electrode and the polymer may lead to polymer degradation, lowering device lifetimes.

Also there is good evidence from works on LEDs where the calcium can dope conjugated polymers affecting their lifetimes. [41, 45] Depending on the environment that is exposed the organic solar cells these presented a slow or fast time degradation ratio, as it was shown above. The values of time degradation ratio for devices under air compared to the values of devices stored in a nitrogen environment demonstrate that further research in encapsulation should lead to devices that function over extended periods of time.

5.4. Conclusions

In this contribution, we reported the lifetime and degradation of ITO/PEDOT:PSS/PTB1:PCBM/Ca/Ag solar cells in nitrogen and air environments and under encapsulation by the analysis of the time evolution of current-voltage characteristics both under illumination and dark applied ISOS-D1 protocols. In a nitrogen atmosphere the lifetime (T_{S80}) was 990 hours, in a ambient atmosphere the lifetime was 4 hours, and under encapsulation the lifetime was 48 hours. It has been shown that the evolution of the power conversion efficiency can be modelled by the sum of two decaying exponentials with time constants T1 and T2. The values extracted from the model were related with the degradation mechanism predominant, according the environment. The solar cells under N_2 environment to T_{S96} by 80 h and T_{S30} by 5300 h, the PCE decreased 4.3% and 69.4%, respectively. The time constant of degradation extracted from the model of *PCE* was $T1 = T2 = 4800$ h showing that only one degradation mechanism is acting in these conditions. Due to low quantity of water and oxygen in N_2 (<0.1 ppm), the mechanism responsible for the slow degradation was identified to the intrinsic chemical reactions of the polymeric materials. The solar cells under air conditions to T_{S10} by 80 h and T_{S1}

by 384 h, the PCE decreased 90.1% and 99.9%, respectively. The time constants of degradation extracted from the model of PCE were T1 = 10 h and T2 = 80 h showing two degradation mechanisms and dominating at different operation time during its life. The mechanisms responsible for the extremely rapid degradation were associated to chemical reaction of the active layer and/or electrodes with water and oxygen that diffuse into devices. Water was the dominant degradation mechanism observed in this environment having the lower time constant of degradation (T1). Finally solar cells under encapsulation to T_{S70} by 80 h and T_{S15} by 5300 h, the PCE decreased 29.1% and 85.1%, respectively. The time constants of degradation extracted from model of PCE were T1 = 4800 h and T2 = 80 h showing two degradation mechanisms too. The order of magnitude of the first time constant suggests that it corresponds with the same mechanism as observed under N_2 environment. On the other hand, the second time constant, similar to that observed under air environment, indicates that oxygen degradation is taking place under encapsulation. The main source of oxygen in these conditions might be the encapsulating/sealing material (EPT-HM), as it contains oxygen in its molecular structure.

These results show that the procedure followed in this work under ISOS-D1 protocols has permitted to gain knowledge of the main degradation mechanisms of the PTB1 donor polymer in the solar cells and thus to improve their reliability and durability.

5.5. References

[1] M.A. Green, K. Emery, Y. Hishikawa, W. Warta, E.D. Dunlop, Solar cell efficiency tables (version 42), *Prog. Photovolt: Res. Appl., 21* (2013) 827−837.

[2] H. Hoppe, N.S. Sariciftci, Organic solar cells: An overview, *J. Mater. Res., 19* (2004) 1924−1945.

[3] V.S. Balderrama, M. Estrada, A. Viterisi, P. Formentin, J. Pallarés, J. Ferré-Borrull, E. Palomares, L.F. Marsal, Correlation between P3HT inter-chain structure and Jsc of P3HT:PC[70]BM blends for solar cells, *Microelectron. Reliab., 53* (2013) 560−564.

[4] C.J. Brabec, Organic photovoltaics: technology and market, *Sol. Energy Mater. Sol. Cells, 83* (2004) 273−292.

[5] P. Heremans, D. Cheyns, B.P. Rand, Strategies for Increasing the Efficiency of Heterojunction Organic Solar Cells: Material Selection and Device Architecture, *Acc. Chem. Res., 42* (2009) 1740−1747.

[6] G. Chidichimo, L. Filippelli, Organic Solar Cells: Problems and Perspectives, *Int. J. Photoenergy Article, ID 123534* (2010) 1−11.

[7] Y. Zhang, Z. Li, S. Wakim, S. Alem, S.-W. Tsang, J. Lu, J. Ding, Y. Tao, Bulk heterojunction solar cells based on a new low-band-gap polymer: Morphology and performance, *Org. Electron., 12* (2011) 1211−1215.

[8] M. Helgesen, R. Sondergaard, F.C. Krebs, Advanced materials and processes for polymer solar cell devices, *J. Mater. Chem., 20* (2010) 36−60.

[9] G. Yu, J. Gao, J.C. Hummelen, F. Wudl, A.J. Heeger, Polymer Photovoltaic Cells: Enhanced Efficiencies via a Network of Internal Donor-Acceptor Heterojunctions, *Science, 270* (1995) 1789−1791.

[10] W. Cai, X. Gong, Y. Cao, Polymer solar cells: Recent development and possible routes for improvement in the performance, *Sol. Energy Mater. Sol. Cells, 94* (2010) 114−127.

[11] K. Kawano, R. Pacios, D. Poplavskyy, J. Nelson, D.D.C. Bradley, J.R. Durrant, Degradation of organic solar cells due to air exposure, *Sol. Energy Mater. Sol. Cells, 90* (2006) 3520−3530.

[12] S.A. Gevorgyan, M. Jørgensen, F.C. Krebs, A setup for studying stability and degradation of polymer solar cells, *Sol. Energy Mater. Sol. Cells, 92* (2008) 736−745.

[13] C.-Y. Chang, F.-Y. Tsai, Efficient and air-stable plastics-based polymer solar cells enabled by atomic layer deposition, *J. Mater. Chem., 21* (2011) 5710−5715.

[14] F.C. Krebs, S.A. Gevorgyan, J. Alstrup, A roll-to-roll process to flexible polymer solar cells: model studies, manufacture and operational stability studies, *J. Mater. Chem., 19* (2009) 5442−5451.

[15] M.H. Petersen, S.A. Gevorgyan, F.C. Krebs, Thermocleavable Low Band Gap Polymers and Solar Cells Therefrom with Remarkable Stability toward Oxygen, *Macromolecules, 41* (2008) 8986−8994.

[16] F.C. Krebs, H. Spanggaard, Significant Improvement of Polymer Solar Cell Stability†, *Chem. Mater., 17* (2005) 5235−5237.

[17] K. Norrman, S.A. Gevorgyan, F.C. Krebs, Water-Induced Degradation of Polymer Solar Cells Studied by H218O Labeling, *ACS Appl. Mater. Interfaces, 1* (2009) 102−112.

[18] J. Hou, H.-Y. Chen, S. Zhang, G. Li, Y. Yang, Synthesis, Characterization, and Photovoltaic Properties of a Low Band Gap Polymer Based on Silole-Containing Polythiophenes and 2,1,3-Benzothiadiazole, *J. Am. Chem. Soc., 130* (2008) 16144−16145.

[19] Y. Liang, Y. Wu, D. Feng, S.T. Tsai, H.J. Son, G. Li, L. Yu, Development of new semiconducting polymers for high performance solar cells, *J. Am. Chem. Soc., 131* (2009) 56−57.

[20] Y. Liang, D. Feng, Y. Wu, S.-T. Tsai, G. Li, C. Ray, L. Yu, Highly Efficient Solar Cell Polymers Developed via Fine-Tuning of Structural and Electronic Properties, *J. Am. Chem. Soc., 131* (2009) 7792−7799.

[21] Y. Liang, L. Yu, A New Class of Semiconducting Polymers for Bulk Heterojunction Solar Cells with Exceptionally High Performance, *Acc. Chem. Res., 43* (2010) 1227−1236.

[22] J. Guo, Y. Liang, J. Szarko, B. Lee, H.J. Son, B.S. Rolczynski, L. Yu, L.X. Chen, Structure, Dynamics, and Power Conversion Efficiency Correlations in a New Low Bandgap Polymer: PCBM Solar Cell, *J. Phys. Chem. B, 114* (2009) 742−748.

[23] M. Jørgensen, K. Norrman, F.C. Krebs, Stability/degradation of polymer solar cells, *Sol. Energy Mater. Sol. Cells, 92* (2008) 686−714.

[24] R. Pacios, A.J. Chatten, K. Kawano, J.R. Durrant, D.D.C. Bradley, J. Nelson, Effects of Photo-oxidation on the Performance of Poly[2-methoxy-5-(3′,7′-dimethyloctyloxy)-1,4-phenylene vinylene]:[6,6]-Phenyl C61-Butyric Acid Methyl Ester Solar Cells, *Adv. Funct. Mater., 16* (2006) 2117−2126.

[25] M.O. Reese, S.A. Gevorgyan, M. Jørgensen, E. Bundgaard, S.R. Kurtz, D.S. Ginley, D.C. Olson, M.T. Lloyd, P. Morvillo, E.A. Katz, A.

Elschner, O. Haillant, T.R. Currier, V. Shrotriya, M. Hermenau, M. Riede, K. R. Kirov, G. Trimmel, T. Rath, O. Inganäs, F. Zhang, M. Andersson, K. Tvingstedt, M. Lira-Cantu, D. Laird, C. McGuiness, S. Gowrisanker, M. Pannone, M. Xiao, J. Hauch, R. Steim, D.M. DeLongchamp, R. Rösch, H. Hoppe, N. Espinosa, A. Urbina, G. Yaman-Uzunoglu, J.-B. Bonekamp, A.J.J.M. van Breemen, C. Girotto, E. Voroshazi, F.C. Krebs, Consensus stability testing protocols for organic photovoltaic materials and devices, *Sol. Energy Mater. Sol. Cells, 95* (2011) 1253−1267.

[26] M. Jørgensen, K. Norrman, S.A. Gevorgyan, T. Tromholt, B. Andreasen, F.C. Krebs, Stability of Polymer Solar Cells, *Adv. Mater.*, *24* (2012) 580−612.

[27] D.M. Tanenbaum, M. Hermenau, E. Voroshazi, M.T. Lloyd, Y. Galagan, B. Zimmermann, M. Hosel, H.F. Dam, M. Jorgensen, S.A. Gevorgyan, S. Kudret, W. Maes, L. Lutsen, D. Vanderzande, U. Wurfel, R. Andriessen, R. Rosch, H. Hoppe, G. Teran-Escobar, M. Lira-Cantu, A. Rivaton, G.Y. Uzunoglu, D. Germack, B. Andreasen, M.V. Madsen, K. Norrman, F.C. Krebs, The ISOS-3 inter-laboratory collaboration focused on the stability of a variety of organic photovoltaic devices, *RSC Adv., 2* (2012) 882−893.

[28] H.B. Yang, Q.L. Song, C. Gong, C.M. Li, The degradation of indium tin oxide / pentacene / fullerene / tris-8-hydroxy - quinolinato aluminum / aluminum heterojunction organic solar cells: By oxygen or moisture?, *Sol. Energy Mater. Sol. Cells, 94* (2010) 846−849.

[29] F.C. Krebs, J.E. Carlé, N. Cruys-Bagger, M. Andersen, M.R. Lilliedal, M.A. Hammond, S. Hvidt, Lifetimes of organic photovoltaics: photochemistry, atmosphere effects and barrier layers in ITO-

MEHPPV:PCBM-aluminium devices, *Sol. Energy Mater. Sol. Cells, 86* (2005) 499−516.

[30] E. Voroshazi, B. Verreet, T. Aernouts, P. Heremans, Long-term operational lifetime and degradation analysis of P3HT:PCBM photovoltaic cells, *Sol. Energy Mater. Sol. Cells, 95* (2011) 1303−1307.

[31] M. Hermenau, M. Riede, K. Leo, S.A. Gevorgyan, F.C. Krebs, K. Norrman, Water and oxygen induced degradation of small molecule organic solar cells, *Sol. Energy Mater. Sol. Cells, 95* (2011) 1268−1277.

[32] M. Al-Ibrahim, O. Ambacher, S. Sensfuss, G. Gobsch, Effects of solvent and annealing on the improved performance of solar cells based on poly(3-hexylthiophene): Fullerene, *Appl. Phys. Lett., 86* (2005) 2011201−2011203.

[33] A. Seemann, H.J. Egelhaaf, C.J. Brabec, J.A. Hauch, Influence of oxygen on semi-transparent organic solar cells with gas permeable electrodes, *Org. Electron., 10* (2009) 1424−1428.

[34] X. Wang, C. Xinxin Zhao, G. Xu, Z.-K. Chen, F. Zhu, Degradation mechanisms in organic solar cells: Localized moisture encroachment and cathode reaction, *Sol. Energy Mater. Sol. Cells, 104* (2012) 1−6.

[35] B. Ecker, J.C. Nolasco, J. Pallarés, L.F. Marsal, J. Posdorfer, J. Parisi, E. von Hauff, Degradation Effects Related to the Hole Transport Layer in Organic Solar Cells, *Adv. Funct. Mater., 21* (2011) 2705−2711.

[36] V.S. Balderrama, M. Estrada, A. Cerdeira, B.S. Soto-Cruz, L.F. Marsal, J. Pallares, J.C. Nolasco, B. Iñiguez, E. Palomares, J. Albero, Influence of P3HT:PCBM blend preparation on the active layer morphology and cell degradation, *Microelectron. Reliab., 51* (2011) 597−601.

[37] N. Grossiord, J.M. Kroon, R. Andriessen, P.W.M. Blom, Degradation mechanisms in organic photovoltaic devices, *Org. Electron., 13* (2012) 432−456.

[38] M.P. Nikiforov, J. Strzalka, S.B. Darling, Delineation of the effects of water and oxygen on the degradation of organic photovoltaic devices, *Sol. Energy Mater. Sol. Cells, 110* (2013) 36−42.

[39] S. Cros, M. Firon, S. Lenfant, P. Trouslard, L. Beck, Study of thin calcium electrode degradation by ion beam analysis, *Nucl. Instrum. Methods Phys. Res., Sect. B, 251* (2006) 257−260.

[40] K. Norrman, N.B. Larsen, F.C. Krebs, Lifetimes of organic photovoltaics: Combining chemical and physical characterisation techniques to study degradation mechanisms, *Sol. Energy Mater. Sol. Cells, 90* (2006) 2793−2814.

[41] M.O. Reese, A.J. Morfa, M.S. White, N. Kopidakis, S.E. Shaheen, G. Rumbles, D.S. Ginley, Pathways for the degradation of organic photovoltaic P3HT:PCBM based devices, *Sol. Energy Mater. Sol. Cells, 92* (2008) 746−752.

[42] D. Gupta, M. Bag, K.S. Narayan, Correlating reduced fill factor in polymer solar cells to contact effects *Appl. Phys. Lett., 92* (2008) 0933011−0933013.

[43] Wagenpfahl, D. Rauh, M. Binder, C. Deibel, V. Dyakonov, S-shaped current-voltage characteristics of organic solar devices, *Phys. Rev. B, 82* (2010) 1153061−1153069.

[44] J. Schafferhans, A. Baumann, A. Wagenpfahl, C. Deibel, V. Dyakonov, Oxygen doping of P3HT:PCBM blends: Influence on trap states, charge

carrier mobility and solar cell performance, *Org. Electron., 11* (2010) 1693−1700.

[45] A.C. Grimsdale, K.L. Chan, R.E. Martin, P.G. Jokisz, A.B. Holmes, Synthesis of light-emitting conjugated polymers for applications in electroluminescent devices, *Chem. Rev., 109* (2009) 897−1091.

Chapter 6

Design, manufacture and analysis of interfacial charge recombination in interdigitated P3HT/$PC_{70}BM$ solar cells

In this chapter interdigitated heterojunction photovoltaic devices were manufactured. The donor layer of P3HT nanopillars was fabricated by soft nanoimprinting using nanoporous anodic alumina templates. Subsequently, the $PC_{70}BM$ acceptor layer was deposited by spin coating on top of the P3HT nanopillars using a solvent that would not dissolve any of the previous material. Anisole solvent was used because it does not dissolve the bottom donor layer of nanopillars and provides a good wettability between the two materials. Charge extraction was used to determine the charge carrier densities *n* on the interdigitated heterojunction under operating conditions. Moreover, transient photovoltage measurements were used to find the recombination rate constant in

combination with the charge carrier density. At the same time, the interdigitated structure was also compared with the bulk heterojunction and bilayer solar cells manufactured with the same polymeric and fullerene materials in order to understand the recombination loss mechanisms in the ordered and disordered nanomorphology of the active layers.

6.1. Introduction

In recent years intense efforts has been put into developing organic solar cells (OSC) that are at least as profitable as inorganic ones. The advantages of their low cost, light-weight, large area, flexibility and ease of processing make organic materials an attractive medium.[1, 2] The power conversion efficiency of photovoltaic devices has been improved by designing and synthesizing new materials with low band-gaps, changing the structure of devices [3], controlling the nanoscale morphology with additives, applying thermal or solvent annealing, controlling evaporation with solvents [4, 5] to increase the interfacial area between donor and acceptor [6], and making nanostructure morphologies such as nanogratings, nanopillars, nanorods and nanodots. [3, 7-10]. In order to improve the performance parameters, nanostructured morphologies were fabricated with poly (3-hexylthiophene) (P3HT)/[6,6]-phenyl-C61-butyric acid methyl (PCBM), and P3HT/C_{60}. Power conversion efficiency was reported to be around 1.1-3.25%. [9-15]

It is well known that power conversion efficiency is limited, among other factors by the diffusion length of excitons in the photoactive layer after they have been generated (typically this length is in the range of tens of nanometers in most organic semiconductors). [16-18] To prevent the loss of excitons before dissociation the morphology must be bi-continuous donor-

acceptor if the free electrons and holes are to be transported and collected at their respective metal electrodes, (e.g. bulk heterojunctions (BHJ) present this morphology).[19-21]

One promising way to increase the power conversion efficiency of polymer photovoltaic cells is to fabricate well-controllable ordered interdigitated heterojunction nanomorphology (IHJN) by soft nanoimprinting. The advantage of IHJN is that almost all the excitons formed are close enough to the interface to be dissociated into electrons and holes and nearly all the free charge carriers can travel along the uninterrupted pathway of the material until they reach their respective electrodes. The vertical IHJN allows the domains in the p-type donor material and the n-type acceptor material to be aligned normal to the electrode surfaces, thus increasing their crystallinity and charge carrier mobility and reducing recombination rates inside the device. [17, 22] The main progress in IHJN has been achieved by new fabrication techniques and technologies. The interdigitated nanostructures (INS) can be manufactured by nanoimprint lithography (NIL) [23], solvent-assisted nanoimprinting lithography (SANIL) [10], electron-beam lithography (EBL) [15], spin-coating and nanoimprinting template-based methods [11, 14, 24], among many others.[3, 7, 25-29] The various methods of nanoimprint lithography use silicon wafers and are usually expensive. The process involves thermal imprinting at high temperature and a considerable amount of time for appropriate heating and cooling. [30] Here we report the use of the nanoimprinting method in which nanoporous anodic alumina templates (NAATs) are used to fabricate INS in a cost effective and straightforward fashion. [24] NAATs are widely used as template material because they are porous have a good hexagonal order and the geometric characteristics can be easily controlled. [31-33] NAATs and soft nanoimprinting can be combined to provide the vertical nanostructured polymer

and the temperature, pressure, and time of the imprint can be precisely controlled. [13, 25, 34]

In order to get the complete IHJN structure for OSC application after the polymer nanostructure has been manufactured, a method must be chosen for depositing and infiltrating the acceptor material (i.e. derivative fullerene) on the nanopatterned layer. Some of the best known methods are: thermal evaporation deposition (generally used for small molecules such as C_{60}, C_{70} because of their low solubility in organic solvents [35]), double nanoimprinting and spin-coating. [9, 11, 22] Here, we report the use of spin-coating to deposit the acceptor material onto the interdigitated polymer layer, because it has proven to be an effective, simple, and low-cost process. Two requirements must be satisfied: first the acceptor solution needs to be orthogonal so that it dissolves the acceptor material but not the donor; second the solvent must wet the donor material so that the acceptor material can spread uniformly over and into the nanostructure. Orthogonal solvents reported with these requirements are dichloromethane and 2-butanone. [22, 36-38]

In this chapter, we used the combination of spin coating and soft nanoimprinting by NAATs to obtain conformal thin films of nanopillars (NP) as donor layer, which made it possible to fabricate several P3HT/$PC_{70}BM$ solar cell devices after the P3HT–NP had been infiltrated with $PC_{70}BM$. Anisole (C_7H_8O) solvent was used to dissolve the fullerene without destroying the donor layer. Bulk heterojunction (BHJ) and bilayer (BL) organic solar cells were fabricated for purpose of comparison with interdigitated solar cells. The fabrication process and conditions were very similar to those of the interdigitated cells.

Once the photovoltaic device with IHJN had been obtained, we then need to understand the physical processes involved in device operation. Such typical electrical characterization as current–voltage (J–V) is not enough to

understand the dynamics or how the device will perform. Some key parameters for better understanding the factors that limit the power conversion efficiency are the charge density distribution and the recombination dynamics. Typical techniques used to measure the previous parameters above mentioned are: charge extraction by linear increasing voltage (CELIV), double injection current (DoI), charge extraction (CE), integral mode of flight (Q-TOF), transient photovoltage (TPV), transient absorption spectra (TAS), etc. [39, 40]

Therefore, in the second part of this contribution we apply the CE and TPV measurements to the IHJN solar cell under steady state operating conditions with the aim of analyzing and determining the charge densities, the carrier recombination dynamics and carrier lifetime dependency on voltage. These measurements are often used in research on BHJ solar cells [41-43] and dyes sensitized solar cells [44], but have not previously been applied to interdigitated structures. Indeed, all the results obtained from the optoelectronic techniques used in this study (CE and TPV) reveal that its interdigitated device nanomorphology is a determining geometric factor that directly affects the charge carrier density, recombination losses and FF during device operation.

6.2. Materials and methods

This section discusses the fabrication process and the preparation of nanoporous alumina anodic templates. The printing process was combined with NAAT to generate an interdigitated morphology structure on polymeric flat film. Then, the fullerene material was deposited on the top surface of the interdigitated morphology manufactured to get the bi-continuous active layer. Finally, the interdigitated heterojunction organic solar cells were characterized electrically and optically so that we could understand the recombination process

that takes place inside the device structures. Bulk heterojunction and bilayer organic solar cells were manufactured as control devices.

6.2.1. Materials and fabrication

Materials. ITO-coated glass substrates (with a nominal sheet resistance of 15 ohm/square and a thickness of 120 nm) were purchased from PsiOTec Ltd. PEDOT:PSS FHC was acquired from Ossila Ltd., P3HT (melting point 238 ºC, *Mw* = 17500 g mol^{-1}, 99.995% regio-regularity) and $PC_{70}BM$ (M_w = 1031.0 g mol^{-1}) were purchased from Sigma-Aldrich and Solenne BV, respectively. High-purity (99.99%) silver wire was obtained from Testbourne Ltd., and calcium pellets with high-purity (99.99%) were purchased from Kurt J. Lesker.

Fabrication of NAAT. The NAAT samples were fabricated by the two-step anodization process. Before anodizing, aluminium (Al) substrates were electropolished in a mixture of ethanol (EtOH) and perchloric acid ($HClO_4$) 4:1 (*v*:*v*) at 20 V for 3 min. After this, the first anodization step was performed in an aqueous solution of oxalic acid ($H_2C_2O_4$) 0.3 M at 40 V and 5ºC for 24 h. Subsequently, the alumina film was selectively dissolved by wet chemical etching in a mixture of phosphoric acid (H_3PO_4) 0.4 M and chromic acid (H_2CrO_7) 0.2 M at 70ºC. Then, the second anodization step was conducted under the same anodization conditions as the first step. The anodization time during this step was adjusted to 60 seconds in order to modify the pore length. Finally, the pore diameter was enlarged by a wet chemical etching procedure in an aqueous solution of H_3PO_4 5 wt%. Subsequently, the NAAT were modified by DPMS (DMS-T22) to reduce the surface energy of the templates, and the reaction mechanism was explained by Krumpfer and co-autors.[53] The NAAT

were immersed in DPMS at 120°C for 24 h, and then rinsed with toluene, and then acetone, ethanol, and DI water. Finally the substrates were dried with nitrogen.

Device fabrication. Appendix E is depicted the process fabrication. Photovoltaic IHJN–OSC devices were fabricated on pre-cleaned patterned ITO glass substrates. 40 nm PEDOT:PSS was applied to the substrates by spin coating at 3500 rpm for 45 s. The PEDOT:PSS film was annealed at 110 ºC for 20 min. The P3HT solution was prepared in chlorobenzene (C_6H_5Cl) and was then spin-coated onto the PEDOT:PSS / ITO glass under nitrogen and a thin film of P3HT was obtained. Afterwards, the nanoimprinting was optimized and carried out with the NAATs by applying 2 MPa at 60 ºC for 5 min to the previous P3HT layer fabricated to get P3HT–NP. The $PC_{70}BM$ solution was prepared in anisole solvent (C_7H_8O) at 10 mg/ml and was deposited on top of P3HT–NP by spin coating at 3000 rpm to backfill the spaces between the nanopillar arrays and form a continuous $PC_{70}BM$ thin film on top. This process was conducted as rapidly as possible to avoid any possible interfacial mixing.

BHJ–OSC and planar bilayer (BL)–OSC were manufactured for purposes of comparison with the IHJN-OSC. BL–OSCs were fabricated under the same conditions as the IHJN–OSC, but without the nanoimprinting process.

BHJ-OSCs were manufactured using the same ITO substrates and PEDOT:PSS layer as for the IHJN. A blend of P3HT:$PC_{[70]}BM$ (ratio 1:1) was prepared in chlorobenzene (CB) solution and then stirred for 18 h at 40 ºC. The active layer was deposited by spin coating at 600 rpm for 45 s. Afterwards, all the structures (i.e. IHJN–OSC, BHJ–OSC and BL–OSC) deposited the metal contact by evaporation through a shadow to give devices with an active area of 0.09 cm^2. Ca (20 nm) and Ag (100nm) were deposited at a rate of 0.15 Å s^{-1} and

0.5–0.8 Å s^{-1} respectively. Then, a post-processing annealing was carried out by heating at 130°C for 20 min.

6.2.2. Optical and electrical characterization

NAAT and structures characterization. The NAAT samples and IHJN–OSC, BHJ–OSC and BL–OSC structures were characterized by environmental scanning electron microscopy (ESEM FEI Quanta 600). The standard image processing package (ImageJ, a public domain program developed at the RSB of the NIH, USA) was used to carry out the ESEM image analysis. Photoluminescence (PL) was measured in a fluorescence spectrophotometer from Photon Technology International Inc. for the three kinds of structures. A Xe lamp was used as the excitation light source at room temperature with an excitation wavelength (λ_{ex}) of 510 nm and an emission spectrum at an angle of 20º. The absorption spectrum was measured for the three sets of IHJN, BHJ and BL structures at room temperature with a Perkin Elmer Lambda 950 UV/VIS/NIR spectrometer. Atomic force microscopy (AFM Agilent 6400) was used to make several characterizations of the surface morphology of IHJN, BHJ and BL layer structures in the tapping mode.

Device testing. The current density-voltage (J–V) characteristics of the devices were measured at room temperature using a Keithley 2400 source measurement unit in combination with a solar simulator (Abet Technologies model 11000 class type A, Xenon arc), automatically controlled with a computer. Appropriate filters were used to reproduce the AM 1.5G spectrum. A light intensity of 100 mW/cm^2 was applied to test the organic solar cell devices under illumination. The light intensity was calibrated with an NREL certified monocrystalline silicon photodiode. Film thicknesses were measured by a Dektak 150 surface profilometer. In addition, J–V dark curves were recorded for all the photovoltaic devices.

The CE was used to determine the distribution of charge carrier densities (n) in devices under different conditions of light and voltage. The general CE procedure is to leave the device in open circuit conditions while illuminated at different intensities. Then, the device is shorted while simultaneously turning off the light, and the resulting discharging current transient through a small external load resistor is measured. The desired illumination intensity is achieved with a white light LED ring from LUXEON® Lumileds connected to a DC power supply and a TGP110 function generator that allows the LEDs to reach a background illumination up to 1 sun on the ITO side of the device. The LEDs were typically turned on for approximately 100 ms so that they could reach steady state conditions. The LEDs have a rise/fall time of <100 ns. After the light is switched off and the circuit is temporally closed, while charges are forced to pass through a TDS 2022 oscilloscope from Tektronix© that records the drop in voltage across a resistance of 50 Ω.

In TPV measurements, devices are connected to the 1M Ω input terminal of a Tektronix© TDS2022 oscilloscope and the background illumination was obtained from a ring of 6 white LEDs from LUXEON®. The small perturbation (5mV) was applied through a light pulse (N_2 laser nominal wavelength, 50 ns pulses). The charge recombination rate was calculated for illumination intensities ranging from 0.1 sun to 1 sun.

6.3. Results and discussion

6.3.1. ESEM characterization of NAAT and IHJN

The NAATs were prepared by the two-step anodization process as is shown in **Table 6.1.** [31-33]

	oxalic acid	V_{anod}[a] (V)	t_{anod} (1st step)[b] (h)	t_{anod} (2nd step) (s)	t_{pw}[c] (min)
Template	$H_2C_2O_4$ (0.3 M)	40	24	60	14

Table 6.1 Fabrication conditions of nanoporous anodic alumina template. [a] V_{anod} is anodization voltage. [b] t_{anod} is anodization time. [c] t_{pw} is pore-widening time.

The pore length was controlled by the anodization time and the pore diameter was enlarged by a wet chemical etching procedure after anodization. The pore diameter (ϕ_p), pore length (H_p) and interpore distance (d_{int}) are shown in Table 6.2. The fabrication conditions of the NAAT sample are summarized in **Table 6.2** and **s**hown in **Fig. 6.1**.

	ϕ_p[a] (nm)	H_p[b] (nm)	d_{int}[c] (nm)
Template of NAA (twenty samples)	60 ± 4	80 ± 5	100 ± 4

Table 6.2. Average geometric characteristics obtained from NAAT.

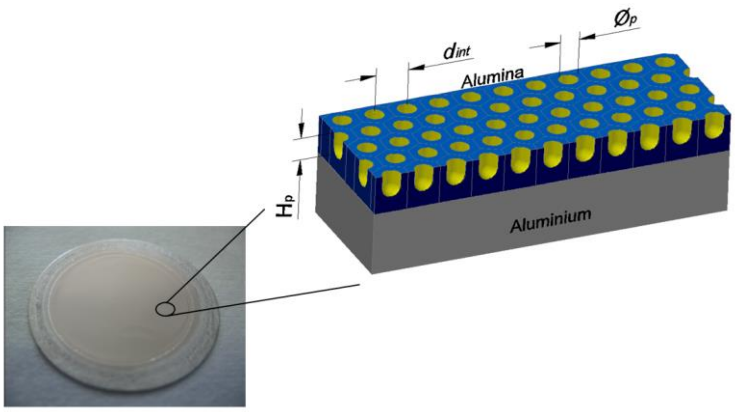

Fig. 6.1 NAAT shows all its geometric characteristics.

The NAATs were modified by dimethylpolysiloxane (DPMS) to reduce the surface energy of the templates as was described in the experimental section. The results showed that they became more hydrophobic, as is reported in [14]. **Fig. 6.2 A, B and C** show the top-view, tilt-view and cross section-view provided by environmental scanning electron microscopy (ESEM) images of the NAATs after fabrication with oxalic acid electrolyte ($H_2Cr_2O_7$).

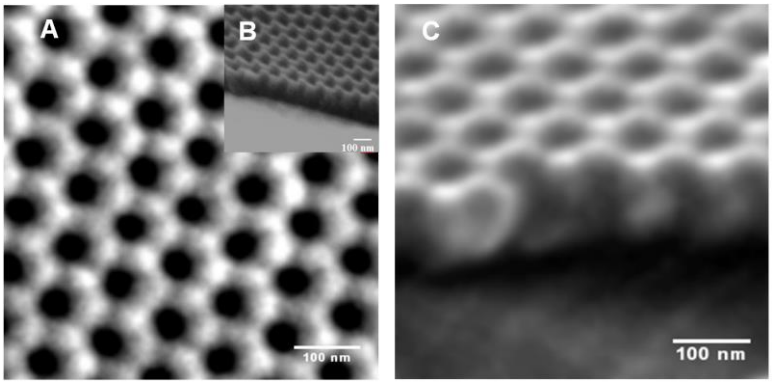

Fig. 6.2 ESEM images of NAAT. (A) Top-view, (B) tilt-view and (C) cross section-view of NAAT. The geometrical characteristics were: ϕ_{pore} = 60 ± 4 nm, H_{pore} = 80 ± 5 nm and d_{inter} = 100 ± 4 nm.

The preparation of IHJN–OSC based on P3HT–NP arrays is shown in **Fig. 6.3 (A-G)**.

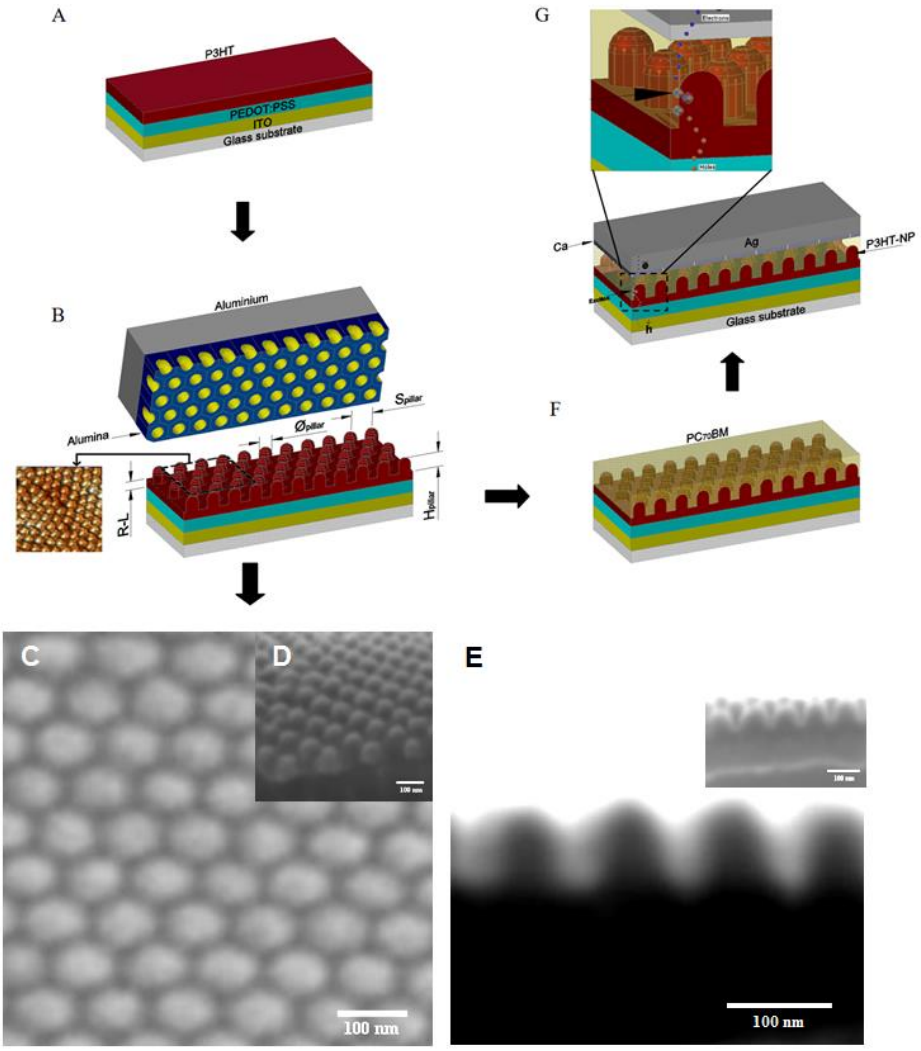

Fig. 6.3 The procedure for obtaining the interdigitated OSC. (A) Spin coating of the P3HT layer on PEDOT:PSS/ITO/Glass. (B) Patterning of P3HT–NP structure done by soft nanoimprinting combining with NAAT templates. The geometrical characteristics of the P3HT–NP can be seen. ϕ_{pillar} is the diameter of the nanopillar, H_{pillar} is the height of nanopillar, S_{pillar} is the distance between nanopillars and R-L is the residual layer of

the structure. (C) Top-view of P3HT–NP with excellent replication by soft NAAT applied with ϕ_{pillar} = 60 ± 4 nm. (D) Tilt view and (E) cross section of P3HT–NP with H_{pillar} = 80 ± 3 nm, S_{pillar} = 100 ± 5 nm, R-L = 45 ± 3 nm. (F) Deposition by spin coating of $PC_{70}BM$ using anisole solvent on the P3HT–NP. (G) Deposition of calcium and silver by thermal evaporation on the previous layers to obtain the IHJN–OSC.

The fabrication process of the IHJN–OSC first required P3HT to be deposited on a structure prepared from poly-(ethylene dioxythiophene) doped with poly-(styrene sulphonic acid) (PEDOT:PSS) / indium tin oxide (ITO) as is shown in **Fig. 6.3A**. The thickness of the P3HT layer was measured by profilometry to be of 130 nm. Then, a soft nanoimprinting process was applied to the prepared NAATs with an antiadhesion layer to imprint the polymer. Hydraulic charge pressure was applied in combination with temperature to produce nanopillars on the P3HT layer. Finally, the mold is released from the sample, and polymer nanoimprinting with negative replication of the mold is obtained (see **Fig. 6.3B**). We optimized the soft nanoimprinting conditions (i.e. time, pressure and temperature) to ensure the fidelity of the nanoporous patterns from the NAAT for the P3HT nanopillars as was described in the experimental section. The geometric parameters that define P3HT–NP are the pillar diameter (ϕ_{pillar}), pillar height (H_{pillar}), interpillar distance (S_{pillar}) and residual layer (R-L). **Fig. 6.3C, D and E** show top-view, tilt-view and cross section-view ESEM images of the P3HT–NP, respectively. The P3HT–NP has an average ϕ_{pillar}= 60±4 nm, H_{pillar}= 80±3 nm, S_{pillar}= 100±5 nm and R-L = 40±3 nm with an aspect ratio of 1.3. Subsequently, the $PC_{70}BM$ fullerene material was deposited by spin coating directly on top of the P3HT–NP layer using anisole solution (2 wt %) as is shown in **Fig. 6.3F**. In this study, we chose $PC_{70}BM$ for two reasons. First, the material has relatively strong and broad absorption in the visible range from 400 nm to 700 nm and gives better results in photon harvesting in the active layer than when such other fullerenes as C_{60}, C_{70} and PCBM are used. [45] The

literature only reports the interdigitated nanostructures OSC fabricated with C_{60} and PCBM, not with $PC_{70}BM$. Second, $PC_{70}BM$ can be dissolved in anisole solvent and deposited by spin coating onto the P3HT–NP. The spaces between the P3HT nanopillars were filled with the $PC_{70}BM$ mixture and the anisole solvent. The nanoimprinting polymer layer was not destroyed when the mixture was deposited.[37, 38] Dichloromethane (CH_2Cl_2) has sometimes been used to dissolve the PCBM and fabricate the nanostructured OSC. [9, 14, 15] Anisole is another solvent that may potentially be used for the fabrication of nanostructured cells but, to date, it has not been reported in the literature. Anisole solvent has been used to fabricate organic thin film transistors (OTFT) where the various polymer layers have to be deposited using orthogonal solvents. [36, 37] In this study, it is worth noting that $PC_{70}BM$ is used in combination with anisole solvent. It is the first time that this method has been used to deposit $PC_{70}BM$ into the gaps in the P3HT–NP and get the IHJN–OSC. Subsequently, the samples were placed inside the evaporation chamber, where a thin layer of calcium (Ca) and silver (Ag) were evaporated as a top contact (parameters and condition are given in the **Experimental Section**) as is shown in **Fig. 6.3G**.

Fig. 6.4A shows the cross section-view of the IHJN–OSC structure captured by ESEM. On some samples infiltrated with the fullerene material (P3HT–NP/$PC_{70}BM$) Ca (20nm) and one thin layer of Ag (10 nm) were deposited so that the stack material covered the top surface of the previous active layer, (see **Fig. 6.4B**). Finally, **Fig. 6.4C** shows the top view of the top surface of the Ag metal contact with a thickness of 100 nm.

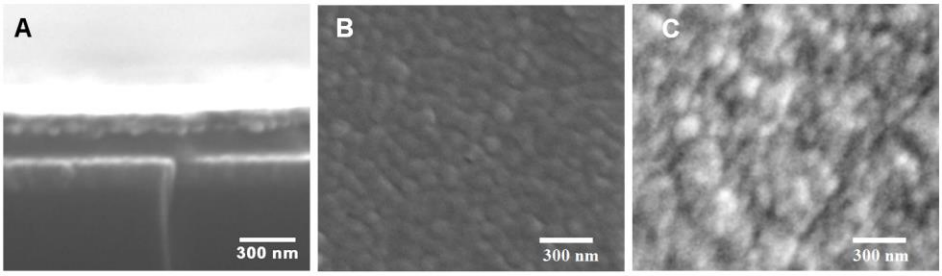

Fig. 6.4 (A) ESEM images from the cross section of IHJN–OSC with the stack ITO/PEDOT:PSS/P3HT–nanopillar/$PC_{70}BM$/Ca/Ag. (B) Top view after the evaporation of Ca (20 nm) and Ag (20 nm) onto the surface of $PC_{70}BM$/P3HT–nanopillars, (C) Top view of the Ca/Ag metal contact with a thickness of 20 nm/100 nm, respectively.

Two types of control cell based on BHJ–OSC standard blend films (by spin coating from a mixture solution) and planar bilayer BL–OSC (by non-patterned imprinting) were fabricated for purposes of comparison (parameters and conditions are given in the **Experimental Section**). The BHJ–OSC has the architecture ITO/PEDOT:PSS/P3HT:$PC_{70}BM$/Ca/Ag and BL–OSC has the stack ITO/PEDOT:PSS/P3HT/$PC_{70}BM$/Ca/Ag (see **Fig. 6.5**).

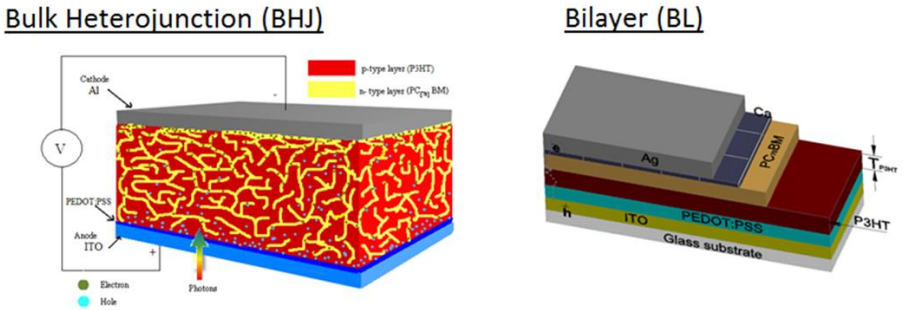

Fig. 6.5 Additional organic photovoltaic structures manufactured for purposes of comparison with the IHJN structure.

6.3.2. AFM characterization

Atomic force microscopy (AFM) in tapping mode was applied to P3HT–NP, P3HT:$PC_{70}BM$–BHJ and P3HT–single layers after thermal annealing, in order to get further insight into their respective surface areas (see **Fig. 6.6**). **Fig. 6.6 A, D** and **G** show the topography images of P3HT–NP revealing a periodically structured top surface with an average nanopillar height of ~ 80 nm and interpillar distance ~100 nm as was seen in the ESEM images. P3HT:$PC_{70}BM$–BHJ has an average surface height of 13.39 nm and the P3HT–single layer has an average surface height of 23 nm, respectively. **Fig. 6.6 B, E** and **H** show the phase image and **Fig. 6.6 C, F** and **I** the tilt view of the P3HT–NP, P3HT:$PC_{70}BM$–BHJ and P3HT–single layer, respectively.

6.3.3. UV-vis and PL characterization

Pristine P3HT–NP, P3HT flat film and P3HT/$PC_{70}BM$–IHJN, P3HT:$PC_{70}BM$–BHJ and P3HT/$PC_{70}BM$–BL films were studied by UV-vis spectroscopy as shown in **Fig. 6.7A**. In the UV-vis spectrum, we see that the absorbance of P3HT nanopillar films is 13% higher than that of P3HT flat film at 510 nm, which is consistent with previous reports. [10, 11] A small red-shift was observed for the imprinted film compared to the flat film. Moreover, imprinted P3HT–NP showed a pronounced increase in the shoulder centered at ~ 605 nm, the intensity of which is correlated with the degree of P3HT crystallinity. This is attributed to the fact that P3HT has a greater conjugation length and more ordered structure than the P3HT flat film because of the self - organization of the mobile chains is done during the heating and imprinting of the film compared to P3HT flat film. [22]

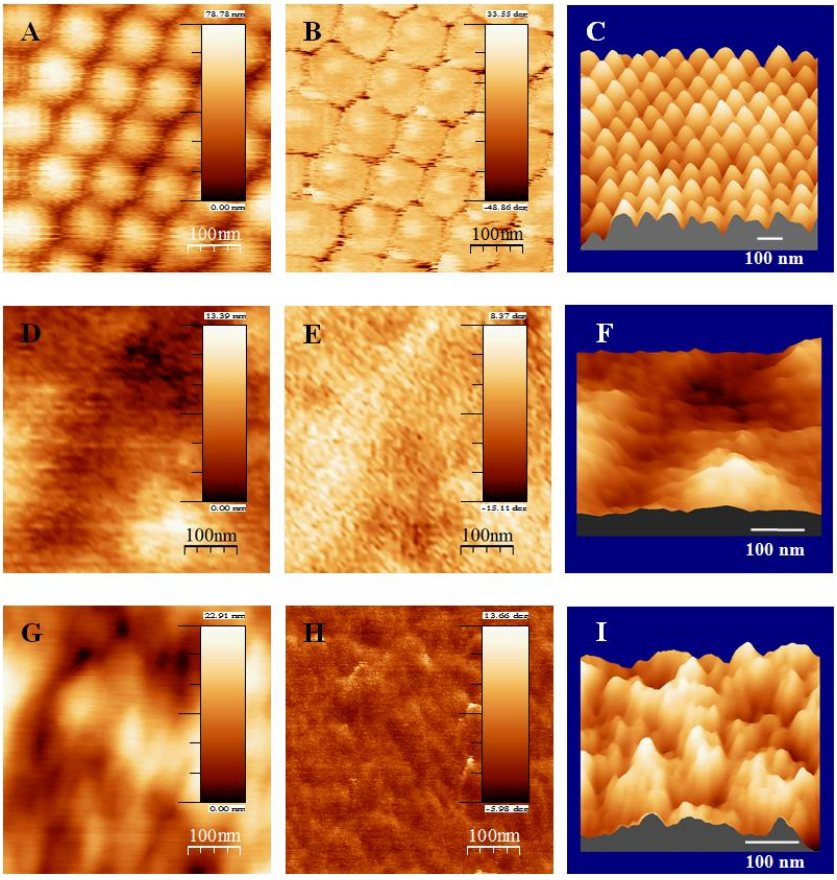

Fig. 6.6 (A, B, C) AFM morphology, phase and tilt view images of the P3HT–NP layer after soft nanoimprinting by NAAT. (D, E, F) AFM morphology, phase and tilt view images of the P3HT:$PC_{70}BM$–BHJ layer after spin coating deposition. (G, H, I) AFM morphology, phase and tilt view images of the P3HT–single layer after spin coating deposition. All the layers underwent thermal annealing at T = 130°C for t = 20 min.

Thermal annealing was applied during and after imprinting and mainly helped to remove residual solvent and reduce the free volume, which led to closer packing of the polymer chains and improved holes mobility. [46] To enhance the absorbance when nanopillars were used, the geometry had to be

optimum (i.e. pillar diameter, pillar height and interpillar distance) so that the light trapping ability inside the structure was also optimum as some simulations have shown [47]. The UV-vis spectrum also shows P3HT/$PC_{70}BM$–IHJN, P3HT:$PC_{70}BM$–BHJ and P3HT/$PC_{70}BM$–BL films with the infiltrated fullerene material and absorption are observed to be stronger at 490 nm and 380 nm corresponding to the P3HT and $PC_{70}BM$ materials, respectively. P3HT:$PC_{70}BM$–BHJ showed the highest absorption while P3HT/$PC_{70}BM$–BL presented the lowest. This was due to the fact that active layer of BHJ presented a film thickness ~ 200 nm, while the active layer of IHJN and BL were 160 nm and 170 nm approx., respectively. The absorbance peak intensity of P3HT/$PC_{70}BM$–IHJN film was 9% greater than that of P3HT/$PC_{70}BM$–BL film. Moreover, P3HT/$PC_{70}BM$–IHJN showed a considerably higher absorbance (at 600 nm) than that for P3HT:$PC_{70}BM$–BHJ film.

The PL measurements of P3HT–NP in **Fig. 6.7B** show a 16% greater intensity than P3HT–flat film at 695 nm (the measurement conditions are explained in the **Experimental Section**). On the other hand, after PL quenching the intensity of P3HT–NP/$PC_{70}BM$–IHJN film was 94.8% lower than that of pure of P3HT–NP at 695 nm. For P3HT:$PC_{70}BM$–BHJ film and P3HT/$PC_{70}BM$–BL film the PL quenching was observed to be 85.3% and 92.7% that of P3HT–flat film at 695 nm, respectively. The best PL quenching of the three structures was for P3HT/$PC_{70}BM$–IHJN film. The total quenching of PL emission between the interfaces of polymer-fullerene might indicate that there is an efficient photoinduced and charge transfer at the interfaces of P3HT/$PC_{70}BM$ materials. [10, 11] Therefore, on the P3HT–NP nanomorphology the interpillar distance between two nanopillar walls was 40 nm (maximum distance to D/A interface: 20 nm).This geometry may help the excitons to diffuse more easily at the polymer/fullerene composite interface (as

it is well known that the exciton diffusion length is ~10 nm in P3HT [16, 17]), which improves the performance parameters of the cells.

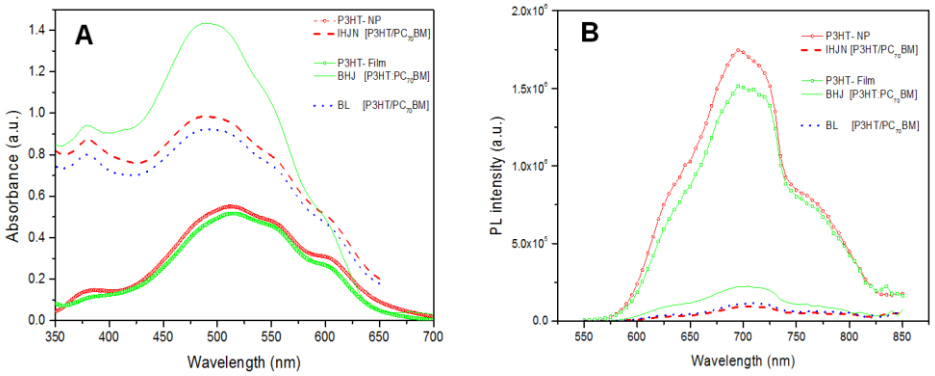

Fig. 6.7 (A) UV/Visible absorbance of P3HT nanopillars (red open circles) and P3HT–film (green open square). The absorbance spectrum of IHJN–[P3HT/$PC_{70}BM$] (red dashed line), BHJ–[P3HT:$PC_{70}BM$] (green continuous line) and BL–[P3HT/$PC_{70}BM$] (blue dotted line is also shown). (B) Photoluminescence spectra were obtained from P3HT nanopillars (red open circles) and P3HT– film (green open squares). Also shown is the PL spectrum from IHJN–[P3HT/$PC_{70}BM$] (red dashed line), BHJ–[P3HT:$PC_{70}BM$] (green continuous line) and BL–[P3HT/$PC_{70}BM$] (blue dotted line). The excitation wavelength was applied at 510 nm.

By integrating the area below the PL spectra the electron injection yield from P3HT to $PC_{70}BM$ can be estimated. In P3HT/$PC_{70}BM$–IHJN film, P3HT:$PC_{70}BM$–BHJ film and P3HT/$PC_{70}BM$–BL film these yields were 95%, 86% and 92%, respectively.

6.3.4. J-V and IPCE characterization

Fig. 6.8A shows the current–voltage (J–V) characteristics of P3HT/$PC_{70}BM$–IHJN imprinted solar cells in comparison to P3HT:$PC_{70}BM$–BHJ and P3HT/$PC_{70}BM$–BL controls OSC under solar illumination at 1 sun (100 mW/cm^2).

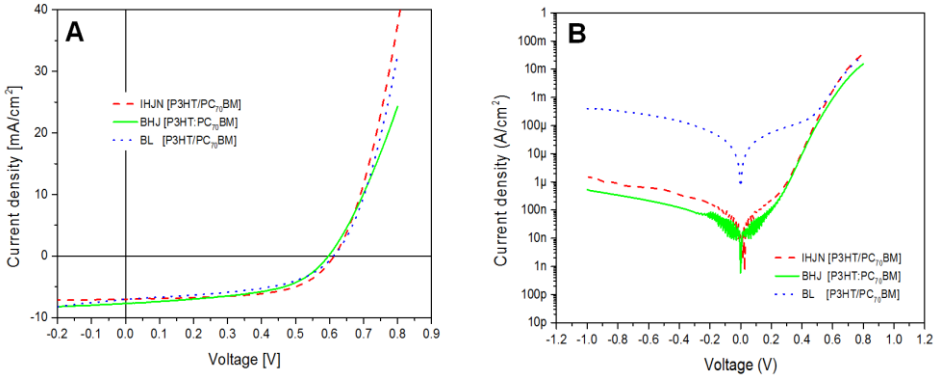

Fig. 6.8 (A) J–V curves to IHJN–OSC (red dashed line), BHJ–OSC (green continuous line) and BL–OSC (blue dotted line) under light (1 sun = 100 mW/cm^2). (B) Semi-log J–V curve under darkness for the three structures.

Fig. 6.9 compares the incident photon to current efficiency (IPCE) spectra for the devices with P3HT/$PC_{70}BM$–IHJN, P3HT:$PC_{70}BM$–BHJ and P3HT/$PC_{70}BM$–BL OSC. For each structure there is a strong correlation of the D/A interface area with IPCE and power conversion efficiency (PCE), short circuit current density (J_{SC}) and fill factor (FF).

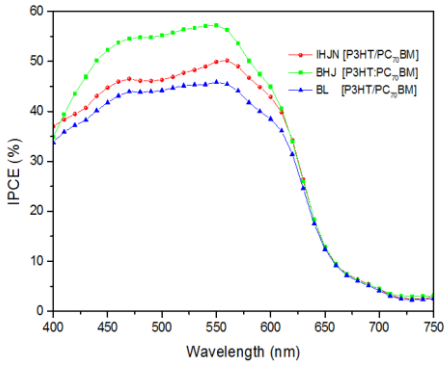

Fig. 6.9 IPCE spectrum of IHJN–OSC, BHJ–OSC and BL–OSC.

Table 6.3 summarizes the best and average performance parameters (i.e. open circuit voltage (V_{OC}), J_{SC}, FF and PCE) of IHJN–OSC (twenty

devices), BHJ–OSC (fifteen devices) and BL–OSC (fifteen devices) after fabrication. The best results of the three structures were analyzed. It is evident that the trend of the IPCE spectra is identical to that of absorption spectra throughout the range but particularly between 400 nm and 700 nm. The IPCE of P3HT/$PC_{70}BM$–IHJN, P3HT:$PC_{70}BM$–BHJ and P3HT/$PC_{70}BM$–BL organic solar cells at 550 nm were 50%, 57% and 45%, and with the integrating J_{SC} they were of 6.99 mA/cm^2, 7.67 mA/cm^2 and 6.7 mA/cm^2, respectively which are strongly supported by J–V characteristics.

	P3HT / $PC_{70}BM$	V_{OC}[a] (mV)	J_{SC}[b] (mA/cm^2)	FF[c] (%)	PCE[d] (%)	$R_{S0\text{-}il}$[e] (Ω-cm^2)	$R_{SH0\text{-}il}$[f] ($k\Omega$-cm^2)	$R_{S0\text{-}dk}$[g] (Ω-cm^2)	$R_{SH0\text{-}dk}$[h] ($k\Omega$-cm^2)
A	IHJN-OSC	613±10	6.4±0.5	53.2±5.6	2.3±0.2	2.58±0.41	0.19±0.06	3.06±0.44	1821.07±1093.95
B	IHJN-OSC Best	630	7.1	61.3	2.6	2.00	0.26	2.18	603.09
C	BHJ-OSC	594±2	6.8±0.4	50.1±1.2	2.0±0.2	7.71±1.01	0.31±0.02	11.37±2.54	2067.50±634.63
D	BHJ-OSC Best	598	7.7	51.4	2.4	6.62	0.33	8.72	2580.01
E	BL-OSC	569±41	6.5±0.4	43.2±5.1	1.6±0.4	2.93±0.44	0.17±0.04	3.22±0.35	2.11±1.47
F	BL-OSC Best	612	6.8	49.0	2.1	2.43	0.21	2.56	3.60

Table 6.3. [a] Open circuit voltage. [b] Short circuit current. [c] Fill factor. [d] Power conversion efficiency. The illumination intensity equivalent applied was 100 m*W*/cm^2 after spectral mismatch correction using AM 1.5G solar simulator. [e] Series resistance per unit area under illumination. [f] Shunt resistance per unit area under illumination. [g] Series resistance per unit area under dark. [h] Shunt resistance per unit area under dark.

IHJN–OSC, BHJ–OSC and BL–OSC showed a PCE of 2.6%, 2.4% and 2.1%, respectively. The V_{OC}, FF and PCE of the IHJN–OSC were 3.5%, 19.3% and 8.3% higher than BHJ–OSC, respectively. On the other hand, the J_{SC} of IHJN–OSC was 7.8% less than that of BHJ–OSC. The PCE of the BHJ–OSCs was a little less than that of IHJN–OSC because the active layer was thicker, so that it could be compared with the others. Moreover, the V_{OC}, J_{SC}, FF and PCE of the IHJN–OSC were 1%, 5%, 23% and 24% higher than BL–OSC, respectively.

In this study, we have observed that the enhancement in the PCE of IHJN–OSC was principally originated by the improvements in FF. While that the FF for BHJ–OSC and BL–OSC were low the values.

The increase in the performance yield of the Jsc of IHJN–OSC we can argue for two aspects: First, it was attributed to the well-controlled interdigitated heterojunction morphology of both materials (P3HT–NP and $PC_{70}BM$) which increased their interfacial area and the contact between them, and made the exciton dissociation more efficient (to get free electrons and holes). Then, the electrons and holes travel through their respective materials to be collected in the metal contact. [12, 14] Second, another reason for the increase in J_{SC} is that the π-π stacking in the P3HT polymer is better oriented and the crystals better formed throughout the nanopillar. This is due to the induction that the polymer undergoes when it is introduced into the nanopore of the template during the soft imprinting step. Therefore, the charge carriers (holes) will move through the P3HT structure and the nanopillar with less difficulty. [22] The improvement of the crystallinity which favors the charge-mobility of holes and the charge transport along the P3HT–NP pathways and reduces the recombination of charge carriers on the pathways. This hypothesis was confirmed by analyzing the orientations of the nanopillar morphology of molecular P3HT with micro-X-ray diffraction. [24] It should be point out that although the absolute thickness of IHJN–OSC was 10 nm less than that BL–OSC the J_{SC} was slightly greater. Moreover, the J_{SC} in the P3HT:$PC_{70}BM$–BHJ solar cell was highest because the active layer was thicker and so able to absorb more photons. [10]

The increase of superficial area of the P3HT–NP layer with respect to the P3HT flat film is known as the interface enhancement factor (IEF) which was calculated by applying the **Eq**. **1** [9, 11, 22]:

$$IEF = \frac{2\pi r_{pillar} H_{pillar} + S_o^2}{S_o^2} \quad (1)$$

where r_{pillar} is the radius of the nanopillar, H_{pillar} is the height of the nanopillar and S_o is the distance between adjacent nanopillars (also called the nanopillar pitch). The P3HT–NP layer had an IEF of 2.5, which means that the surface area increased with respect to that of the P3HT–flat film.

FF was highest for IHJN–OSC (~61.3%) in comparison with BHJ–OSC (~51.4%) and BL–OSC (~49.0%). This increase in FF for IHJN–OSC can be attributed to the nanoimprinted pattern – in which the interface area between the polymer/fullerene material was greater –, the good quality of the cathode-fullerene and anode-polymer interfaces and the decrease in the series resistance (R_S) in the interdigitated heterojunction nanomorphology, all of which suggests that the charge transport properties are substantially improved, as has been observed in [8, 40, 41].

Fig. 8B shows the J–V characteristic in dark conditions for the three organic solar cells. It is well known that R_S can be related to the resistance and thickness of the active layer, the contact resistance between the metal and active layers, the transport properties of the semiconductor material and the properties of the selective contacts. Its value per unit area, R_{S0}, can be calculated by the inversed slope of the J–V curve at the highest operating voltage where the curve becomes linear: $R_{S0} = (J/V)^{-1}$, as has been reported in [48]. In this study, the series resistances $R_{S0\text{-}il}$ and $R_{S0\text{-}dk}$ were obtained from the J–V characteristic under illumination and darkness, respectively, and the values for each organic solar cell structure are shown in **Table 6.3**. In general, $R_{S0\text{-}il}$ and $R_{S0\text{-}dk}$ on IHJN–OSC presented the best values, in which where 70% and 75% lower than for BHJ–OSC and 18% and 15% lower than for BL–OSC, respectively.

The shunt resistance, R_{SH}, which is related to the recombination of charge carriers near the dissociation site (e.g. the donor/acceptor interface of the interdigitated organic materials P3HT–NP/$PC_{70}BM$ in this case) also depends on the transport properties of the semiconductor. The value of shunt resistance per unit area, R_{SH0}, can be determined by calculating the inverse slope around 0 V of the J–V curve, $R_{SH0} = (J / V)^{-1}$. In the dark, this parallel shunt resistance is expected to reflect the intrinsic conductivity of the materials. Under illumination, light induced charge generation (photodoping), caused by the charge transfer between the donor and the acceptor, is expected to reduce the shunt dramatically as was observed in our results. [49] In this study, the shunt resistances $R_{SH0\text{-}il}$ and $R_{SH0\text{-}dk}$ were obtained from the J–V characteristic under illumination and darkness, respectively and their values are shown in **Table 6.3**. Continuing with the analysis, in general, the $R_{SH0\text{-}il}$ and $R_{SH0\text{-}dk}$ of IHJN–OSC were 21% and 76% lower than those of BHJ–OSC, but were 1.23 times and 167 times higher than those of BL–OSC, respectively.

The V_{OC} of IHJN–OSC was 3.5% and 1.1% greater than that of BHJ–OSC and BL–OSC, respectively. The improvement in V_{OC} with respect to the blend devices might be attributed to a reduction in shunt losses, because the wetting layers were correctly arranged in the imprinted devices as reported [10]. It is also reported in the literature that V_{OC} can be attributed to differences in electrical contact work functions and to the difference between the HOMO of the donor and the LUMO of the acceptor. [3, 19] However, when there are recombination losses, the real V_{OC} value depends on the inverse saturation current of the junction in the dark. [49] The V_{OC} value for the IHJN and BL organic solar cells are almost identical. On the other hand, the V_{OC} value for the BHJ-OSC is 6% less than for the IHJN and BL organic solar cells at 1 sun. This must be because in the IHJN and BL cells, the PEDOT:PSS selective electrode is only in contact with the donor material while the calcium selective electrode

is in contact with the acceptor material. The donor and acceptor materials of the BHJ cells, however, are in close contact at the same time with both selective contacts.

Table 6.4 summarizes the method for fabricating nanostructured organic solar cells and compares their geometric characteristics reported in literature with our results.

	polymer-fullerene	morphology array	type of template used[a]	solvent [b]	method of manufacture donor- acceptor[c]	feature size W or ϕ, H, S (nm)[d]	A/A_0 (nm^2)[e]	R-L (nm) [f]	ref.
A	P3HT / C60	Rod	NAAT	-	MW / EV	50, 150, 100	3.3	30	[11]
B	P3HT / PCBM	Rod	NAAT	CH_2Cl_2	NI / SC	50, 80, 100	2.2	20	[9]
C	P3HT / PCBM	Dot	Silicon	$CHCl_3$	SANIL / SC-SANIL	25, 80, 50	3.5	10	[10]
D	P3HT / PCBM	Rod	Silicon	CH_2Cl_2	NI / SC	80, 60, 100	2.5	-	[12]
E	P3HT / PCBM	Nanograting	Silicon	CH_2Cl_2	SANIL / SC	137, 56, 360	1.2	-	[13]
F	P3HT / PCBM	Nanopillar	NAAT	CH_2Cl_2	NI / SC	30, 180, 90	3.0	-	[14]
G	P3HT / PCBM	Nanopillar	-	CH_2Cl_2	EBL / SC	50, 60, 200	1.2	25	[15]
*	P3HT / $PC_{70}BM$	Nanopillar	NAAT	C_7H_8O	NI / SC	60, 80, 100	2.5	40	-

Table 6.4. Summary of the method for fabricating nanostructured organic solar cells and their geometric characteristics reported in literature. [a] Open circuit voltage. [b] Solvents used to dissolve the fullerene material: CH_2Cl_2 is dichloromethane, $CHCl_3$ is chloroform, and C_7H_8O is anisole. [c] MW is melt welting, EV is evaporation, NI is nanoimprinting, SC is spin coating, SANIL is solvent assisted nanoimprint lithography, EBL is electron-beam lithography. [d] W is the width of nanograting morphology and ϕ is the diameter for dot, rod and nanopillar morpholgy, H is the height and S is the distance between adjacent nanopillars (also called the nanopillar pitch). [e] A/A0 is the D/A ratio of the interface areas of the patterned to the planar-interface photovoltaic devices calculated using eq. (1). [f] Residual layer that is under the nanostructure. * Results from this contribution.

Likewise, **Table 6.5** summarizes the performance parameters of the structures shown in **Table 6.4**. It is worth noting that our IHJN–OSC is one of

the first to be manufactured by spin coating using $PC_{70}BM$ and anisole solvent and deposited on P3HT–NP. Another characteristic was the use of Ca and Ag as the cathode for collecting the charge carriers, about which no reports have been published to date. The fill factor obtained here of 61.3% is higher than all others report in the literature. The PCE of IHJN–OSC was 2.6%, which is comparable with such other standard methods and technologies as standard NIL mold, NAAT and double imprinting. The manufacturing method presented here using orthogonal solvent with the fullerene $PC_{70}BM$ is a simpler low-cost method, and facilitates deposit by spin coating. However, cells need to be optimized if performance is to be improved using this technology.

	Device structure	V_{oc}[a] [mV]	J_{sc}[b] [mA/cm^2]	FF[c] [%]	PCE[d] [%]	ref.
A	ITO / PEDOT:PSS / P3HT nanorods / C60 (200nm) / LiF (0.6nm) / Al (150nm)	510	4.7	46.0	1.12	[11]
B	ITO / PEDOT:PSS / P3HT nanorods / PCBM(70 nm) / LiF (0.7nm) / Al (80nm)	570	0.1	56.0	0.05	[9]
C	ITO / PEDOT:PSS / P3HT nanodots / PCBM (80nm) / Al (80nm)	640	8.6	56.0	3.25	[10]
D	ITO / PEDOT:PSS / P3HT nanorods / PCBM (70 nm) / Al (100nm)	570	11.3	40.0	2.57	[12]
E	ITO / PEDOT:PSS / P3HT nanograting / PCBM (69 nm) / Al (100nm)	582	7.6	58.0	2.59	[13]
F	ITO / PEDOT:PSS / P3HT nanopillars / PCBM (? nm) / Al (100nm)	600	7.4	53.0	2.40	[14]
G	ITO / PEDOT:PSS / P3HT nanopillars / PCBM (40 nm) / Al (100nm)	600	1.7	40.0	0.43	[15]
*	ITO / PEDOT:PSS / P3HT nanopillars / $PC_{70}BM$ (40 nm) / Ca (20nm) / Ag (100nm)	630	7.1	61.3	2.60	-

Table 6.5. Summary of the performance of nanostructured photovoltaic devices reported in the literature. [a] Open circuit voltage. [b] Short circuit current. [c] Fill factor. [d] Power conversion efficiency. The illumination intensity equivalent applied was at 100 mW/cm^2 after spectral mismatch correction using AM 1.5G solar simulator. * Results from this contribution.

6.3.5. CE and TPV characterization

In the second part of this study, the IHJN–OSC was analyzed using CE and TPV to show that at open circuit voltage the P3HT/$PC_{70}BM$–IHJN photovoltaic devices are primarily controlled by bimolecular recombination. The two types of control cells manufactured were also analyzed by CE and TPV for purposes comparison.

Fig. 6.10A shows typical CE transients for the devices at 1 sun and in V_{OC} conditions, an extraction half-time of ~2 μs for BHJ–OSC as reported in the literature. [39] For IHJN–OSC and BL–OSC, on the other hand, the half-time was ~6 μs approx. CE was used to measure the average charge carrier density (*n*) in the device at various white light intensities while holding the device at V_{OC} and after switching off the light. The light intensities go from dark to 1 sun. These measurements of *n* against voltage are shown in **Fig. 6.10B**. Note that this experiment collects charges stored in both the photoactive layer and the electrodes. The extracted charge *n* at 1 sun on IHJN–OSC, BHJ–OSC and BL–OSC with V_{OC} was ~630 mV, 598 mV and 612 mV where *n* values were 5.5 $x10^{16}$ cm^{-3}, 1.3 $x10^{17}$ cm^{-3} and 3.8 $x10^{16}$ cm^{-3}, respectively. These values have a stronger correlation with the J_{SC} of the J–V characteristic obtained for each structure analyzed. As have been explained before [39], the charge carrier density in BHJ-OSC manufactured with P3HT:$PC_{70}BM$ can be produced in the bulk of the active layer and at the selective electrodes of the device. Generally, the volumetric charge density in the P3HT:fullerene active layer is more predominant than at the selective electrodes, as was observed in this study.

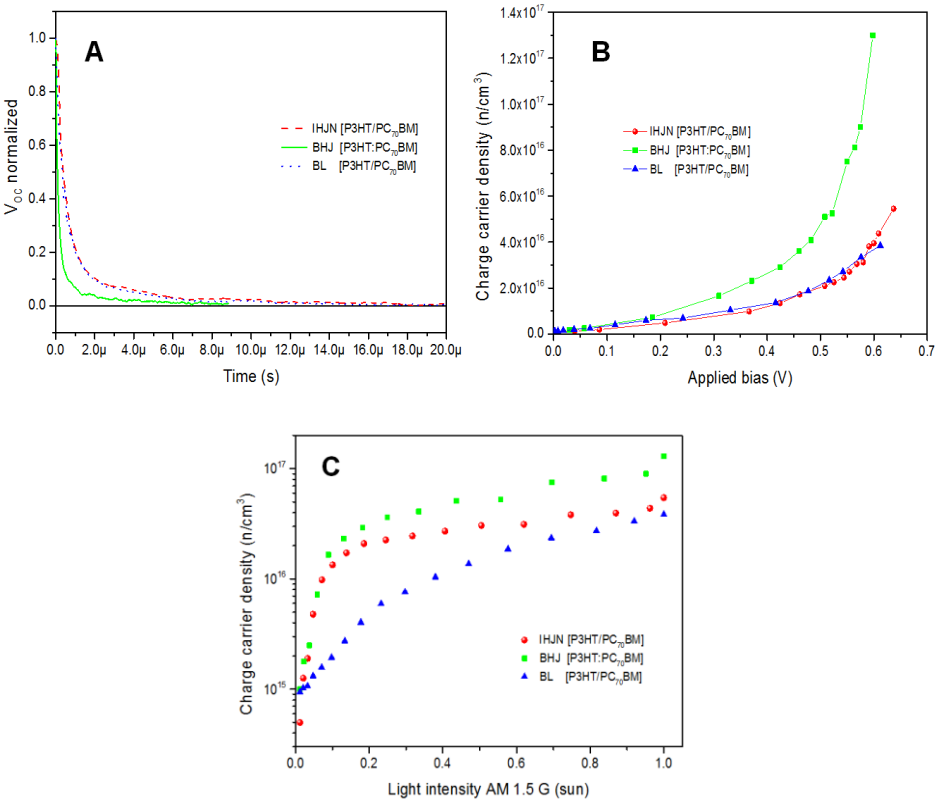

Fig. 6.10 (A) CE transient acquired to compare IHJN–OSC, BHJ–OSC and BL–OSC under 1 sun steady state background irradiation. For the CE transient, the background irradiation was turned off rapidly, and the device simultaneously switched from open to short circuit. (B) Charge carrier density (*n*) as a function of the applied bias (the maximum point of each curve is 1 sun of light incident on the PV structure during the measurement). In the IHJN–OSC, BHJ–OSC and BL–OSC the charge carrier density undergoes an exponential increase. (C) Log n–light intensity, variation in charge carrier density measured under different light intensities for each structure manufactured.

Our devices with the structure BHJ–OSC, IHJN–OSC and BL–OSC seem to have the same predominant charge accumulation dynamics. [39, 42, 43, 48] **Fig. 6.10B** shows that the charge carrier density in open circuit conditions

for different light intensities exponentially depends on the V_{OC} obtained by changing the light intensity according to the following formula [40]

$$n = n_0 e^{\gamma voc} \quad (2)$$

n_0 is the initial charge carrier and γ is a factor related to the presence of energetic disorder in the intrinsic properties of the semiconductor materials. The values of $\gamma < 19$ V^{-1} when $p \approx n$, or $\gamma \sim 38$ V^{-1} when n>>p or p>>n. Eq. (2) was applied to IHJN–OSC, BHJ–OSC and BL–OSC. n_0 and γ presented values for IHJN–OSC, BHJ–OSC and BL–OSC of 3.58 x 10^{14} cm^{-3} and 9.73 V^{-1}, 4.63 x 10^{14} cm^{-3} and 7.42 V^{-1} and 1.52 x 10^{15} cm^{-3} and 5.29 V^{-1}, respectively. The γ values obtained in this study are similar to the ones obtained in others an in all cases they are less than half of the value expected for an ideal band-gap. [41, 42] This suggests that gamma values present a non-ideal behavior and is due to the presence of an exponential tail of density of trap states extending into the band-gap of the photoactive layer. In other words these traps correspond to the presence of energetic disorder in the active layer, which influences the transport and recombination processes. [40, 50] So, we suggest that the structure with most energetic disorder in the active layer was BL–OSC and the structure with the least was IHJN–OSC. BHJ–OSC presented disorder values in the active layer that were between the other two because the high values of R_{S0} were caused by the thick active layer.

The TPV measurements were performed on BHJ–OSC, IHJN–OSC and BL–OSC. The charge carrier density obtained from CE measurements for different light intensities (from 0.3 to 1.0 sun) was used to get the carrier lifetime from TPV measurements. The decay dynamics for all devices agrees with previous measurements on P3HT:PCBM blends: namely, that single-exponential fits apply for a wide range of illumination intensities. [40-43, 48, 51, 52] **Fig. 6.11A** shows carrier lifetimes as a function of carrier density for

varying illumination intensities. At one sun, the IHJN–OSC, BHJ–OSC and BL–OSC have carrier lifetimes of ~3.9 μs, ~5.8 μs and 4.2 μs, respectively. The recombination lifetime decreases when the light intensity is increasing until achieve to 1 sun and the charge carriers are also increasing.

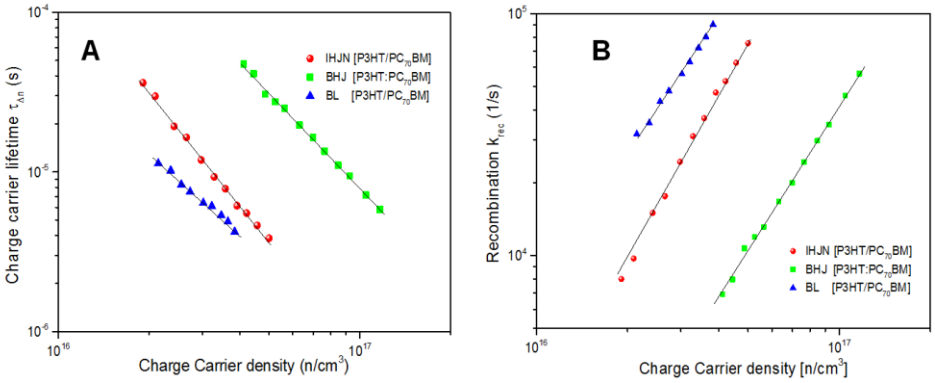

Fig. 6.11 (A) TPV measurements were performed under open circuit conditions and different illumination (V_{OC}) for IHJN–OSC, BHJ–OSC and BL–OSC structures. (B) Bimolecular recombination rate constant k_{rec}, extracted from carrier τ and *n*, as a function of *n*. The pulse excitation wavelength was 470 nm. The pulsed source power was set so that the ΔV of the TPV measurement did not exceed 3% of the V_{OC} measured at 0.1 sun.

The charge density has an inverse square relationship with the recombination lifetime (Eq. 3) with $\beta/\gamma = \lambda$. IHJN–OSC, BHJ–OSC and BL–OSC show λ values of 2.4, 2 and 1.8, respectively.

$$\tau_{\Delta n} = \tau_{n0} (n_0/n)^{\lambda} \qquad (3)$$

All the values of λ indicate there are bimolecular recombinations as similar values were reported in the literature. [41, 43, 48] **Fig. 6.11B** shows the bimolecular recombination rate constants k_{rec} and were calculated from the carrier lifetimes and densities according to the following equation [39]:

$$k_{rec} = 1/(\lambda+1)\, \tau_{\Delta n} \qquad (4)$$

The devices with the lowest bimolecular recombination rate were BHJ–OSC. Reduced recombination constants are considered critical for efficient solar cells. BHJ–OSC had the longest carrier lifetimes and smallest k_{rec} values whereas BL–OSC had the shortest carrier lifetimes and largest $k_{rec.}$ IHJN–OSC presented values in between (see **Fig. 6.11B**).

All the electrical characterization used in this study provides insight into the working mechanisms of the various organic solar cells that were fabricated and analyzed. The critical parameter(s) required to improve the synthesis, design and fabrication on interdigitated organic solar cells and enhance the performance parameters have been identified.

6.4. Conclusions

In this chapter IHJN–OSC were manufactured by soft nanoimprinting in combination with nanoporous anodic alumina templates to produce P3HT–NP and they were filled by spin coating of $PC_{70}BM$ on the top of NP in combination with anisole orthogonal solvent. The fabrication method, using this orthogonal solvent, on IHJN–OSC has been reported for the first time. The P3HT–NP presented good replication and a well-ordered array of NAAT with an average diameter of 60 nm, pillar height of 80 nm and interpillar distance of 100 nm. IHJN–OSC was compared with BHJ–OSC and BL-OSC as controls and they were fabricated under the same conditions. The surface area of the P3HT–NP theoretically increased 2.5 times more than that of BL-OSC. Current–voltage characteristics and optical measurement were applied for all photovoltaic devices. The results provide direct evidence that the imprinting layer gives FF ~ 61.3% and PCE ~2.6%. This due to the larger interface between the donor and acceptor materials, resulting in more efficient

photogeneration, exciton dissociation and charge transport on extended interfaces made up of a finely controlled morphology. CE and TPV measurement were applied on IHJN–OSC. Bimolecular recombination was found to be the main mechanism by which charge carriers were lost. For the interdigitated the recombination losses were lower than for BL–OSC. The gamma values for the IHJN–OSC, presented an exponential tail of density of trap states that extended into the band-gap of the photoactive layer. These values were lower for IHJN–OSC than for BHJ–OSC and BL–OSC. In other words, the structure with the lowest energetic disorder in the active layer was IHJN–OSC where the recombination process is reduced. The study of the three structures at the same time provides important information about how such physical properties as the charge density, charge carrier lifetime and mechanism are governed inside the device.

We conclude that interdigitated morphology has a favorable influence on photogeneration and charge transport but they also depend on factors such as the quality of the materials, the fabrication process (e.g. the use of orthogonal solvents, quality of materials, etc.), technology and even how the solar cells are characterized. The use of orthogonal solvents to fabricate solar cells offers a simple, potentially low-cost fabrication route and opens up new possibilities for using new polymers for manufacturing interdigitated OSC.

6.5. References

[1] C.J. Brabec, Organic photovoltaics: technology and market, *Sol. Energy Mater. Sol. Cells, 83* (2004) 273−292.

[2] V.S. Balderrama, M. Estrada, A. Viterisi, P. Formentin, J. Pallarés, J. Ferré-Borrull, E. Palomares, L.F. Marsal, Correlation between P3HT inter-chain structure and Jsc of P3HT:$PC_{70}BM$ blends for solar cells, *Microelectron. Reliab., 53* (2013) 560−564.

[3] J.-T. Chen, C.-S. Hsu, Conjugated polymer nanostructures for organic solar cell applications, *Polym. Chem., 2* (2011) 2707−2722.

[4] J. Jo, S.-I. Na, S.-S. Kim, T.-W. Lee, Y. Chung, S.-J. Kang, D. Vak, D.-Y. Kim, Three-Dimensional Bulk Heterojunction Morphology for Achieving High Internal Quantum Efficiency in Polymer Solar Cells, *Adv. Funct. Mater., 19* (2009) 2398−2406.

[5] W. Ma, C. Yang, X. Gong, K. Lee, A.J. Heeger, Thermally Stable, Efficient Polymer Solar Cells with Nanoscale Control of the Interpenetrating Network Morphology, *Adv. Funct. Mater., 15* (2005) 1617−1622.

[6] K. Sivula, Z.T. Ball, N. Watanabe, J.M.J. Fréchet, Amphiphilic Diblock Copolymer Compatibilizers and Their Effect on the Morphology and Performance of Polythiophene:Fullerene Solar Cells, *Adv. Mater., 18* (2006) 206−210.

[7] J. Weickert, R.B. Dunbar, H.C. Hesse, W. Wiedemann, L. Schmidt-Mende, Nanostructured Organic and Hybrid Solar Cells, *Adv. Mater., 23* (2011) 1810−1828.

[8] X. Li, W.C.H. Choy, L. Huo, F. Xie, W.E.I. Sha, B. Ding, X. Guo, Y. Li, J. Hou, J. You, Y. Yang, Dual plasmonic nanostructures for high performance inverted organic solar cells, *Adv. Funct. Mater., 24* (2012) 3046−3052.

[9] W. Wiedemann, L. Sims, A. Abdellah, A. Exner, R. Meier, K.P. Musselman, J.L. MacManus-Driscoll, P. Müller-Buschabaum, G. Scarpa, P. Lugli, L. Schmidt-Mende, Nanostructured interfaces in polymer solar cells, *Appl. Phys. Lett., 96* (2010) 263109.

[10] X. He, F. Gao, G. Tu, D.G. Hasko, S. Hüttner, N.C. Greenham, U. Steiner, R.H. Friend, W.T.S. Huck, Formation of Well-Ordered Heterojunctions in Polymer:PCBM Photovoltaic Devices, *Adv. Funct. Mater., 21* (2011) 139−146.

[11] J.S. Kim, Y. Park, D.Y. Lee, J.H. Lee, J.H. Park, J.K. Kim, K. Cho, Poly(3-hexylthiophene) Nanorods with Aligned Chain Orientation for Organic Photovoltaics, *Adv. Funct. Mater., 20* (2010) 540−545.

[12] M. Aryal, F. Buyukserin, Imprinted large-scale high density polymer nanopillars for organic solar cells, *J. Vac. Sci. Technol. B, 26* (2008) 2562−2566.

[13] J.Y. Park, N.R. Hendricks, K.R. Carter, Solvent-assisted soft nanoimprint lithography for structured bilayer heterojunction organic solar cells, *Langmuir, 27* (2011) 11251−11258.

[14] D. Chen, W. Zhao, T.P. Russell, P3HT Nanopillars for Organic Photovoltaic Devices Nanoimprinted by AAO Templates, *ACS Nano, 6* (2012) 1479−1485.

[15] S. Moungthai, N. Mahadevapuram, P. Ruchhoeft, G.E. Stein, Direct Patterning of Conductive Polymer Domains for Photovoltaic Devices, ACS Appl. Mater. *Interfaces, 4* (2012) 4015−4023.

[16] C.W. Tang, S.A. Vanslyke, Organic electroluminescent diodes in: *Appl. Phys. Lett.,* (1987) 913−915.

[17] J. Slota, X. Hea, W.T.S. Huck, Controlling nanoscale morphology in polymer photovoltaic devices, *Nano Today, 5* (2010) 231−241.

[18] K.M. Coakley, Y. Liu, C. Goh, M.D. McGehee, Ordered Organic–Inorganic Bulk Heterojunction Photovoltaic Cells, *MRS Bull, 30* (2005) 37−40.

[19] C.J. Brabec, N.S. Sariciftci, J.C. Hummelen, Plastic Solar Cells, *Adv. Funct. Mater., 11* (2001) 15−26.

[20] H. Hoppe, N.S. Sariciftci, Morphology of polymer/fullerene bulk heterojunction solar cells, *J. Mater. Chem., 16* (2006) 45−61.

[21] V.S. Balderrama, M. Estrada, A. Cerdeira, B.S. Soto-Cruz, L.F. Marsal, J. Pallares, J.C. Nolasco, B. Iñiguez, E. Palomares, J. Albero, Influence of P3HT:PCBM blend preparation on the active layer morphology and cell degradation, *Microelectron. Reliab., 51* (2011) 597−601.

[22] Y. Yang, K. Mielczarek, M. Aryal, A. Zakhidov, W. Hu, Nanoimprinted Polymer Solar Cell, *ACS Nano, 6* (2012) 2877−2892.

[23] Y. Liu, C. Kirsch, A. Gadisa, M. Aryal, S. Mitran, E.T. Samulski, R. Lopez, Effects of nano-patterned versus simple flat active layers in upright organic photovoltaic devices, *J. Phys. D: Appl. Phys., 46* (2013) 024008.

[24] A. Santos, P. Formentín, J. Pallarés, J. Ferré-Borrull, L.F. Marsal, Fabrication and characterization of high-density arrays of P3HT

nanopillars on ITO/glass substrates, *Sol. Energy Mater. Sol. Cells, 94* (2010) 1247−1253.

[25] J.H. Lee, D.W. Kim, H. Jang, J.K. Choi, J. Geng, J.W. Jung, S.C. Yoon, H.-T. Jung, Enhanced Solar-Cell Efficiency in Bulk-Heterojunction Polymer Systems Obtained by Nanoimprinting with Commercially Available AAO Membrane Filters, *Small, 5* (2009) 2139−2143.

[26] M. Aryal, K. Trivedi, W. Hu, Nano-confinement induced chain alignment in ordered P3HT nanostructures defined by nanoimprint lithography, *ACS Nano, 3* (2009) 3085−3090.

[27] A. Greiner, J.H. Wendorff, Electrospinning: A Fascinating Method for the Preparation of Ultrathin Fibers, *Angew. Chem. Int. Ed., 46* (2007) 5670−5703.

[28] F.C. Krebs, Fabrication and processing of polymer solar cells: A review of printing and coating techniques, *Sol. Energy Mater. Sol. Cells, 93* (2009) 394−412.

[29] N. Haberkorn, J.S. Gutmann, P. Theato, Template-Assisted Fabrication of Free-Standing Nanorod Arrays of a Hole-Conducting Cross-Linked Triphenylamine Derivative: Toward Ordered Bulk-Heterojunction Solar Cells, *ACS Nano, 3* (2009) 1415−1422.

[30] D.-G. Choi, K.-J. Lee, J.-H. Jeong, D.H. Wang, O.O. Park, J.H. Park, Sub-100 nm scale polymer transfer printing process for organic photovoltaic devices, *Sol. Energy Mater. Sol. Cells, 109* (2013) 1–7.

[31] H. Masuda, H. Yamada, M. Satoh, H. Asoh, Highly ordered nanochannel-array architecture in anodic alumina, *Appl. Phys. Lett., 71* (1997) 2770−2772.

[32] A. Santos, P. Formentin, J. Pallarés, J. Ferré-Borrull, L.F. Marsal, Quasi-ordered P3HT nanopillar-nanocap structures with controlled size, *Mater. Lett., 64* (2010) 371−374.

[33] A.P. Li, F. Müller, A. Birner, K. Nielsch, U. Gösele, Hexagonal pore arrays with a 50–420 nm interpore distance formed by self-organization in anodic alumina, *J. Appl. Phys., 84* (1998) 6023−6026.

[34] D. Cheyns, K. Vasseur, C. Rolin, J. Genoe, J. Poortmans, P. Heremens, Nanoimprinted semiconducting polymer films with 50 nm features and their application to organic heterojunction solar cells, *Nanotechnology, 19* (2008) 424016−424021.

[35] G. Yu, J. Gao, J.C. Hummelen, F. Wudl, A.J. Heeger, Polymer Photovoltaic Cells: Enhanced Efficiencies via a Network of Internal Donor-Acceptor Heterojunctions, *Science, 270* (1995) 1789−1791.

[36] I. Mejia, M. Estrada, M. Avila, Improved upper contacts PMMA on P3HT PTFTS using photolithographic processes, *Microelectron. Reliab., 48* (2008) 1795−1799.

[37] M. Estrada, I. Mejia, A. Cerdeira, B. Iñiguez, MIS polymeric structures and OTFTs using PMMA on P3HT layers, *Solid State Electron., 52* (2008) 53−59.

[38] J.S. Jaworski, M. Cembor, M. Orlik, Anisole as a solvent for organic electrochemistry, *J. Electroanal. Chem., 582* (2005) 165−170.

[39] C.G. Shuttle, A. Maurano, R. Hamilton, B. O'Regan, J.C. de Mello, J.R. Durrant, Charge extraction analysis of charge carrier densities in a polythiophene/fullerene solar cell: Analysis of the origin of the device dark current, *Appl. Phys. Lett., 93* (2008).

[40] A. Maurano, C.G. Shuttle, R. Hamilton, A.M. Ballantyne, J. Nelson, W. Zhang, M. Heeney, J.R. Durrant, Transient Optoelectronic Analysis of Charge Carrier Losses in a Selenophene/Fullerene Blend Solar Cell, *J. Phys. Chem. C, 115* (2011) 5947−5957.

[41] J. Albero, Y. Zhou, M. Eck, F. Rauscher, P. Niyamakom, I. Dumsch, S. Allard, U. Scherf, M. Kruger, E. Palomares, Photo-induced charge recombination kinetics in low bandgap PCPDTBT polymer:CdSe quantum dot bulk heterojunction solar cells, *Chem. Sci., 2* (2011) 2396−2401.

[42] A. Maurano, R. Hamilton, C.G. Shuttle, A.M. Ballantyne, J. Nelson, B. O'Regan, W. Zhang, I. McCulloch, H. Azimi, M. Morana, C.J. Brabec, J.R. Durrant, Recombination Dynamics as a Key Determinant of Open Circuit Voltage in Organic Bulk Heterojunction Solar Cells: A Comparison of Four Different Donor Polymers, *Adv. Mater., 22* (2010) 4987−4992.

[43] A. Guerrero, N.F. Montcada, J. Ajuria, I. Etxebarria, R. Pacios, G. Garcia-Belmonte, E. Palomares, Charge carrier transport and contact selectivity limit the operation of PTB7-based organic solar cells of varying active layer thickness, *J. Mater. Chem. A, 1* (2013) 12345−12354.

[44] B.C. O'Regan, J.R. Durrant, Calculation of Activation Energies for Transport and Recombination in Mesoporous TiO2/Dye/Electrolyte FilmsTaking into Account Surface Charge Shifts with Temperature, *J. Phys. Chem. B, 110* (2006) 8544−8547.

[45] F. Zhang, Z. Zhuo, J. Zhang, X. Wang, X. Xu, Z. Wang, Y. Xin, J. Wang, J. Wang, W. Tang, Z. Xu, Y. Wang, Influence of $PC_{60}BM$ or

$PC_{70}BM$ as electron acceptor on the performance of polymer solar cells, *Sol. Energy Mater. Sol. Cells, 97* (2012) 71−77.

[46] F. Padinger, R.S. Rittberger, N.S. Sariciftci, Effects of Postproduction Treatment on Plastic Solar Cells, *Adv. Funct. Mater., 13* (2003) 85-88.

[47] P. Granero, V.S. Balderrama, J. Ferré-Borrull, J. Pallarès, L.F. Marsal, Two-dimensional finite-element modeling of periodical interdigitated full organic solar cells, *J. Appl. Phys., 113* (2013) 043107−043101.

[48] C.G. Shuttle, B. O'Regan, A.M. Ballantyne, J. Nelson, D.D.C. Bradley, J. de Mello, J.R. Durrant, Experimental determination of the rate law for charge carrier decay in a polythiophene: Fullerene solar cell, *Appl. Phys. Lett., 92* (2008).

[49] C. Waldauf, M.C. Scharber, P. Schilinsky, J.A. Hauch, C.J. Brabec, Physics of organic bulk heterojunction devices for photovoltaic applications, *J. Appl. Phys.,* 99 (2006).

[50] C.G. Shuttle, R. Hamilton, J. Nelson, B.C. O'Regan, J.R. Durrant, Measurement of Charge-Density Dependence of Carrier Mobility in an Organic Semiconductor Blend, *Adv. Funct. Mater., 20* (2010) 698−702.

[51] C.G. Shuttle, R. Hamilton, B.C. O'Regan, J. Nelson, J.R. Durrant, Charge-density-based analysis of the current–voltage response of polythiophene/fullerene photovoltaic devices, *Proc. Nat. Acad. Sci., 107* (2010) 16448−16452.

[52] I. Etxebarria, A. Guerrero, J. Albero, G. Garcia-Belmonte, E. Palomares, R. Pacios, Inverted vs standard PTB7:PC70BM organic photovoltaic devices. The benefit of highly selective and extracting contacts in device performance, *Org. Electron., 15* (2014) 2756−2762.

[53] J.W. Krumpfer, T.J. McCarthy, Rediscovering Silicones: Unreactive Silicones React with Inorganic Surfaces, *Langmuir*, *27* (2011) 11514−11519.

Chapter 7

Summary and conclusions

The work presented in this thesis concern the following subjects: fabrication of bulk heterojunction organic solar cells using the P3HT and PTB1 as the p-type donor materials and the $PC_{70}BM$ and PCBM as the n-type acceptor materials. The analysis of degradation process in the photovoltaic devices was carried out, which aspects as the active blend preparations, the morphology control, the annealing process and the environment conditions exposed the organic solar cells were taken. Current-voltage characteristic was used to monitor the performance parameters of the photovoltaic devices during the operation under light and dark conditions. An electrical model was used to correlate the physical mechanisms with the performance parameters of the organic solar cells.

The interdigitated heterojunction organic solar cells were designed, manufactured and characterized to investigate the electrical and optical characteristics and then compared with the bulk heterojunction and bilayer

structures. The charge extraction and transient photovoltage characterizations were used in the photovoltaic devices.

Chapter 3 presents two different blend solutions of P3HT:PCBM at (1:0.8) wt% – blend 1 and (1:1) wt% – blend 2 and theses were deposited to fabricate the organic solar cells. The photovoltaic devices fabricated with the blend 2 after the exposition in air for 72 h, the degradation process becomes more predominant. I-V characteristic obtained under light and dark conditions in the organic solar cells were well fitted with the electrical model proposed. Parameters as saturation current Io, ideality factor *n*, series and shunt resistances R_s, R_{sh} were extracted from the electrical model. The electrical behavior of the device was correlated with the morphology of the active layer and the parameters extracted. The Io values for both photovoltaic structures (blend 1 and blend 2) just after fabrication were the same. Whereas, Io for the devices fabricated with the blend 2 after degradation process, the value is greater of one order of magnitude than devices fabricated with the blend 1. This suggests that the intrinsic properties of the active layer for the devices prepared with the blend 2 are more severely affected by the oxygen and water content in the air.

The electrical model for the I-V curves fit with one and two diodes for the devices fabricated with the blend 2 and the blend 1, respectively. This morphologically was suggested that the devices manufacture with the blend 1 had formed two types of junctions for generating, separating and transporting of the charge carriers. The first junction is due to formation of the heterojunction between the P3HT and PCBM materials; whereas the second diode is by the formation of the metal-semiconductor junction. Then, the ideality factor extracted of the electrical model for the first junction is n=2 which suggests the charge transport mechanism is by recombination and for the second junction is n=1 which the charge transport mechanism is by diffusion. The morphology in the blend 2 was predominant the formation of heterojunctions between the

P3HT and PCBM with n=1 and the charge transport mechanism is the same as was described above. The series resistances in the devices manufactured with the blend 1 were lower than that the devices manufactured with blend 2 after the degradation process in air.

In chapter 4, the P3HT:$PC_{70}BM$ active blends prepare with different amounts of $PC_{70}BM$ to fabricate photovoltaic devices have direct relation with the short circuit current density. When the $PC_{70}BM$ amount in the active layer is increasing, the disorder and interchain distance-spacing d_{100} between two lamellar structures in P3HT polymer is also increasing. In response, there is an increment in the charge carrier recombination inside of the active layer and the short circuit current density is reduced in the device. Test of micro-X-ray diffraction and I-V characteristic confirm the above described. In the experiment with the blend S1 (1:0.5 wt%) shows the highest J_{sc} and with less interchain distance-spacing d_{100} in P3HT of 1.64 nm, condition that helps to have a better transport of charge carriers through by the active layer.

In chapter 5, the organic solar cells prepare with PTB1 polymer of low-band gap in combination with PCBM, the best power conversion efficiency is 5.2%. These photovoltaic devices were exposed under different environments such as air, nitrogen and under encapsulation where the ISOS-D1 protocol was applied. Cells under nitrogen environment the lifetime at (T_{S80}) is 990 hours, in an ambient atmosphere the lifetime is 4 hours, and under encapsulation the lifetime is 48 hours. We have seen that the evolution of the power conversion efficiency can be modelled by the sum of two decaying exponentials with time constants T1 and T2. The values extracted from the model are related with the degradation mechanism predominant, according the environment. The mechanism responsible for the slow degradation in cells under nitrogen environment is identified to be the intrinsic chemical reactions of the polymeric materials with values of T1 = T2 = 4800 h. The solar cells under air conditions,

the time constants of degradation extracted from the model of PCE are T1 = 10 h and T2 = 80 h showing two degradation mechanisms and dominating at different operation time during its life. In these solar cells, the water is the more predominant degradation mechanism. Finally solar cells under encapsulation, the time constants of degradation extracted from model of PCE are T1 = 4800 h and T2 = 80 h showing two degradation mechanisms too. In this case the oxygen is the predominant degradation mechanism for these solar cells. These results show that the procedure followed in this work under ISOS-D1 protocols permit to gain knowledge of the main degradation mechanisms of the PTB1 donor polymer in the solar cells.

Finally in the chapter 6, interdigitated heterojunction nanostructured organic solar cell, IHJN–OSC, are manufactured by soft nanoimprinting method in combination with nanoporous anodic alumina templates to produce P3HT–NP and after by spin coating is deposited the $PC_{70}BM$ on the top of NP in combination with anisole orthogonal solvent. The results provide direct evidence which the imprinting layer gives FF ~ 61.3% and PCE ~2.6%. The nanoimprinting polymer creates larger interface between the donor and acceptor materials, then resulting with more efficient the photogeneration, the exciton dissociation and transport of the charge carriers by all the morphology interdigitated. The charge extraction and transient photovoltage are electrical techniques to quantify the charge density variation over the applied bias in the organic solar cells. For the first time these techniques are applied in IHJN–OSC. Using both techniques, the results reveal that bimolecular recombination is predominant in the dynamic of charge carrier losses for the interdigitated heterojunction organic solar cells. The recombination losses in interdigitated photovoltaic devices have been of 1.2 times lower than bilayer organic solar cells, BL–OSC. According to the results obtain and interpret for the IHJN–OSC has been identified an exponential tail of trap density states extending into the band-gap of the photoactive layer with values lower than that in BHJ–OSC.

This characteristic favors for the transport of charge carriers in IHJN–OSC. In other words, there are fewer traps and as results are obtained the reduction of the presence of energetic disorder inside of the interdigitated active layer and in the recombination processes.

Appendix

Appendix A. Process fabrication of bulk heterojunction solar cells

Appendix A. Process fabrication of bulk heterojunction organic solar cells

The fabrication process of the solar cell is represented in **Fig. A-A1**. Indium tin oxide was bought with the ITO pattern. Acetone, isopropyl, and water are used to clean the substrates. Ultraviolet light is employed to eliminate organic waste. PEDOT:PSS was deposited on the previous clean ITO substrate as was described in chapter 5. Blend solution was prepared under nitrogen conditions. The blend solution takes long time to get good dissolution of the polymer. Then, the blend solution is deposited by spin coating. Finally, it is deposited the metal contact under ultra-high vacuum to obtain the photovoltaic device.

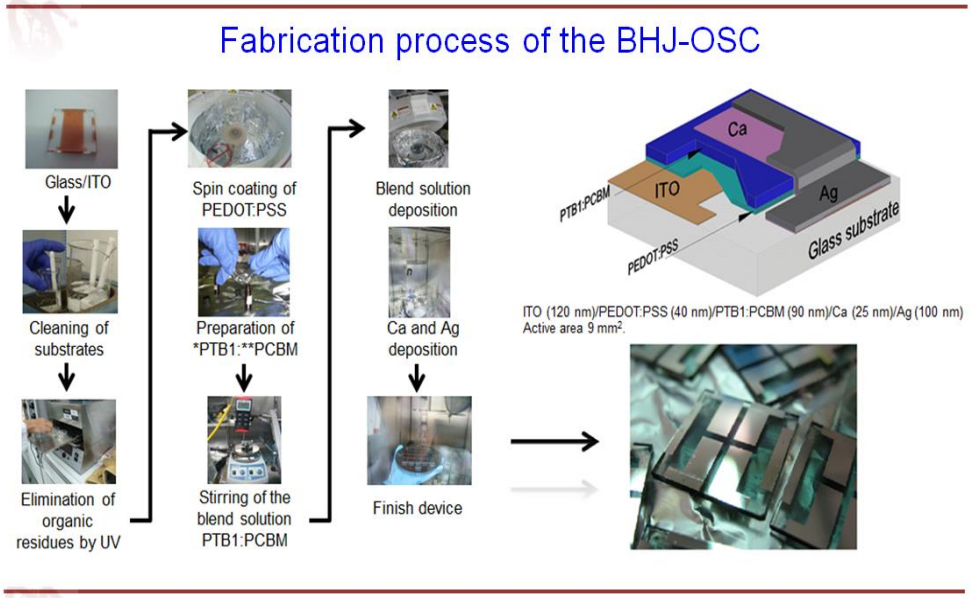

Fig. A-A1 Typical fabrication process used on PTB1:PCBM organic solar cell under nitrogen environment.

Appendix B. ISOS-D1 protocols

ISOS-D1 protocols was applied in PTB1:PCBM solar cells. The conditions and parameters apply in the organic solar cells are to stablish the standard condition when the photovoltaic devices are exposed under different environment. **Fig. B-A2** shows the parameters and conditions to analyse the degradation process over time in the organic solar cells from the experiments of chapter 5.

Aging mode	N_2	Air	Encapsulation
Conditions	Electronic grade 99.999% N_2 H_2O < 0.1 ppm O_2 < 0.1 ppm	Environmental air 60 ± 5% RH	Top glass sealed to the bottom glass with the glue adhesive (EPT-HM)***
Temperature	23 °C	23 °C	23 °C
Stored specimen	Under darkness	Under darkness	Under darkness
Characterization light source	Solar simulator	Solar simulator	Solar simulator
Load	Open circuit	Open circuit	Open circuit

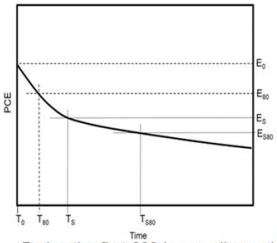

Four pairs of parameters needed to define OPV device stability [1]

Parameters	
E_0, T_0	E_0 is the initial testing measurement after fabrication of the device, at time = 0, T_0.
E_S, T_S	E_S is a second testing measurement, defined arbitrarily by the user as some time T_S.
E_{80}, T_{80}	E_{80} is the testing measurement when is decayed 20% from the initial lifetime. T_{80} is the time it took to decay.
E_{S80}, T_{S80}	E_{S80} is the testing measurement after the device has decayed 20% of its lifetime. T_{S80} is the time it took to decay and is defined arbitrarily by the user as some time.

[1] Sol. Energy Mater. Sol. Cells, 95 (2011) 1253–1267
***EPT-HM = [3-(2,3-Epoxypropoxy)propyl]-trimethoxysilane, hydroxypropyl methacrylate

During the first 288 hours, all sample groups were stored in N_2 at 23 ºC. The photovoltaic solar cells in this period of time did not show any substantial change in their performance parameters. After this time the devices were aged under different conditions.

Fig. B-A2 Protocols applied for the organic solar cells.

Appendix C. ESEM micro-analysis by X-ray

Environmental scanning electron microscope (ESEM FEI Quanta 600) is equipped with an energy dispersive X-ray spectroscope (EDXS). In this microscope, a focused high-energy electrons beam generates a diversity of signals at the sample surface. These signals are derived between the probe electron and the specimen atoms. These electrons reveal information about the sample properties such as the external morphology, chemical and crystal structure. Lithium-drifted silicon (Si (Li)) was used as detector. The energy applied to the sample was 15kV with a working distance of 10 mm. Fig. C-A3 a) shows the ESEM image of the glue material. Afterward, it was analyzed by X-ray. **In Fig. C-A3** b) and c) were showed the chemical analysis and quantification in weight percentage of EPT-HM, respectively. The quantity of carbon, oxygen and silicon were 76.49%, 23.05% and 0.45%, respectively. The hydrogen element was not found due to that the detector has a beryllium window mount in it.

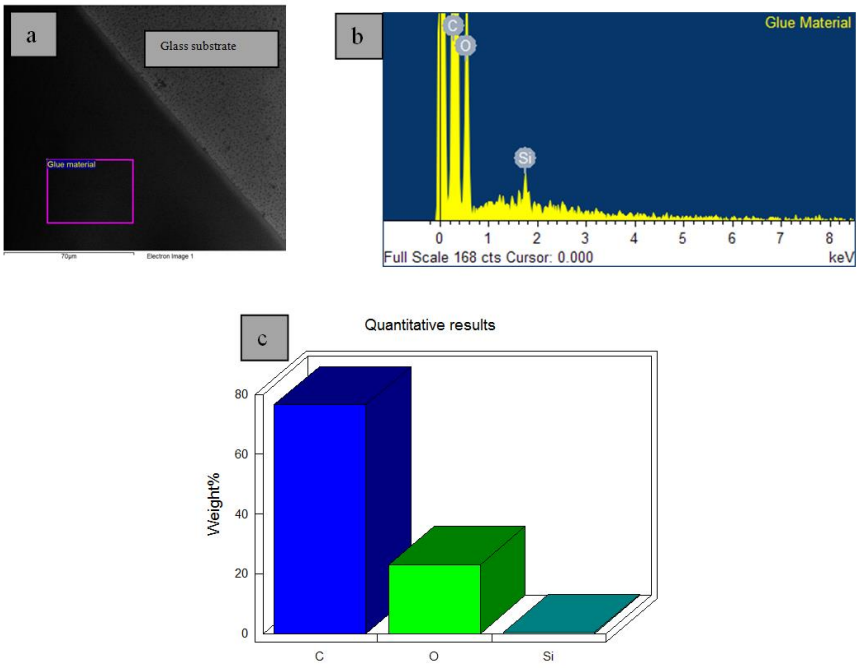

Fig. C-A3 a) ESEM image obtained of EPT-HM material; b) and c) represent the chemical analysis and the quantification in weight percentage of each element found, respectively.

Appendix D. Degradation mechanisms in BHJ organic solar cells

With the tremendous effort over the last few years in achieving higher power conversion efficiencies in organic solar cells, studies on device lifetime and degradation mechanisms shifted more into focus. Only the understanding of these degradation mechanisms can ensure that the stability and lifetime of organic solar cells can be increased to several years.

Up to now investigations often concerned the influence of extrinsic parameters like temperature, light, oxygen and humidity on single active layers, on the interfaces and contacts, or on fully processed solar cells. **Fig. D-A4** presents several degradation mechanisms which are reported in the literature. However, fewer publications deal with intrinsic degradation mechanisms arising from the materials used to produce solar cells. Additionally the interfaces between materials can also be a bottle neck for improving device lifetime, but it is generally difficult to localize and characterize stability issues in complete devices.

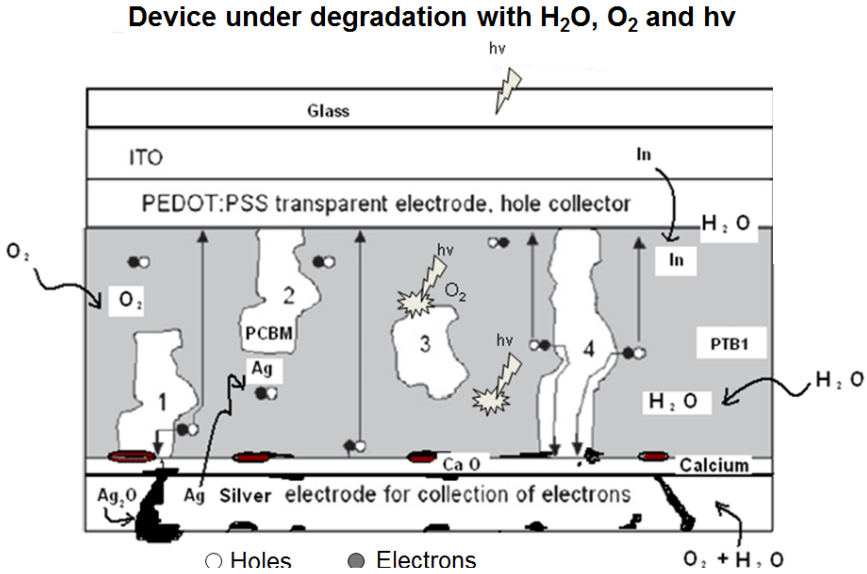

Fig. D-A4. The loss of the Jsc in the photovoltaic devices was due to the physical and chemical degradation. The reduction of FF is related by the increase of the series resistance into the device.

Appendix E. Manufacture of interdigitated heterojunction organic solar cells

The NAATs were prepared by two-step anodization process of aluminum metal in an aqueous solution of oxalic acid ($H_2Cr_2O_7$). To obtain the P3HT nanopillars, first the solution was prepared in chlorobenzene (C_6H_5Cl) and after it, it was spin coated onto the previous prepared structure of glass/ITO/PEDOT:PSS under nitrogen atmosphere. Afterwards, the nanoimprinting was done with the NAATs at 2 MPa as was describe in chapter 6. The $PC_{70}BM$ solution was prepared in anisole ($CH_3OC_6H_5$) and deposited on glass/ITO/PEDOT:PSS/P3HT nanopillars by spin coating. Ca and Ag metals were evaporated through a shadow mask. At the same time, planar bilayer organic solar cells (BL-OSC) were manufactured to compare against the interdigitated heterojunction organic solar cells. All the steps for the fabrication are depicted in **Fig. E-A5**.

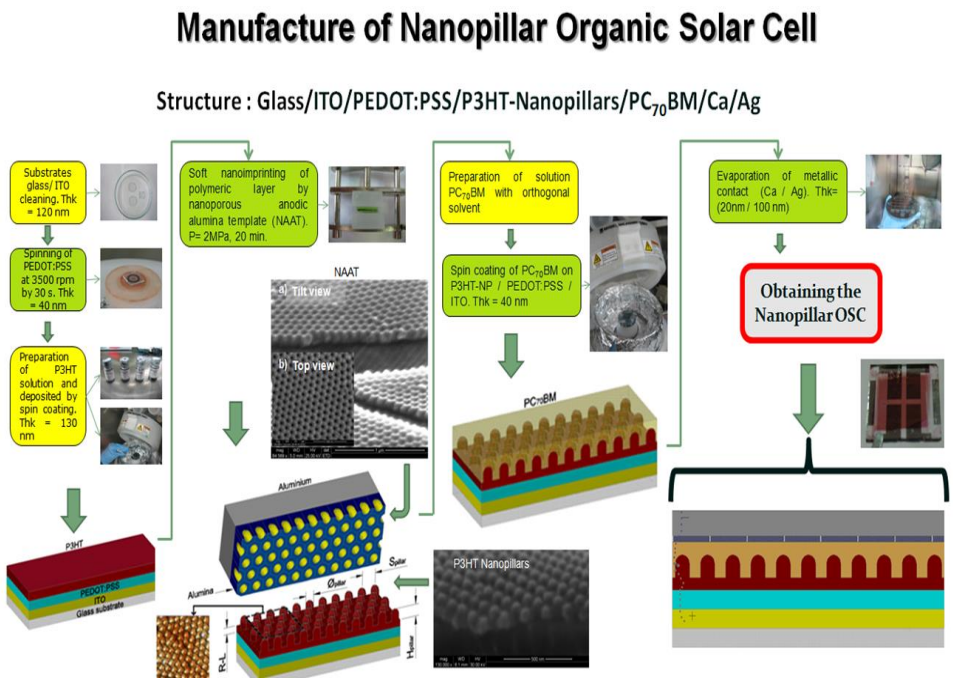

Fig. E-A5 General sequence is shown for the fabrication of IHJN-OSC.

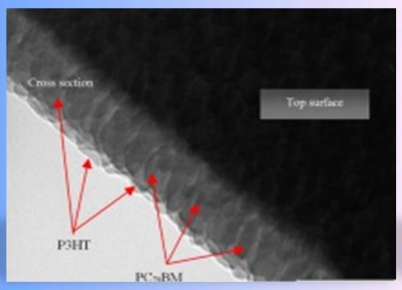

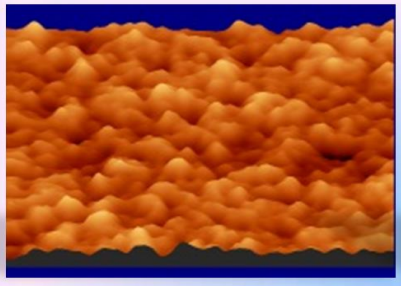

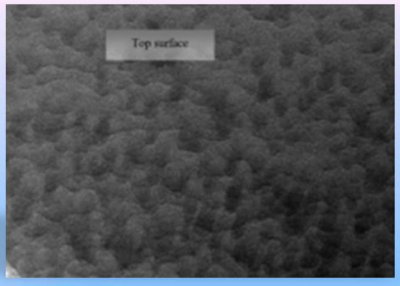

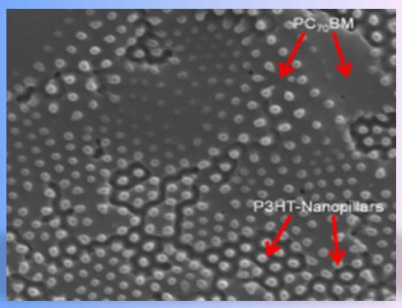

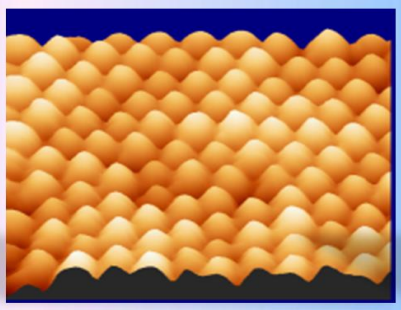

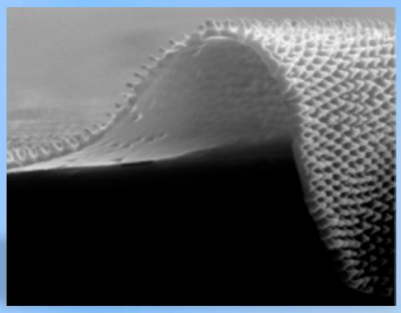

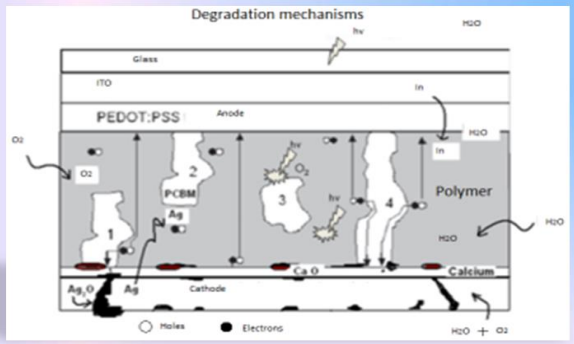

N_2

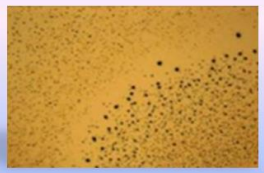

Air

O_2